UNIVERSITY OF LATVIA
FACULTY OF PHYSICS, MATHEMATICS AND OPTOMETRY

UNIVERSITY
OF LATVIA

GUNA DOĶE

RED AND NEAR INFRA-RED PERSISTENT LUMINESCENCE OF TRANSITION METAL ACTIVATED GERMANATE MATERIALS

DOCTORAL THESIS

FOR A DOCTORAL DEGREE IN PHYSICS AND ASTRONOMY
SUBSECTOR: SOLID STATE PHYSICS

Riga, 2023

The doctoral thesis was carried out at the Institute of Solid State Physics, University of Latvia from 2012 to 2023.

The thesis contains the introduction, four chapters, the theses, and reference list.

Form of the thesis: dissertation in Physics and Astronomy, subfield of solid state physics.

Supervisor: Prof. Dr. phys. Anatolijs Šarakovskis, Head of the laboratory and leading researcher of Laboratory of Spectroscopy at Institute of Solid State Physics, University of Latvia.

Reviewers:

1) *Dr. habil. phys.* Linards Skuja, leading researcher at Institute of Solid State Physics, University of Latvia;
2) *Dr. phys.* Pāvels Onufrijevs, leading researher at Institute of Technial Physics, Riga Technical University;
3) *Prof. PhD.* Marco Kirm, professor at Institute of Physics, University of Tartu (Estonia).

The thesis will be defended at the public session Doctoral Committee of Physics, Astronomy and Mechanics, University of Latvia, at 15:00 on May 12, 2023, in the conference hall of the Institute of Solid State Physics of University of Latvia.

The thesis is available at the Library of the University of Latvia, Kalpaka blvd. 4.

This thesis is accepted for the commencement of the degree of Doctor of science (PhD) in Physics and Astronomy by the Doctoral Committee of Physics, astronomy and mechanics, University of Latvia.

Chairman of the Doctoral Committee _____ *Dr. habil. phys.* Linards Skuja

Secretary of the Doctoral Committee _____ Sintija Siliņa

ANOTĀCIJA

Ilgstoša pēcspīdēšana ir luminiscence, kuras ilgums ir no dažām sekundēm līdz vairākām dienām pēc ierosmes avota izslēgšanas. Lielākajai daļai aprakstīto pēcspīdošo materiālu emisija ir elektromagnētiskā spektra redzamajā daļā, jo sevišķi zaļajā. Lai gan literatūrā ir minēts plašs pielietojuma klāsts materiāliem, kas izstaro sarkanajā un tuvajā infrasarkanajā spektra diapazonā, pētījumu skaits par šādiem materiāliem ir salīdzinoši mazāks. Balstoties uz iepriekšminētajiem apsvērumiem, šis darbs ir veltīts jaunu sarkanā un tuvā infrasarkanā spektra diapazonā emitējošu ilgspīdošu materiālu $MgGeO_3$: Cr^{3+} un $Mg_2Si_{1-x}Ge_xO_4$: Mn (x = 0.0 – 1.0) sintēzei un analīzei. Papildus tika analizēta iespēja uzlabot jau iepriekš zināma ilgspīdoša materiāla $MgGeO_3$: Mn^{2+} luminiscences īpašības, veicot sintēzi reducējošā atmosfērā.

Visi minētie materiāli tika sintezēti, izmantojot cietvielu sintēzes metodi, un analizēti, izmantojot tādas metodes kā rentgenstaru difrakcija, optiskā spektroskopija, elektronu paramagnētiskā rezonanse un termiski stimulētā luminiscence.

Tika secināts, ka visi trīs materiāli ir daudzsološi pēcspīdētāji, un paraugus ar optimālu aktivatoru koncentrāciju un pamatmateriāla sastāvu var raksturot ar pēcspīdēšanu, kas detektējama vairāk nekā 10 stundas pēc ierosmes avota izslēgšanas.

Šis darbs fokusējas uz lādiņnesēju ķērājcentru īpašībām un to ietekmi uz pēcspīdēšanas procesu. Tika secināts, ka $MgGeO_3$: Mn^{2+} materiālā pēc apstarošanas ar ultravioleto starojumu parādās diskrēti ķērājcentri, un sintēze reducējošā atmosfērā palielina seklo ķērājcentru, kas ir atbildīgi par pēcspīdēšanu istabas temperatūrā, koncentrāciju. $MgGeO_3$: Cr^{3+} gadījumā var runāt par ķērājcentru nepārtraukto sadalījumu, savukārt, $Mg_2Si_{1-x}Ge_xO_4$: Mn materiālos tika konstatēta abu tipu ķērājcentru klātbūtne. Darbā aplūkotais $Mg_2Si_{1-x}Ge_xO_4$: Mn izceļas ar tādu literatūrā reti aplūkotu īpatnību, ka par fotoluminiscenci un ilgspīdošo luminiscenci ir atbildīgi dažādi Mn luminiscences centri.

Apkopojot rezultātus, tika izdarīti secinājumi par ilgstošās pēcspīdēšanas mehānismiem un ķērājcentru īpašībām $MgGeO_3$: Mn^{2+}, $MgGeO_3$: Cr^{3+} un $Mg_2Si_{1-x}Ge_xO_4$: Mn materiālos.

Atslēgvārdi: Pēcspīdēšana; pārejas metāli; germanāti; ķērājcentri; termiski stimulētā luminiscence; elektronu paramagnētiskā rezonanse.

ANNOTATION

Persistent luminescence or afterglow or long-lasting phosphorescence is a luminescence characterised by the emission of radiation lasting from a few seconds to several days after the excitation source is turned off. Most of the persistent luminescence materials have emission in the visible part of the spectrum, especially in green. Despite great potential in applications, there is a lack of research on red and near infra-red emitting persistent luminescence materials. Therefore, this work is dedicated to the synthesis and analysis of novel red and near infra-red emitting persistent phosphors $MgGeO_3$: Cr^{3+} and $Mg_2Si_{1-x}Ge_xO_4$: Mn (x = 0.0 – 1.0). In addition, the possibility of improving the persistent luminescence properties of already known and recognised persistent luminescence material $MgGeO_3$: Mn^{2+} through the synthesis in a reducing atmosphere has been studied.

All materials have been synthesised by the solid state synthesis method and investigated using X-ray diffraction, optical spectroscopy, electron paramagnetic resonance and thermally stimulated luminescence.

It is concluded that all three materials are excellent persistent phosphors, and the samples with the optimal doping level and host composition exhibit a detectable afterglow well over 10 hours after switching off the excitation source.

This work focuses on the trap properties and their impact on the persistent luminescence mechanism. It is concluded that there are several discrete trap levels in the case of $MgGeO_3$: Mn^{2+}, and the synthesis atmosphere does not significantly impact the nature of the shallow traps responsible for room temperature persistent luminescence. In the case of $MgGeO_3$: Cr^{3+}, a continuous trap distribution is present. In $Mg_2Si_{1-x}Ge_xO_4$: Mn materials, the presence of both types of traps, discrete and continuous, were detected. The $Mg_2Si_{1-x}Ge_xO_4$: Mn stands out with the rarely reported feature of different Mn luminescence centres responsible for photoluminescence and for persistent luminescence.

Summarising the results, conclusions are drawn about the mechanisms of persistent luminescence and trap properties of $MgGeO_3$: Mn^{2+}, $MgGeO_3$: Cr^{3+} and $Mg_2Si_{1-x}Ge_xO_4$: Mn materials and their potential applications.

Keywords: Persistent luminescence; transition metals; germanates; traps; thermally stimulated luminescence; electron paramagnetic resonance.

TABLE OF CONTENTS

LIST OF SYMBOLS

Symbols

I	intensity
I_0	initial intensity
n	number of electrons/filled traps/etc.
n_0	initial number of electrons/filled traps/etc.
φ	probability of an electron to return to the ground state
t	time
n_T	number of electrons per unit volume in the trap states
n_{T0}	initial number of electrons per unit volume in the trap states
n_{CB}	number of electrons per unit volume in CB
N	trap concentration
τ	luminescence/trap lifetime
E	energy
E_a	activation energy or trap depth
C	constant of proportionality
c	probability of released electrons from CB to be retrapped by a trap
p	number of holes
r	probability of released electron recombining with a hole
T	temperature
s	frequency factor
b	order of kinetics
γ , l	fitting parameters
m	electron mass
r, d	distance
λ	wavelength
Θ	angle
Dq	crystal field splitting parameter
B	Racah parameter
α	Trees correction
T_{max}	temperature at maximum intensity point of TSL peak
T_{stop}	preheating temperature
β	heating rates
υ	frequency
B	strength of the applied magnetic field
g	spectroscopic splitting factor
$\breve{H}_{EZ}$	Hamilton operator for the electron Zeeman interaction
$\breve{H}_{ZFS}$	Hamilton operator for electron-electron interaction (zero-field splitting)
$\breve{H}_{HFS}$	Hamilton operator for nucleus-electron interaction
S	electron spin operator

$\boldsymbol{D}$	zero-field splitting tensor
$\boldsymbol{A}$	hyperfine coupling tensor
I	nuclear spin operator

Constants

k_B	Boltzmann constant	$8.617 \cdot 10^{-5}$ eV/K
h	Planck constant	$4.136 \cdot 10^{-15}$ eV/Hz
$\hbar$	Reduced Planck constant	$6.582 \cdot 10^{-16}$ eV·s
μ_B	Bohr magneton	$5.789 \cdot 10^{-5}$ eV/T

LIST OF ABBREVIATIONS

Sample names

aMGO	in ambient atmosphere synthesised $MgGeO_3$: Mn^{2+}
rMGO	in reducing atmosphere synthesised $MgGeO_3$: Mn^{2+}
MGO	$MgGeO_3$: Cr^{3+}
MSGO	$Mg_2(Si_{1-x}Ge_x)O_4$: Mn (x = 0.0 – 1.0)

Abbreviations

AC	alternating current
CB	conduction band
CT	charge transfer
CTB	charge transfer band
DC	direct current
DC-LED	direct current light emitting diode
EPR	electron paramagnetic resonance
ESR	electron spin resonance
ICDD	International Centre for Diffraction Data
IR	infrared
IRA	initial rise analysis
LED	light emitting diode
MW	microwave
NIR	near infra-red
OSL	optically stimulated luminescence
PDF	Powder Diffraction File
PersL	persistent luminescence
PL	photoluminescence
PLE	photoluminescence excitation
PMT	photomultiplier tube
RE	rare-earth
RT	room temperature
SH	spin Hamiltonian
TM	transition metal
TSL	thermally stimulated luminescence
UV	ultraviolet
UVC	ultraviolet-C (200 – 300 nm)
VB	valence band
VIS	visible
XRD	X-ray diffraction

LIST OF FIGURES

LIST OF TABLES

INTRODUCTION

Motivation

Persistent luminescence, also called long-lasting phosphorescence or simply afterglow, is a luminescence characterised by the emission of radiation from a few seconds to several days after the excitation source has been switched off. Although the process has been known for centuries, active research on afterglow materials began in the late 1990s. Over the last 25 years, research on persistent luminescence materials, both in fundamental and applied physics, has developed rapidly; however, the explanation of the physical processes that cause afterglow still needs to be clarified, and there are many unanswered questions and unexplored potential applications. Today, persistent luminescence materials are used mainly for technologically trivial applications, such as luminescent paints, safety signs and decorations. At the same time, research and development of novel persistent luminescence materials and their application in medicine, military technology, anti-counterfeiting, etc., are underway.

Currently, most of the emission of well-developed materials is in the visible part of the spectrum, especially green, which is not optimal or usable for several applications, such as night vision surveillance, biomedical imaging, etc., where red and near infra-red emission would be necessary. Still, there is relatively less research on materials with emission bands in the red and near infra-red regions. Additionally, these materials rarely are as efficient in the sense of intensity and longevity as their counterparts emitting green and blue light. Besides, it should be noted that most of the used persistent luminescence phosphors currently employ rare-earth element ions as activators. Rare-earth elements are relatively expensive; thus, their use increases overall production costs for persistent phosphors. Therefore, the common tendency in the development of a new generation of persistent luminescence materials is to avoid rare-earth elements by substituting them with elements from the other groups, primary transition metals.

For red and near infra-red emission, manganese and chromium ions are commonly suggested. As transition metal ions, manganese and chromium are strongly affected by the crystal field surrounding them and, when introduced into a properly chosen matrix, can provide red afterglow in the case of Mn^{2+} and near infra-red afterglow in the case of Cr^{3+}. On the other hand, germanate materials have attached widespread attention due to the high density of trapping levels, and there are many reports on excellent Mn^{2+} and Cr^{3+} activated germanate persistent luminescence materials; therefore, the aim of this work was set as follows.

The aim and main tasks of the work

The aim of this work is to **design new and improve already established transition metal doped red and near infra-red persistent luminescence materials.**

To achieve this goal, the following tasks were set:

- ► Synthesis of Mn^{2+} and Cr^{3+} activated germanate materials using solid state synthesis method;
- ► Characterisation of material structure using X-ray diffraction and electron paramagnetic resonance methods;
- ► Characterisation of the spectroscopic properties of prepared materials using optical spectroscopy methods such as photoluminescence spectra, decay kinetics, photoluminescence excitation spectra, persistent luminescence spectra and kinetics measurements;
- ► Analysis of defects in the synthesised materials, including characterisation of the charge carrier trap properties: depth, distribution, density and stability, and identification of corresponding defects using thermally stimulated luminescence and electron paramagnetic resonance experimental methods.

Contributions of the Author

Most of the samples have been synthesised by the Author. The Author measured all the photoluminescence emission and excitation spectra and kinetics at room temperature, persistent luminescence spectra and kinetics, thermally stimulated luminescence glow curves and X-ray diffraction patterns. The Author has performed all data analysis, calculations, and visualisation.

MSc Aija Kalnina has assisted with the synthesis of the samples. PhD Guna Krieke has performed low-temperature decay kinetic measurements. PhD Andris Antuzevics has carried out electron paramagnetic resonance measurements and their preliminary analysis.

The Author of the doctoral thesis manuscript is the corresponding author of all scientific publications directly related to the thesis and has presented most of the results at several international and local scientific conferences.

Scientific novelty

Within the framework of the dissertation, new, previously not reported red and near infra-red persistent luminescence phosphors $MgGeO_3$: Cr^{3+} and $Mg_2Si_{1-x}Ge_xO_4$: Mn (x = 0.0 - 1.0) have been successfully synthesised and analysed. An interpretation of the luminescence mechanisms in them has been provided. In addition, the possibility of improving the persistent luminescence properties of already known and recognised persistent luminescence material $MgGeO_3$: Mn^{2+} has been studied. To obtain optimal luminescence properties of these materials, methods such as finding the optimal concentration of activators, synthesis in different atmospheres, and modification of the host material composition have been used.

Most of the results presented in this work have been published in peer-reviewed scientific journals indexed in the international scientific database SCOPUS.

Outline of the thesis

This work contains an Introduction, four chapters, the Theses, and a Reference list.

Chapter 1. Theoretical background. Here physical foundation of photoluminescence and persistent luminescence is described with an emphasis on the mechanism of persistent luminescence. The overview of point defects in solids and general properties of transition metals manganese and chromium is also given.

Chapter 2. Literature review. Here an analysis of established persistent phosphors is given with emphasis on applications and strategies for designing persistent phosphor materials. A literature overview of Mn^{2+} and Cr^{3+} doped persistent phosphors is presented, together with a comprehensive analysis of previous reports on host materials used in this dissertation.

Chapter 3. Experimental. The employed experimental equipment units and their basic physical operating principles and mathematical and physical background of used data processing are reported here. In addition, an overview of the material synthesis is given.

Chapter 4. Results and discussion. This chapter is divided into three subsections, one for each researched material. The first subsection elaborates on differences in luminescence properties of the $MgGeO_3$: Mn^{2+} material synthesised either in the air or in a reducing atmosphere. The second reports on novel broadband near infra-red persistent phosphor $MgGeO_3$: Cr^{3+}, and the third discusses the luminescence properties of manganese doped Mg_2SiO_4 - Mg_2GeO_4 solid solution.

1. THEORETICAL BACKGROUND

1.1. Introduction to luminescence in solid state materials

The word *luminescence* was coined in 1888 by German physicist Eilhardt Wiedemann using the Latin words *lumen*, which means "light", and *escentia,* which means "the process of", meaning luminescence is the process of giving off light. Years later, luminescence was defined as the radiation that the body emits in addition to thermal radiation and whose decay time exceeds 10^{-10} s; thus, it is significantly larger than the period of oscillations of the emitted light [1–3].

Luminescence can be observed on a wide variety of materials - organic and inorganic, solids and non-solids; however, in the scope of this dissertation, only inorganic solid state luminophores will be discussed. Thus, all the terminology, which sometimes differs between fields, will match the use of inorganic solid state materials.

There are two widely used classification systems for luminescent materials, one based on the source of excitation and the second based on the emission duration.

Typical examples of different types of luminescence distinguished according to the source of excitation are electroluminescence (excited by applying an electric field), mechanoluminescence (excited through mechanical action), chemiluminescence (excited with chemical reactions), photoluminescence (excited with optical radiation), etc. It should be noted that most of these have subdivisions, and nearly 20 different types of luminescence based on the nature of excitation have been defined [4,5].

Depending on the emission duration after the excitation has stopped, the luminescence is traditionally divided into fluorescence and phosphorescence. Fluorescence is short luminescent emission from allowed transitions between states with the same spin. The fluorescence decay of a single centre is exponential, with a lifetime of less than 10^{-8} s. On the other hand, phosphorescence is a somewhat delayed emission of photons. This delay is provided by forbidden transitions from quasi-stable excited states or trap levels that capture charge carriers. Phosphorescence is characterised by a lifetime of more than 10^{-8} s and subdivided into sort-period phosphorescence with a lifetime up to 10^{-4} s and long-period phosphorescence with a lifetime of more than 10^{-4} s. If traps are not involved in the phosphorescence process, the decay of a single centre also can be exponential but usually lasts no longer than a second. In the case of the involvement of traps, phosphorescence may last not only seconds, minutes, or hours but even days, and its decay curve typically is quite complex. For the last decade, this type of luminescence has been predominantly called persistent luminescence (PersL), and most authors use it interchangeably with terms such as afterglow and long-lasting phosphorescence [3,6,7].

This dissertation is dedicated to the PersL of inorganic phosphors; however, photoluminescence (PL) measurements will be used for the analysis of the materials discussed in the Results and Discussion part of this work. Thus, in the following subsection, the basic principles of the PL process will be explained.

1.2. Photoluminescence

As previously mentioned, PL is a type of luminescence in which the emission of light results from the excitation by optical radiation, typically ultraviolet (UV) or visible (VIS) light. The solid state phosphors typically are crystals or glasses with intrinsic defects or impurities called activators or dopants that can function as luminescence centres in these materials. Most currently researched and commercialised solid state phosphors are activated by rare-earth (RE) or transition metal (TM) ions, and electronic transitions that produce PL happen within these dopant ions. The host itself does not participate in the production of luminescence [6].

A schematic representation of a configurational coordinate model for the excitation and emission process is shown in **Fig. 1.1. (a)**. The configurational coordinate model is widely used to explain the optical properties of a localised centre based on potential curves, each representing the system's total energy in its ground or excited state as a function of the configurational coordinates. If the dopant ion absorbs a photon with the appropriate energy, the electron can move from the ground state to the excited state. Typically, a fast relaxation occurs, and the system locates in the equilibrium position. The energy difference will be lost in the form of phonons. From here, the electron can return to the ground state by emitting a photon with energy smaller than the energy of the absorbed photon. This shift between excitation and emission energies is called the Stokes shift. It should be noted that this is not the case for all phosphors: the emitted photon may have higher energy than the absorbed, and so-called anti-Stokes emission can be observed.

As shown in **Fig. 1.1. (a)**, the two parabolas intersect. The difference ΔU between the energies of the intersection and the minimum of the excited level represents the smallest energy necessary so that the electron in the excited state overpass a thermal barrier and can return to the ground state nonradiatively. The required energy is usually received by means of thermal energy in the form of phonons and a process is called thermal quenching of luminescence [3,6,8].

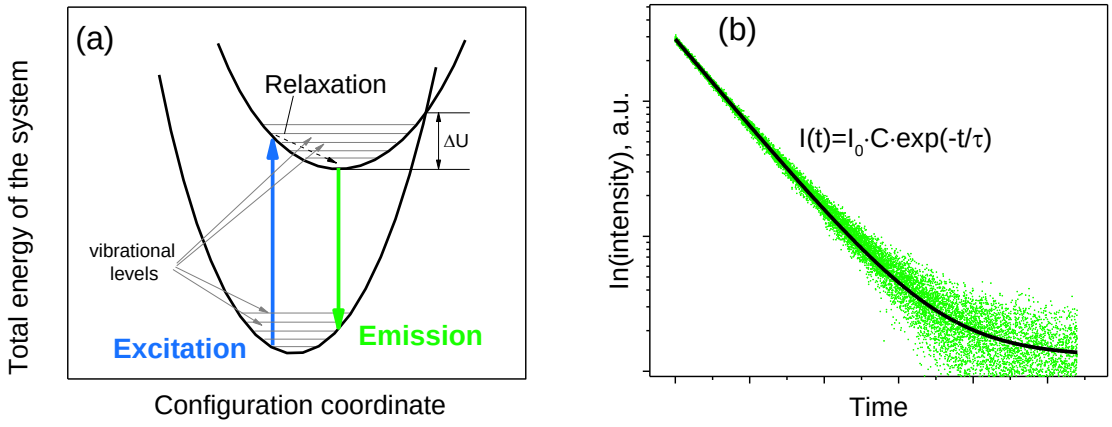

Fig. 1.1. (a) *A schematic representation of a configurational coordinate model for the PL process,* ***(b)*** *typical decay curve of monomolecular recombination process, semi-logarithmic scale.*

In the simplest case, when the PL process follows the scheme mentioned above, the PL emission intensity *I* will be proportional to the rate $\frac{dn}{dt}$ at which electrons from the excited state return to the ground state. Hence, if *n(t)* is the number of electrons at the excited state at any instant of time t and φ is the probability of an electron to return to the ground state, *I* is given by

$$I = -C\frac{dn}{dt} = C \cdot \varphi \cdot n(t), \tag{1.1}$$

where *C* is a constant. The rate of decay φ is inversely proportional to luminescence lifetime τ; hence the solution of the differential equation presented in *Eq. (1.1)* gives

$$n(t) = C \cdot n_0 exp\left(-\frac{t}{\tau}\right), \tag{1.2}$$

where n_0 is the initial number of electrons at the excited state. If expressed as a change of intensity in time:

$$I(t) = I_0 \cdot C \cdot exp\left(-\frac{t}{\tau}\right). \tag{1.3}$$

I_0 is the initial luminescence intensity when excitation ceased (t = 0). These equations are characteristic of the first-order, also called monomolecular decay kinetics, and based on *Eq. (1.3)*, the decay curve of this process is exponential, an example is shown in **Fig. 1.1. (c)** [9–11].

1.3. Persistent luminescence

Although the PersL phenomenon has been known for centuries, with the first reports coming from China dated around 960–1279 A.D. [12], until the end of the 20th century, only a limited number of studies were devoted to the understanding of physical processes behind PersL and development of new PersL materials. In 1996 Matsuzawa *et al*. [13] demonstrated remarkable properties of $SrAl_2O_4$: Eu^{2+}, Dy^{3+} emitting green, bright luminescence lasting for more than 30 hours, which led to rapidly increased interest in the PersL materials. Since then, materials with long-lasting afterglow have been widely studied due to their wide range of potential applications and versatile functionality [14–18].

1.3.1. Band theory of solids and trap levels

The energy band concept is often used as a great way to visualise several properties and processes, including PersL, of solid state materials. In a single isolated atom, the electrons in each orbit have discrete energy; however, if multiple atoms are brought together, for example, as a molecule, the energy levels will split. This is caused by the electrical interactions and the exclusion principle; namely, the wave functions of the electrons, mainly outer valence electrons, will distort and allowed energies will shift (some

upward and some downward by varying amounts) as the valence electron wave functions become less localised and extend over more and more atoms. When a large number of atoms, typically near the order of Avogadro's number (10^{24}), are brought together to form a solid material, the difference between energy values of the levels becomes so tiny that they can be perceived as continuous bands of energy rather than the discrete energy levels [7,19,20]. The highest band filled with electrons is called the valence band (VB). The next higher band, called the conduction band (CB), generally is empty. However, if external energy is applied, the electrons of the VB can be transferred to the CB and become free electrons. In this case, a vacant site, called a hole, is left behind in the VB. Holes act as positive charge carriers and may migrate through the material just as free electrons. Between CB and VB, there is an energy gap corresponding to forbidden energies called a forbidden band or band gap. It is characterised by energy value E_g. In the case of an ideal, pure crystal, there are no energy levels within the band gap, and optical absorption only takes place for radiation with photon energies larger than E_g. However, real crystals have imperfections, such as impurity ions and lattice defects. These imperfections introduce a local change in the system, and new energy levels are produced within the band gap. These energy levels may form recombination (luminescence) centres or trapping centres. Recombination centres are the source of emission, typically RE or TM ions; however, host related centres may also appear. On the other hand, trapping centres or traps capture free electrons from the CB or holes from the VB [21,22].

Traps are crucial for PersL since the necessary delay of luminescence comes from gradual charge carrier release after they have been captured. In general, the speed at which the traps can be emptied depends on the trap depth, also called activation energy E_a and temperature T. If the traps are too deep, a considerable amount of thermal energy is required for the detrapping, and it is possible that PersL at room temperature (RT) cannot be observed. However, if traps are too shallow – charge carriers will escape rapidly, ensuring intense but short PersL. Typically, when speaking of traps, the electron traps are meant, and the trap depth is expressed in eV below the bottom of the CB, and it is believed that the best trap depth for excellent PersL performance at RT is up to 0.8 eV [5,23].

If the energetic distance between adjacent trapping states is small, continuous trap distribution in place of discrete trapping levels is considered. This is assumed to be caused by slight variations in the environment of the defects responsible for the traps [24,25].

1.3.2. Basic mechanism of persistent luminescence

The real-life mechanism of PersL is a complex multi-step process consisting of various possible occurrences with occurring probabilities depending on multiple conditions; thus, for physically meaningful interpretation, each material must be evaluated individually. Even arguably the most widely explored phosphor to date, $SrAl_2O_4$: Eu^{2+}, $Dy^{3+,}$ has several possible mechanisms offered [26], and there still is not an unanimous opinion on some of them.

Despite the perplexing nature of the PersL mechanism, it is accepted that this process involves three key steps: 1) ionisation, 2) trapping, and 3) detrapping. The first step of the PersL process consists of electron excitation and delocalisation. Normally, an electron

at an excited state is still attached to its parent ion; it is localised. However, if sufficient energy is provided, the electron can reach the CB, becoming mobile and delocalised. For oxide-based phosphors, there are three typical electron delocalisation mechanisms. The first is a straightforward band-to-band transition if the absorbed energy $E \geq E_g$. Other two are so-called charge transfer (CT) transitions. In **Fig. 1.2.** CT1 stands for CT from oxygen ion in VB to activator ion creating charge transfer band (CTB). If CTB is close enough to CB, some electrons may cross over to CB. Further, CT2 stands for CT from the ground state of the activator ion to the CB; therefore, photo-oxidation of the activator ions occurs. In all three cases, if an electron is transferred to the CB, a hole is left behind. Delocalised charge carriers can move throughout the crystal; however, at some point, the localisation of charge carriers at appropriate defect sites will occur. In other words – electrons will be trapped by electron traps, and hole traps will trap holes. Direct electron-hole recombination can also happen; in this case, so-called band-edge luminescence emerges [27].

After charge carriers have been trapped for some time, detrapping and consequent charge carrier recombination at the recombination centre occurs. There are two liberation possibilities – thermal promotion to CB or quantum tunnelling to the recombination centre. Additional competitive process – retrapping may occur. Retrapping is a process where the escaped charge carriers are recaptured before they reach recombination centres. These processes will be described in detail in the following subsections.

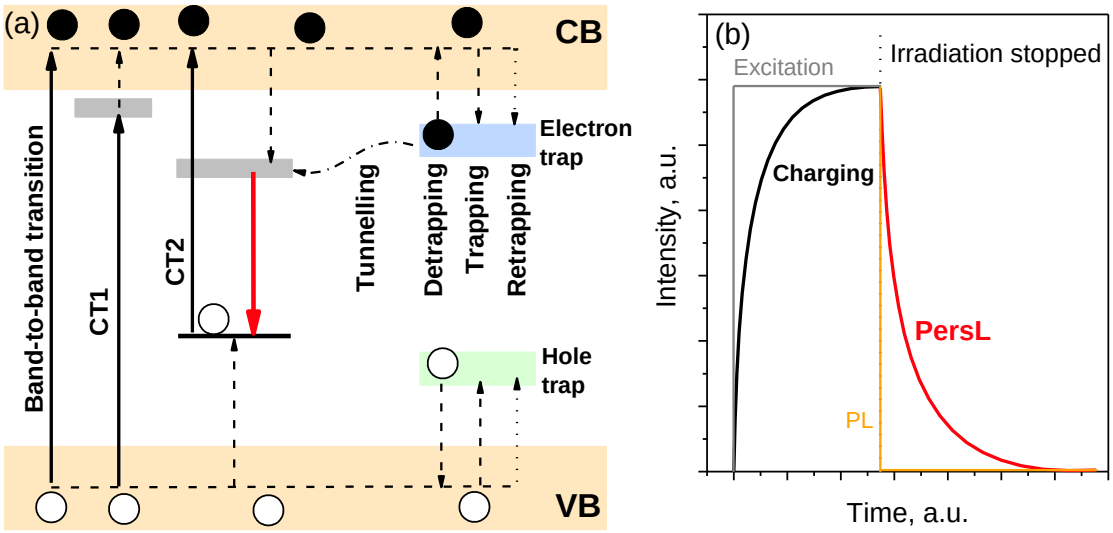

Fig. 1.2. (a) *Schematic diagram of the mechanism of PersL (● – electrons, ○ – holes) and* ***(b)*** *typical profiles of the emission intensity of PersL and PL phosphor during and after the irradiation.*

Additionally, **Fig. 1.2. (b)** shows a typical intensity-time plot of PersL during the charging of the sample and consequent decay when irradiation is stopped. The comparison profile of traditional PL intensity during excitation and emission has also been shown. Besides longer decay time, a notable difference is the gradual increase of intensity while the sample is irradiated/charged. This arises from the fact that initially, when most of the traps are empty, the trapping dominates over the recombination, thus, weaker emission intensity. As more traps are filled, more charge carriers are "left" for recombination, and intensity increases until the trapping and recombination processes achieve equilibrium [6].

Note that although both electrons and holes are equally important for recombination to occur, typically, “the electron picture” is used to illustrate excitation, trapping, retrapping, recombination, emission, tunnelling, etc. This approach will be used here as well.

1.3.3. Detrapping via thermal promotion to the conduction band

The most reported detrapping mechanism undoubtedly is electron detrapping via thermal promotion to CB. After being captured, the electron will remain trapped for some time τ – the mean lifetime of the trap:

$$\tau = \frac{1}{s} exp\left(\frac{E_a}{k_B T}\right), \tag{1.4}$$

where s – frequency factor, sometimes called attempt-to-escape factor. In the simple model, s is considered a temperature independent constant with a value in the order of the lattice vibration frequency, 10^{12} – 10^{14} s^{-1}. E_a is activation energy or trap depth – the energy necessary for an electron to get promoted from trap to CB, k_B – the Boltzmann constant and T – temperature.

In the simple model shown in **Fig. 1.2. (a),** only one kind of electron trap is considered. If n_T and n_{CB} are the number of electrons per unit volume in the trap state and CB, respectively, t is time, N is trap concentration, and c is the probability of released electrons from CB to be retrapped by a trap, the rate equation representing the detrapping of electrons after irradiation is stopped can be written as *Eq. (1.5)*

$$\frac{dn_T}{dt} = -\frac{1}{\tau} n_T + c(N - n_T) n_{CB}. \tag{1.5}$$

Meanwhile, the rate equation representing the detrapping of holes is:

$$\frac{dp}{dt} = -rpn_{CB}, \tag{1.6}$$

where p is the number of holes and r is the probability of released electron recombining with a hole. By assuming that the number of the electrons in the CB in the PersL process is so tiny that $p \approx n_T$ and $\frac{dp}{dt} \approx \frac{dn_T}{dt}$, *Eq. (1.5)* and *Eq. (1.6)* gives:

$$\frac{dn_T}{dt} = \frac{-\frac{1}{\tau} n_T^2}{n_T + \left(\frac{c}{r}\right)(N - n_T)} \tag{1.7}$$

Eq. (1.7) can be solved analytically for two cases: $c \ll r$ and $c \approx r$. These two decaying mechanisms are known as the first-order kinetics or monomolecular reaction mechanism and as the second-order kinetics or bimolecular reaction mechanism, respectively [6,10].

1.3.3.1. First-order kinetics

The first-order kinetics model of detrapping was introduced by Randall and Wilkins in 1945 [28,29], and it presumes that firstly – only one type of trap is present and secondly – retrapping is negligible and once released from traps, electrons are not retrapped in the afterglow process. Since the excited state lifetimes of the luminescence centres are typically shorter than the trap lifetimes, the PersL process will be governed by the lifetime of the traps [10]. The mathematical description of the first-order kinetics model following the PersL process is basically the same as in the case of PL, i.e., *Eq. (1.1 – 1.3)*. The key difference here is that *n* stands for the concentration of the occupied traps, not electrons in an excited state, and τ is the mean lifetime of the trap, not the excited level. According to *Eq. (1.3)*, the decay profile of PersL is exponential; however, in practical phosphorescent systems, single exponential decay has been rarely, if ever, reported [30,31]. In the case of multiple independent trapping centres, *Eq. (1.3)* can be rewritten as a sum of multiple exponential equations.

1.3.3.2. Second-order kinetics

If the retrapping probability of the electrons is equal to the probability of recombination, *Eq. (1.7)* transforms to:

$$-\frac{dn_T}{dt} = \frac{n_T^2}{\tau N}, \tag{1.8}$$

and the number of trapped electrons per unit volume is given by *Eq. (1.9),* where n_{T0} is the initial number of electrons per unit volume in the trap states.

$$n_T = \frac{n_{T0}}{1 + \left(\frac{\tau N}{n_{T0}}\right) t} \tag{1.9}$$

Just as previously, we assume that emission intensity *I* of the afterglow is proportional to rate $\frac{dn_T}{dt}$, thus

$$I(t) = \frac{I_0}{(1+\gamma t)^2}, \qquad \gamma = \frac{\tau N}{n_{T_0}} \tag{1.10}$$

This is called the second-order kinetics model of detrapping, and it was developed by Garlick and Gibson in 1948 [32]. The afterglow of such a process is no longer exponential but has a power-law like behaviour.

1.3.3.3. General order kinetics

For real phosphors, however, the total afterglow decay curve cannot be easily described using first or second-order kinetics equations. For intermediate situations, May and Partridge [33] developed a so-called general order kinetics expression:

$$I(t) = \frac{I_0}{\left(1 + (b-1)\frac{t}{\tau}\right)^{\frac{b}{b-1}}} \tag{1.11}$$

where b is the kinetic order (often $1 < b \leq 2$), *Eq. (1.11)* is not valid for $b = 1$; however, it is reduced to *Eq. (1.3)* when $b \rightarrow 1$ and to *Eq. (1.10)* when $b \rightarrow 2$ [34].
Due to the complicated nature of *Eq. (1.11)*, most authors use simplified expression *Eq. (1.12)* where γ and l are fitting parameters, and l usually is between 1 and 2; however, values as low as 0.5 has been reported [16,30,35–37].

$$I(t) = \frac{I_0}{(1 + \gamma t)^l} \tag{1.12}$$

Eq. (1.12) corresponding function is called compressed hyperbola or Becquerel function.

Another expression used for complex phosphor systems is stretched exponential function or Kohlrausch function [38]:

$$I(t) = I_0 exp\left[-\left(\frac{t}{\tau}\right)^{\alpha}\right], \quad 0 < \alpha < 1. \tag{1.13}$$

In studies of the relaxation of complex systems, the Kohlrausch function is frequently used as a purely empirical decay law; nevertheless, it is found that stretched-exponential luminescence decay corresponds to a broad distribution of lifetimes which correspond to the individual relaxation processes, radiative or nonradiative. Thus this type of afterglow decay behaviour may indicate high disorder in the proximity of the luminescence centre [39,40].

1.3.4. Detrapping via tunnelling

Simple models of PersL typically assume recombination via the CB; however, an alternative pathway is a localised transition where an electron recombines with a hole in the nearby luminescence centre via quantum tunnelling [41]. Tunnelling refers to the quantum mechanical phenomenon where a wave function can go through a potential barrier that it classically could not overcome. In the context of PersL – trapped electrons can tunnel to the nearby excited state of the luminescence centre, entirely omitting thermal promotion to CB [42]. Tunnelling may be a temperature independent or temperature assisted process [43]. In the latter case, additional thermal excitation of an electron to a higher vibrational level of the trap is necessary, after which athermal tunnelling towards the excited state of the

emission centre can occur. The tunnelling probability, in this case, increases with increased temperature [44].

In contrast to classical thermal retrapping via the CB model, tunnelling does not require trap levels to be in a specific depth for PersL to occur; thus, tunnelling is mainly used to explain the PersL mechanism related to deep traps.

There are two necessary conditions for electron tunnelling to occur [45]:

- the electron wave functions must overlap for the electron initial and final state;
- the energy of an electron in the initial and final state must be equal.

The general notions of detrapping via tunnelling are as follows. By approximating the electron trap with a square potential well, the rate of tunnelling *P(r)* of the electron can be expressed with *Eq. (1.14)*.

$$P(r) = s \cdot exp\left(-2\frac{\sqrt{2mE}}{\hbar} \cdot r\right) \tag{1.14}$$

Here *s* – frequency factor, *m* – electron mass, *E* – the barrier height for traps located at distance r from the recombination centre, and *ħ* – reduced Planck constant. If the PersL process obeys first-order kinetics (no retrapping), the change of the PersL intensity in time in the case of detrapping via tunnelling is given by

$$I(t) = \int_0^\infty n_0^2 exp(-P(r)t)4\pi r^2 dr \tag{1.15}$$

where n_0 is the initially occupied trap concentration. It has been shown that when the tunnelling is from an electron trap into a random distribution of recombination centres, *Eq. (1.15)* yields approximately *Eq. (1.12)* with l = 1 or close to 1 [44,46].

1.4. Defects in crystals

In an ideal crystal, there are no defects; however, an ideal crystal can be obtained, hypothetically, only at an absolute zero temperature. At any actual temperature, there will be some vibration of atoms, which, in a sense, may be perceived as a defect, but also, several atoms are inevitably misplaced; even more, typically, there will be the presence of some extrinsic defects as well.

The most used classification scheme for defects is based on the size and shape of the defect. For example, point defects involve one atom or site; line defects are multiple point defects in a row, and in the case of plane defects, the whole layer in the crystal structure may be out of order. In the context of PersL, the point defects are the most important [22].

1.4.1. Point defects in crystals

The point defects expected in a real crystal are shown schematically in **Fig. 1.3.** and can be divided into the following groups:

- *vacancies* – anion or cation is removed from its site and not replaced;
- *interstitial* – an ion, intrinsic or extrinsic, occupies an interstitial site that is normally empty;
- *antisite* – an ion on a site normally occupied by a different element which exists in the material;
- *substitutional defects* – an ion is substituted by an extrinsic ion. Dopants are substitutional impurity defects;
- aggregate forms of the defects mentioned above [47–49].

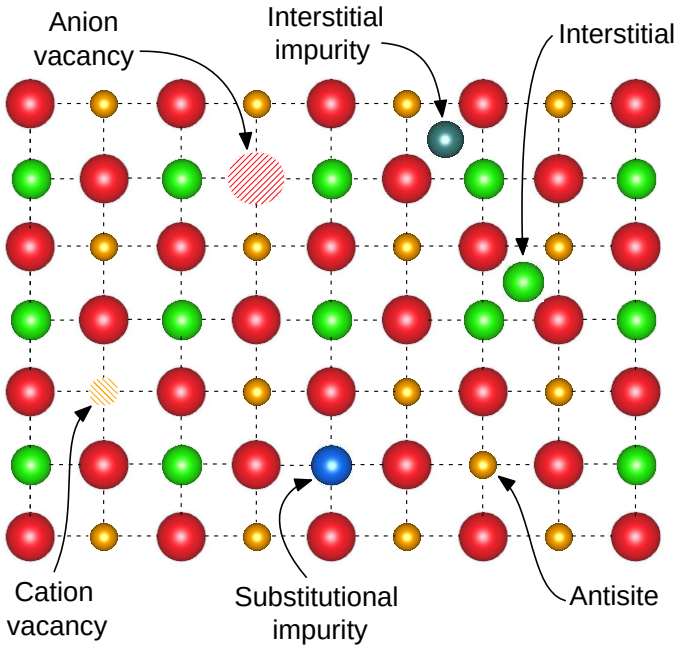

***Fig. 1.3**. Schematic illustration of various point defect types in real crystals, including vacancies, interstitials, antisite defect, and substitutional impurity.*

1.4.2. Kröger-Vink notation

The notation of point defects, the sites involved and effective charges on the defects were developed by F. A. Kröger and H. J. Vink at 1950s. The notation follows the simple scheme of M_S^C, where *M* stands for the species (atoms, vacancies, typically denoted by V, interstitials, electrons, or holes). *S* indicates the lattice site occupied by *M*, and *C* represents the electronic charge of the *M* with respect to the lattice. Here typically used symbols are [×] for a zero net charge, [•] for a positive charge, and ['] for a negative charge. For example, $Mn_{Mg}^{\times}$ is a divalent manganese ion in a divalent magnesium site; isovalent substitution yields a neutral charge with respect to the crystal lattice. On the other hand, $V_O^{\bullet\bullet}$ stands for oxygen

ion vacancy. Since oxygen ions have a 2- charge, the lack of it creates a net positive charge, specifically here +2 [22,49].

1.4.3. Colour centres and charge carrier traps

Another subclass of defects is so-called colour centres which have obtained their name because they absorb some part of visible light, thus lending a characteristic colour to the crystal. Colour centres are point defects or point defect aggregates associated with trapped electrons or holes. A typical example of a colour centre is F-centre (from the German word *Farbe*, which means "colour"). Here the presence of anion vacancy creates a localised positive charge since the negative ion which normally occupies the site is missing. If a free electron moves through the crystal, it will be attracted by the Coulomb force to the localised positive charge and can be trapped in the vacancy creating the F-centre.

Analogous, a cation vacancy may be involved in hole trapping; in this case, the system is called the V-centre. Specifically, in oxides, by V-type centre, a hole trapped by oxygen and stabilised by a neighbouring cation vacancy is understood.

There are several other colour centre types, such as M-centre (two neighbouring F-centres), V_k-centre (one hole shared by two adjacent anions), etc. Altogether it can be assumed that F-type centres serve as electron traps and V-type centres as hole traps.

In addition to F-type centres, electron traps are produced by aliovalent cationic substitutional impurities. Namely, if a trivalent cation substitutes a divalent cation, the local crystal field becomes positively charged and can trap an electron [22,47,50].

1.4.4. Solid solutions

In crystallography, if the dopant concentration extends 1%, it may be referred to as a solid solution rather than a doped material. However, most authors in the field of luminescence use this term when describing a family of materials with a range of compositions and a single crystal structure. Well-known examples are NaCl – KCl or Mg_2SiO_4 – Fe_2SiO_4 solid solutions. NaCl and KCl have the same cubic crystal structure, and it is possible to make a pure compound with any ratio of Na^+ to K^+. Similarly, forsterite Mg_2SiO_4 and fayalite Fe_2SiO_4 can form pure solid solution $Mg_{(2-x)}Fe_xSiO_4$, with physical properties smoothly varying from those of forsterite to those of fayalite by increasing x value. Simply put, a solid solution is a crystalline phase with variable composition [22].

Solid solutions change the properties of the material by distorting the crystal lattice. If the radii of the variable ions differ, it is expected that the unit cell of the material will change accordingly. For instance, in the case of $Mg_{(2-x)}Fe_xSiO_4$ solid solution, if Mg^{2+} with a radius of 0.72 Å is gradually replaced by Fe^{2+} with a radius of 0.61 Å [51], the unit cell volume will decrease. In general, the unit cell volume of a solid solution can be calculated using Vegard's law [52] which states that the lattice parameter of a solid solution of two components is approximately a weighted mean from both of them at the same temperature.

Efficient forming of substitutional solid solution can be expected if the following statements are true:

- ► the ionic radii of exchanging elements are close (no more than 15 % difference);
- ► involved crystals have the same structure;
- ► exchanging ions have similar electronegativities;
- ► exchanging ions have the same or comparable valency [22,53].

1.5. Properties of the transition metal ions

The TM elements, also called the d-block elements, are characterised by a partially filled d subshell and the ability to produce cations with an incomplete d subshell. There are 40 elements in this group with atomic numbers 21 (scandium) to 30 (zinc), 39 (yttrium) to 48 (cadmium), 71 (lutetium) to 80 (mercury) and 103 (lawrencium) to 112 (copernicium) [7]. However, mostly 3d elements are used as dopants in optical materials [54], and here term TM will be used interchangeably with 3d elements. A summary of TM with 3d electronic configuration is given in *Table 1.1*.

Table 1.1. Transition metals with 3d electronic configuration.

Configuration	*$3d^0$*	*$3d^1$*	*$3d^2$*	*$3d^3$*	*$3d^4$*	*$3d^5$*	*$3d^6$*	*$3d^7$*	*$3d^8$*	*$3d^9$*	*$3d^{10}$*
Ions										Cu^{2+}	Cu^{+}
								Ni^{3+}	Ni^{2+}	Ni^{+}	
							Co^{3+}	Co^{2+}	Co^{+}		
						Fe^{3+}	Fe^{2+}				
		Mn^{6+}	Mn^{5+}	Mn^{4+}	Mn^{3+}	Mn^{2+}	Mn^{+}				
		Cr^{5+}	Cr^{4+}	Cr^{3+}	Cr^{2+}	Cr^{+}					
	V^{5+}	V^{4+}	V^{3+}	V^{2+}							
	Ti^{4+}	Ti^{3+}	Ti^{2+}								

In contrast to more commonly studied RE ions, spectroscopically active orbitals (d subshell) in TM ions are also the valence orbitals, leading to high environmental sensitivity. Consequently, different hosts will provide different optical properties of TM ion activators [55]. Namely, when the ion is a part of a crystal, the effect of the crystal field (the electric field created by the adjacent ions) must be considered since it causes splitting and bending of the free ion levels. The two types of crystalline environments relevant to this dissertation are octahedral and tetrahedral molecular geometries shown in **Fig. 1.4**. In the case of an octahedral environment, the TM ion is at the centre of six equally spaced anions, producing an electric field of octahedral symmetry at the site of the TM ion. In the case of a tetrahedral environment, anions are at the four corners of a tetrahedron and produce an electric field of tetrahedral symmetry at the site of the TM ion. Based on estimated crystal field stabilisation energy, most TM ions are more inclined to incorporate into octahedral or distorted octahedral symmetry rather than tetrahedral symmetry. The exception is high-spin d^5 ions as well as d^0 and d^{10} ions, with no particular preference for octahedral or tetrahedral sites. In turn, ions such as Cr^{3+}, Mn^{4+} and Ni^{2+} almost never will incorporate into tetrahedral sites [22,56].

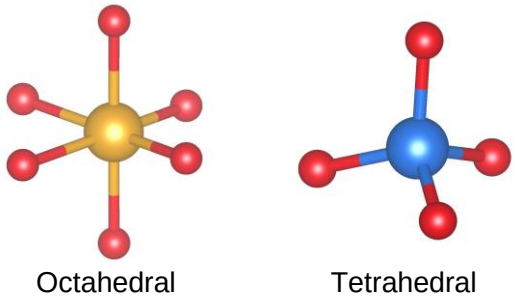

Fig. 1.4. *Octahedral and tetrahedral molecular geometries.*

1.5.1. Tanabe-Sugano diagrams

To determine the positions of energy levels of the TM ions in the crystal field, the Tanabe-Sugano diagrams for different d^n electron configurations are used [57,58].

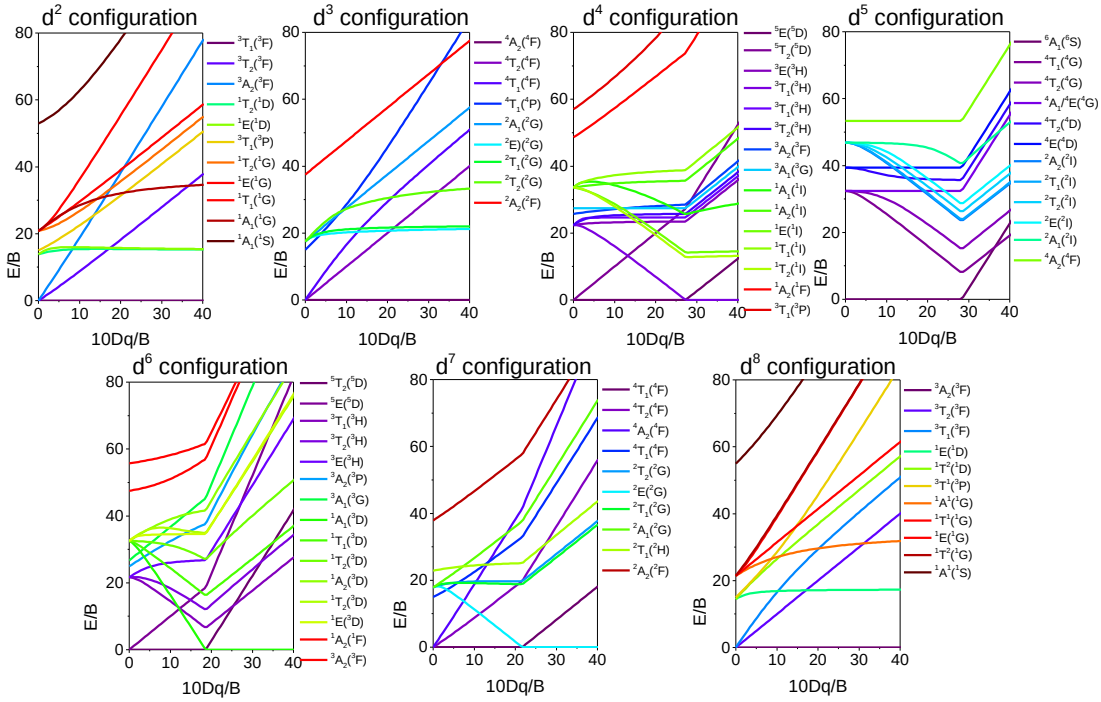

Fig. 1.5. *Simplified Tanabe-Sugano diagrams for octahedral complexes with d^2, d^3, d^4, d^5, d^6, d^7, and d^8 electron configuration.*

Tanabe and Sugano acquired the determinants of the electron configuration interaction for the d^2 to d^8 configurations in an octahedral field and presented TM ionic energy levels depending on the crystal field strength in the Tanabe-Sugano diagrams. On the x-axis of Tanabe-Sugano diagrams is the crystal field splitting parameter – *Dq*, scaled by the Racah parameter *B*. At the same time, the y-axis represents energy *E*, also scaled by *B*. Racah parameter represents an approximation of the bond strength between the anion and TM ion. Tanabe-Sugano diagrams for octahedral complexes with d^2 – d^8 electron configurations are shown in **Fig. 1.5**.

For tetrahedral coordination, the same diagrams may be used with the caveat that the diagram for a d^n tetrahedral configuration will apply to the diagram for a $d^{(10-n)}$ octahedral configuration [48,59].

1.5.2. Chromium

Chromium can be found in +1, +2, +3, +4, +5, and +6 states, with the Cr^{3+} being the most stable and common. The partially filled d-shell of Cr^{3+} provides strong visible light absorption, primarily due to transitions between the energy levels within $3d^3$ configurations. Cr^{3+} ions typically show intense PL ranging from 650 to 1200 nm, making Cr^{3+} the ideal luminescent centre for most red and especially near infra-red (NIR) emitting materials [60].

Like all TM elements, Cr^{3+} is strongly affected by the crystal field of the host material [6]. If Cr^{3+} is in strong crystal field conditions, mainly spin forbidden $^2E(^2G) \rightarrow {}^4A_2(^4F)$ transition occurs, resulting in relatively narrow luminescence bands. On the other hand, when Cr^{3+} is in weak crystal field conditions, broadband luminescence is expected due to the spin allowed $^4T_2(^4F) \rightarrow {}^4A_2(^4F)$ transition. In many cases, both narrow and broadband emissions of Cr^{3+} luminescence are observed. In this case, one can assume that an intermediate crystal field is present, and there is thermal equilibrium between the $^2E(^2G)$ and $^4T_2(^4F)$ states [61].

The simplified Tanabe-Sugano diagram of Cr^{3+} ion energy levels in the octahedral coordination is shown in **Fig. 1.6.** Crystal field is considered weak in the case of $Dq/B < 2.3$, strong in the case of $Dq/B > 2.3$ and intermediate if $Dq/B \approx 2.3$ [62,63]. Arrows represent electronic transitions leading to broadband or narrow band emission of Cr^{3+}.

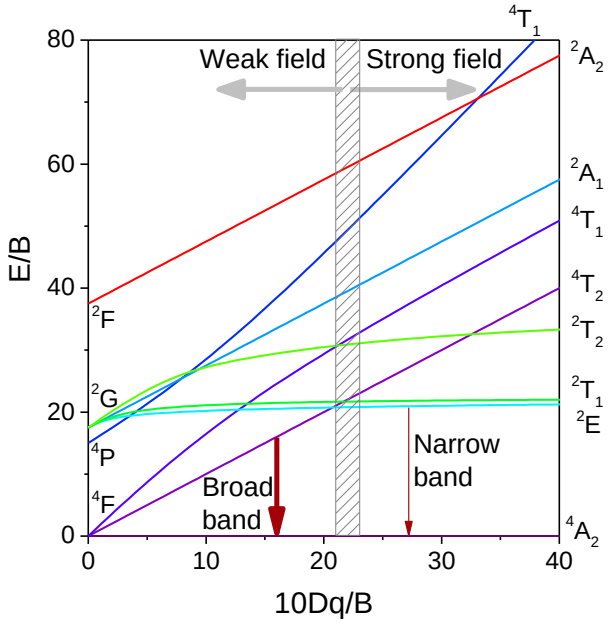

Fig. 1.6. *Simplified Tanabe-Sugano diagram of Cr^{3+} ions in octahedral crystal field. The arrows represent broadband emission in the weak crystal field and narrow band in the strong crystal field.*

The crystal field parameters of Cr^{3+} and other d^3 ions, such as Mn^{4+}, can be estimated using the following equations [64]:

$$Dq = \frac{E_1}{10} \tag{1.16}$$

$$x = \frac{E_2 - E_1}{Dq} \tag{1.17}$$

$$\frac{Dq}{B} = \frac{15(x-8)}{x^2 - 10x} \tag{1.18}$$

Here E_1 corresponds to the peak energy of the excitation band $^4A_2(^4F) \rightarrow {}^4T_2(^4F)$, and E_2 corresponds to the peak energy of the excitation band $^4A_2(^4F) \rightarrow {}^4T_1(^4F)$.

1.5.3. Manganese

The most common forms of manganese are Mn^{2+}, Mn^{3+}, Mn^{4+}, Mn^{6+} and Mn^{7+}; however, all oxidation states from -3 to +7 can be found. Of these, the most stable is Mn^{2+}. The luminescence properties of manganese have been mostly explored for Mn^{2+}, Mn^{3+}, Mn^{4+}, and Mn^{5+}, with Mn^{2+} and Mn^{4+} being the most well researched [65]. In general, manganese is one of the most promising activators for red-emitting phosphors [27,66,67]. The Mn^{4+} ions tend to occupy highly symmetrical octahedral sites with relatively strong local crystal field and generate deep red emission with sharp peaks, typically in the 620 – 720 nm range [65,68]. Mn^{4+} is a d^3 ion, thus, is characterised by the same Tanabe-Sugano diagram as Cr^{3+} (**Fig. 1.6.**), and for crystal field parameter evaluation, *Eq. (1.16 –1.18)* can be used.

On the other hand, Mn^{2+} has the d^5 electron configuration. As mentioned, the Tanabe-Sugano diagram for a d^n tetrahedral configuration will apply to that for a $d^{(10-n)}$ octahedral configuration, which means that Mn^{2+} will be characterised by the same diagram in both octahedral and tetrahedral symmetry. The same $^4T_1(^4G) \rightarrow {}^6A_1(^6S)$ transition can result in a widely different emission colour depending on molecular geometries in the material. The colour of Mn^{2+} emission in a strong field environment, such as an octahedral configuration, is red or even NIR [14]. In contrast, green emission appears in a weak field typically expected with a tetrahedral configuration. In all cases, broad featureless luminescence bands are expected [69].

A simplified Tanabe-Sugano diagram for d^5 electron configuration with representative arrows of emission is shown in **Fig. 1.7.** For d^5 elements, the energies of the $^4E(^4D)$ and $^4A_1,{}^4E(^4G)$ states relative to the $^6A_1(^6S)$ ground state is insensitive to the *Dq* and determined only by the *B* [70]. Thus, the Tanabe-Sugano diagram for Mn^{2+} may be constructed according to *Eq. (1.19)* [71–73].

$$B = \frac{94\alpha + \sqrt{49(E_3 - E_4)^2 - 768\alpha^2}}{49} \tag{1.19}$$

Here α - the Trees correction with free ion value of 76 cm^{-1}, E_3 and E_4 represent energies of $^6A_1(^6S) \rightarrow {}^4E(^4D)$ and $^6A_1(^6S) \rightarrow {}^4A_1,{}^4E(^4G)$ transitions, respectively.

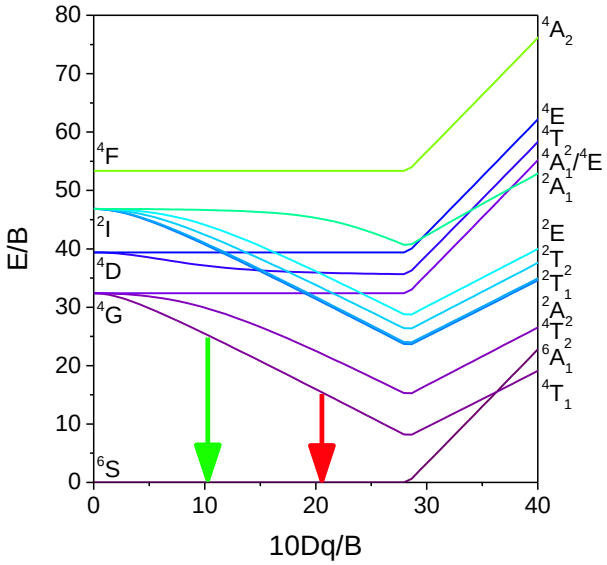

Fig. 1.7. *Simplified Tanabe-Sugano diagram of Mn^{2+} ions in octahedral and tetrahedral crystal field. The arrows represent green emission typical of Mn^{2+} in tetrahedral crystal field and red emission in octahedral crystal field.*

2. LITERATURE REVIEW

2.1. Overview of persistent luminescence materials

There was no significant scientific interest in the PersL phenomenon until the 1990s. However, since then, as evident from **Fig. 2.1.**, the number of publications on the topic has rapidly grown. Currently, it is possible to find publications on several hundred combinations of materials and activators, of which about 20% use Eu^{2+} or Eu^{3+} in combination with some other activator [74,75].

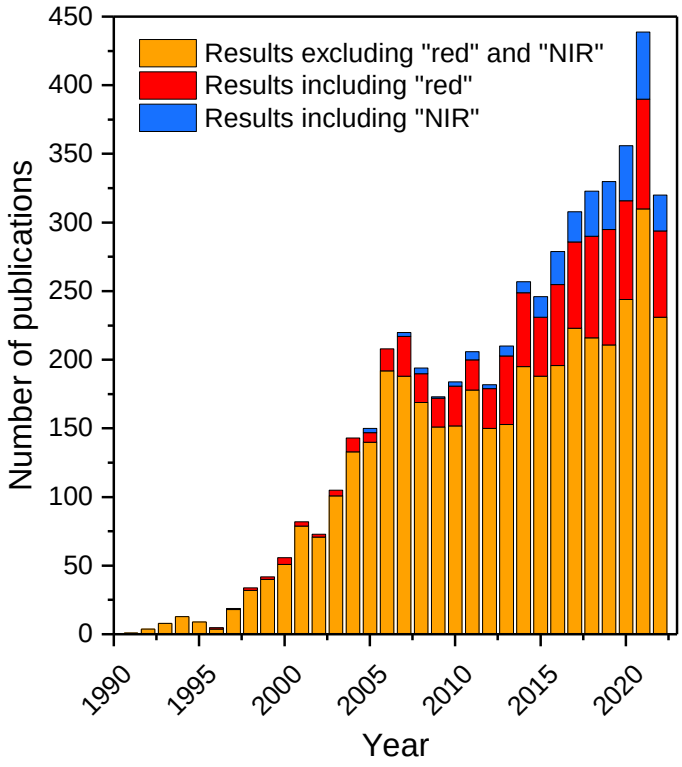

Fig. 2.1. *Number of publications on PersL in the Web of Science (accessed September 05, 2022). Search terms: "persistent luminescen*" OR "long afterglow" OR "long lasting phosphorescen*" OR "persistent phosphor*". The exact keywords were used together with "red" or "NIR" as well.*

The common host materials for PersL phosphors are oxides, silicates, aluminates, nitrides, germanates, gallates, etc. As dopants, typically, RE ions (e. g., Ce^{3+}, Eu^{2+}, Eu^{3+}, Tb^{3+}, Nd^{3+}, Pr^{3+}, Ho^{3+} Sm^{3+}, Tm^{3+}, Yb^{3+}, Dy^{3+}), TM ions (e. g., Cr^{3+}, Mn^{4+}, Mn^{2+}, Ni^{2+}, Fe^{3+}, Ti^{3+}) or post-transition group ions (e. g., Bi^{3+}, Pb^{2+}), are used [75,76].

Up to now, there are established PersL phosphors for each of the primary colours, with the representative ones including Y_2O_2S: Eu^{3+}, Mg^{2+}, Ti^{4+} (red) [77], $SrAl_2O_4$:Eu^{2+}, Dy^{3+} (green) [13] and $CaAl_2O_4$:Eu^{2+}, Nd^{3+} (blue) [78]. However, compared to the blue and green emitting PersL materials, there are far fewer reports on red phosphors, with most of them still at the research and development stage, with unsatisfactory luminescence lifetime, intensity and other properties necessary for practical applications [53].

In addition to VIS emitting PersL phosphors, “invisible” UV and NIR emitters are also in demand. Right now, arguably, the best NIR PersL phosphor is Cr^{3+} doped $Zn_3Ga_2Ge_2O_{10}$ with reported emission for more than 360 h [79]. Because of their promising applications in biomedicine, interest in NIR PersL phosphors has rapidly increased over the last ten years. In turn, materials demonstrating long afterglow in UV are much less common, and publications on them have emerged in the last few years.

Fig. 2.2. shows an overview of emission wavelengths of most of the reported dopant ions in PersL phosphors. Note that the used values are an approximation, and some variations may occur depending on the host.

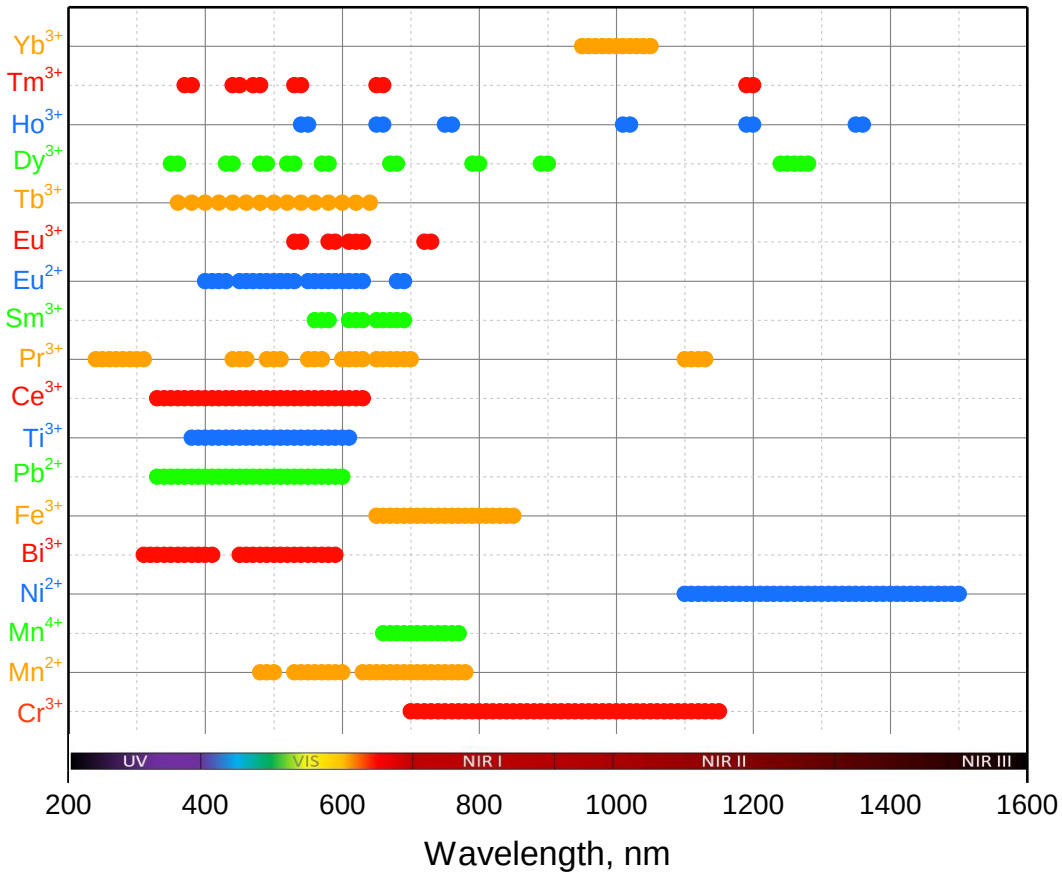

Fig. 2.2. *Overview of emission wavelengths of most reported dopant ions in PersL phosphors.*

2.2. Applications and future perspectives for PersL materials

Right now, the best-known applications of PersL phosphors are somewhat trivial: “glow-in-the-dark” toys, luminous paints for decorations and watches, etc. Probably the most important and recognised commercialised application is safety signs in buildings and aeroplanes that persist to glow in the case of a complete lack of power [80,81]. In addition to these, a wide variety of other potential applications, such as bioimaging [82,83], road markings [84,85], fingerprint detection [86,87], and anti-counterfeiting [88,89], among others, have been suggested throughout the years.

The most reported applications of PersL phosphors are listed in **Fig. 2.3**. These are in various stages of development for practical use and will be outlined in the following subsections.

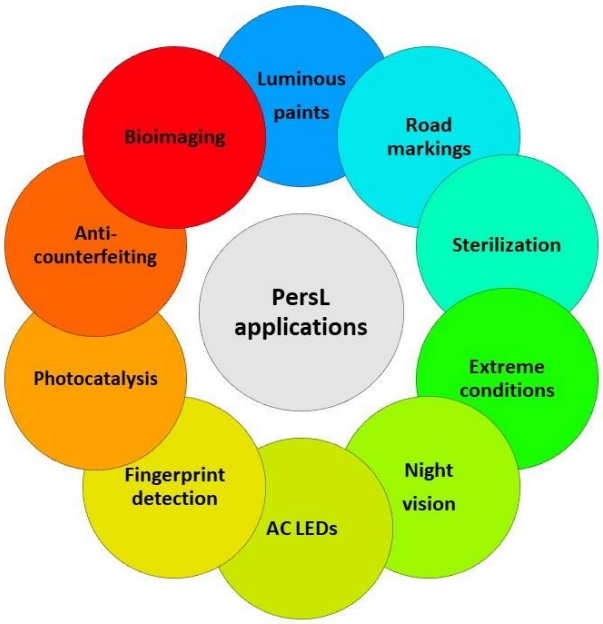

Fig. 2.3. *Overview of the most reported applications of PersL phosphors.*

2.2.1. Luminous paints

Fundamentally, luminous paints are composites made from PersL phosphors and emulsions in which fillers and additives are supplemented in the desired ratio. The first widely used synthetic phosphorescent pigment was green emitting copper doped zinc sulphide (ZnS: Cu^{2+}), which was discovered in the 1930s [90]. It dominated the market for decades until the discovery and commercialisation of Eu doped aluminates ($SrAl_2O_4$: Eu^{2+}, Dy^{3+} etc.), which are safer, chemically stable and emit no harmful radiation [42].

2.2.2. Road markings

Currently, standard road markings are paints, dispersions, thermoplastics, and films that reflect light. However, reflection-based markings, by definition, always need light from the moving car and therefore do not work at large distances. The idea of using luminous road markings has been introduced; however, widespread adaptation of them is still quite challenging [91].

Firstly, while applications such as toys, watch dials, emergency signs, etc., are primarily used indoors with somewhat constant and predictable temperature, and excitation intensity, luminophores used for outdoor applications must perform under very variable conditions. Since the typical PersL mechanism is based on the thermal release of trapped electrons, the performance of the road markings is strongly affected by weather – they may glow brighter but for a shorter period on warm summer nights, while the emission in cold winters may be neglectable altogether. Secondly, charging strongly depends on the

availability of sunlight; thus, road markings may not work as intended on cloudy/foggy days and following nights [81,84].

2.2.3. UV sterilisation

The use of UV light for sterilisation and reduction of the transmission of pathogens has been known since the late 19th century. Today, UVC radiation (200 – 300 nm) is widely used as a disinfectant for air, water, and non-porous surfaces in numerous commercial, industrial, and residential disinfection systems. Absorption of UVC light destroys the ability to replicate the nucleic acid of many types of germs, leading to cell death in bacteria and inactivation in viruses. Typical sources of UVC light are UV lamps, such as low-pressure Hg lamps, pulsed Xe lamps and UVC LEDs [92,93].

Last few years, an increased interest in UVC emitting PersL phosphors has arisen for their potential application in sterilisation. Several Pr^{3+} doped PersL phosphors, for example, Li_2CaGeO_4 [94], Lu_2SiO_5 [95], and $BaLu_2Al_2Ga_2SiO_{12}$ [96], have been proposed. In laboratory settings, it has already been proven that the afterglow UVC PersL phosphors are sufficient to inactivate several types of bacteria, e.g. *Staphylococcus aureus* (the leading cause of skin and soft tissue infections) [94] and *Pseudomonas aeruginosa* (can cause infections in the blood, lungs or other parts of the body) [97] and research interest of PersL phosphors for sterilisation purposes is rapidly increasing.

2.2.4. Extreme conditions

For different applications of PersL phosphors, it is vital to obtain a material with an optimal trap depth so that there is a good compromise between the initial intensity and decay time of the afterglow. For RT, it is reported to be around 0.7 – 0.8 eV [5,23], while for *in vivo* bioimaging in the human body, traps may be deeper since the core temperature is within a range of 36.5 – 38.5 °C.

On the other hand, some PersL materials have very deep traps that remain filled for weeks or months at RT and can be emptied in high temperature conditions, such as 200 °C or even higher. Thus, they are widely used for personal thermoluminescence dosimeters in various fields [81].

In the case of extremely shallow traps, PersL phosphors can be used in cryopreservation, biological labelling, etc. In these cases, PersL phosphor is charged at low temperature, typically liquid nitrogen temperature. If temperature increases, trapped charge carriers may escape. From here, either the PersL signal can be detected directly, or the PersL phosphor-based seal may be checked after any storage time to assess whether there has been an increase in temperature [98,99].

2.2.5. Night vision surveillance

For the last few years, night vision surveillance has been mentioned as an emerging possible application for NIR PersL phosphors. Since NIR radiation is invisible to the naked eye, NIR PersL paints can be used to tag different police, military, etc., equipment for tracing, positioning, and identification in the dark. Liu *et al.* [100] have recently

demonstrated $LaZnAl_{1.5}Ga_{9.5}O_{19}$: Cr^{3+}, Yb^{3+} based NIR PersL tag, that after UV excitation for 5 min, can be easily detectable by night vision monocular even after 10 h. Thus, proving the concept of sunlight charged, power free, and maintenance free night-time surveillance.

2.2.6. Flickering reduction in AC-LEDs

Light emitting diode (LED) based light sources have high luminous efficacy and, compared to conventional lighting sources such as incandescent bulbs or fluorescent tubes, have a significantly longer lifetime [101]. Currently, the market is dominated by DC-LEDs (direct current LEDs) equipped with driver electronics to convert alternating current (AC) from the electricity network to DC. This yields several problems. Firstly, AC to DC conversion significantly (≈ 30%) increases electric power consumption. Secondly, the general lifetime of the DC-LED bulb decreases since the lifetime of the capacitor series in the converter is around 50 times shorter than that of an LED itself [102]. As an obvious solution, the use of AC-LED bulbs is proposed. However, due to the 50 or 60 Hz AC frequency, an unavoidable flicker in every AC cycle is expected. Exposure to flickering light is a health hazard that may induce photosensitive epileptic seizures, headaches, etc. [103,104].

It has been recently offered that the dark periods may be bridged with the afterglow of PersL phosphors. In this case, afterglow time does not have to exceed a few tens of milliseconds; thus, the trap depth must be shallow. Additional requirements are: appropriate emission colour and excitation wavelength should match the blue region of the commercial InGaN chip that is the base of LED bulbs [105,106].

2.2.7. The detection of fingerprints

The detection and analysis of fingerprints are one of the most critical parts of forensic investigation. Since the 1970s, nanophosphor powders have been widely used with the powder dusting technique that involves adherence of the powder particles to fingerprint ridges. Then nanophosphor is excited under UV light, and the contrast between the fingerprint profile and the background surface provides a fingerprint picture [107]. The main problem of this technique is the background fluorescence signal from the surface. As a solution, it is proposed that the signal of powder is collected after the background fluorescence disappears. For this purpose, PersL phosphors have been suggested; however, their use for this purpose is not common yet [108–110].

2.2.8. Round-the-clock photocatalysis

Photocatalysis is the acceleration of chemical reactions under the influence of optical radiation (UV, VIS, NIR) in the presence of a catalyst – photocatalytic material. Photocatalytic technology has attracted substantial interest in fields such as CO_2 reduction, organic pollutants degradation, hydrogen or oxygen production from water-splitting, water waste purification, etc. [111,112]. For the photocatalytic activity to occur, photocatalytic material must be exposed to an external irradiation source; thus, photocatalysis does not happen in a dark environment.

To overcome this restriction, for the last decade, there has been increased interest in using PersL phosphors combined with photocatalysts [81]. There is a plethora of research demonstrating that the addition of PersL phosphor improves photocatalysis. However, the mechanism is unclear. A reasonable guess would be that PersL acts as a source of light even when external lighting is unavailable. At the same time, charge transfer processes between PersL phosphor and photocatalyst may occur, or both mechanisms operate simultaneously [76,112].

2.2.9. Anti-counterfeiting

The conventional luminescence-based anti-counterfeiting markings are invisible or lightly coloured under normal conditions and emit visible light under excitation. A typical example would be Euro banknotes that utilise the luminescence of RE ions for anti-counterfeiting purposes. Although widely applied, traditional anti-counterfeiting luminescent materials exhibit multiple shortcomings: typically, single, or dual-mode emission excited either by UV or NIR is used, and the luminescence is visible only at the time of excitation, making it susceptible to the interference of background created by an excitation source. Additionally, similar emission characteristics can be imitated by mixing different easily purchasable luminescent materials; thus, poor anti-counterfeiting performance is achieved [76,88].

Recently, immense attention has been paid to combining three or more luminescent modes in a single material. For this purpose, one of the most perspective classes of materials is PersL phosphors. The complex nature of the PersL mechanism makes PersL phosphors excellent candidates for advanced anti-counterfeiting applications. Firstly, due to charge carrier trapping by different traps with various depths, it is possible to obtain different thermally stimulated luminescence (TSL) and optically stimulated luminescence (OSL) patterns with emissions within a broad colour range. Secondly, since light emission follows long after the removal of the excitation source, PersL has a much higher signal-to-noise ratio than PL. Furthermore, multi-stimuli-responsive and multi-mode emission properties are more difficult for counterfeiters to replicate; thus, high security anti-counterfeiting performance can be achieved [113–116].

2.2.10. Bioimaging

The most mentioned application of NIR PersL phosphors for the last decade is bioimaging and related biological applications [66]. The appeal of NIR PersL materials lies in the fact that biological tissues strongly absorb UV and VIS optical radiation. Only those materials that emit or absorb radiation in the so-called biological window areas can be considered practical. Biological windows correspond to the following spectral ranges: first biological window 700 nm – 950 nm, second biological window 1000 nm – 1350 nm and third biological window 1550 nm – 1870 nm [117]. Low optical scattering and absorption in tissues within these windows enable deep-tissue imaging. Therefore, emission in the NIR region is highly desirable for *in vivo* imaging. Currently, most markers used for bioimaging are organic materials, which have poor photochemical stability and are prone to photobleaching and photodegradation. Compared to other non-persistent biomarkers, the

PersL phosphors stand out for their ability to be excited before injection into a biological specimen. Therefore, bioimaging can be realised without further excitation, thus, practically eliminating issues of autofluorescence of tissues and protecting the specimen from potentially harmful excitation effects [118–120].

2.3. Strategies to design PersL phosphors

There are several aspects to keep in mind when designing PersL phosphor. Firstly, choosing an optimal host and activator combination with desirable absorption and emission, suitable band gap, and appropriate traps is necessary. Secondly, an appropriate synthesis method (solid state synthesis, sol-gel, hydro-thermal method, etc.) and conditions must be chosen. In the case of solid state synthesis, a synthesis atmosphere may play a significant role, especially when working with oxygen rich hosts. Synthesis in the reducing atmosphere or vacuum promotes the formation of oxygen vacancies which typically serve as trapping centres [121–124].

Lastly, there are several different routes to enhance the PersL properties of already known materials. The most mentioned are co-doping, band gap engineering and persistent energy transfer.

Fig. 2.4. summarises the basic aspects to consider when designing a PersL material.

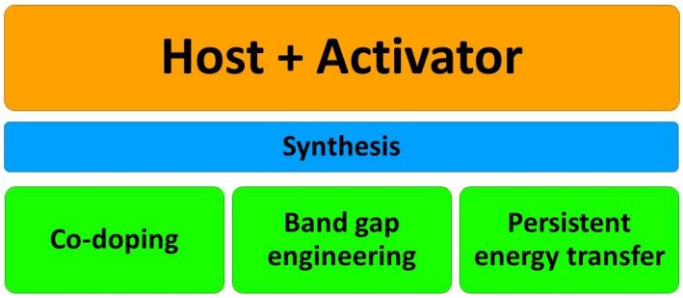

Fig. 2.4. *Basic aspects important for designing persistent phosphors.*

2.3.1. Co-doping

Co-doping is the most used method for developing exceptional PersL phosphors. There are three approaches:

- *Co-doped ion act as a trapping centre*. For this purpose, trivalent RE ions are widely used. For example, in the case of well-known $SrAl_2O_4$: Eu^{2+}, Dy^{3+}, the luminescence centre is $Eu^{2+,}$ and incorporation of Dy^{3+}, which serves as the trapping centre, into the system significantly increases its afterglow time [78].
- *Aliovalent substitution*. If ions with different charges substitute the cations or anions in the host, additional defects will be produced to ensure charge compensation. Further, these defects may serve as trapping centres [125,126].

- *Enhanced trapping efficiency*. Co-dopants with a higher transition rate can be used as electron "pumps" that increase the number of electrons in CB and subsequently in the trapped state [127].

2.3.2. Band gap engineering

Band gap engineering refers to the change of the band gap energy E_g typically by modifying the host composition to obtain optimal optical and/or electronic characteristics for the desired purpose. For example, band gap engineering has been proven to be a highly effective strategy to improve scintillation performances in $RE_3Al_5O_{12}$ garnet scintillators [128,129] etc. Here hosts such as yttrium−aluminium garnet ($Y_3Al_5O_{12}$) are modified by replacing the smaller cation Al^{3+} with larger Ga^{3+}. The typical formula for this is $Y_3Al_{5-x}Ga_xO_{12}$, where x changes from 0 to 5. The introduction of Ga^{3+} leads to the distortion of the crystal structure, thus, changing the electronic structure of the system, including the band gap. In the case of scintillators, the aim usually is to remove shallow electron traps (e.g., oxygen vacancies or anti-site defects) by "swallowing" them into CB. On the other hand, the same strategy has recently been used to design novel PersL phosphors. By varying the E_g value, it is possible to change the energy gap from the excitation level of the activator to CB or electron trap to CB, thus acquiring desired PersL properties [130–132].

2.3.3. Persistent energy transfer

The persistent energy transfer strategy is used if the desired luminescence centre (acceptor) does not show PersL. As a solution, it is proposed to use an established PersL phosphor with a luminescence centre (donor) that emits light in the spectral range where the acceptor can be excited. Thus, the PersL of the donor converts to the PersL of the acceptor [53]. Donor in these cases can be either a co-activator or host related luminescence centre. Examples of persistent energy transfer are NIR phosphor $ZnGa_2O_4$: Cr^{3+}, Yb^{3+} [133] where energy transfer $Cr^{3+} \rightarrow Yb^{3+}$ occurs, UV phosphor $(Y,Gd)_3Ga_5O_{12}$:Bi^{3+} [134] with $Bi^{3+} \rightarrow Gd^{3+}$ energy transfer, $SrGa_{12}O_{19}$: Cr^{3+} [135] with host $\rightarrow Cr^{3+}$ energy transfer and many more.

2.4. Activators and hosts in this work

2.4.1. Persistent luminescence of Mn^{2+} activated materials

Red light covers a spectral region with wavelengths from 625 to 740 nm and is perceived by the human eyes. At present, the most prominent red light-emitting PersL materials are Y_2O_2S: Eu^{3+}, Mg^{2+}, Ti^{4+} [77], $Ca_{1-x}Sr_xS$: Eu^{2+} [136] and others [137–139]. As luminescence centres in these materials, RE ions such as Eu^{2+} and Sm^{3+} are typically used. In the case of red PersL, the best alternatives for RE ions are Mn^{2+} and Mn^{4+}. In the context of this work, further attention will be paid to Mn^{2+} activated PersL materials. A selected number of Mn^{2+} activated PersL phosphors are presented in *Table 2.1*.

As evident from *Table 2.1.*, a wide variety of hosts, such as aluminates, silicates, germanates, etc., may be used to obtain Mn^{2+} doped PersL materials. However, as previously

mentioned, the colour of emission of Mn^{2+} is strongly affected by the local crystal field, thereby limiting the number of potential hosts for red PersL material.

Table 2.1. Selection of Mn^{2+} activated PersL phosphors.

	Host	***Co-activator***	***Lum. band maximum***	***Lum. colour***	***Duration***	***Year***	***Ref.***
Aluminates	$Ca_2Sn_2Al_2O_9$		565 nm	yellow	> 7 h	2020	[140]
	$CaAl_2O_4$	Ce^{3+}	520 nm	green	up to 24 h	2003	[141]
Silicates	$BaMg_2Si_2O_7$	Ce^{3+}	680 nm	red	> 16 h	2012	[142]
	$CdSiO_3$	Y^{3+}, La^{3+}, Gd^{3+}, Lu^{3+}	580 nm	orange	> 15 min	2006	[143]
	$MgSiO_3$	Eu^{2+}, Dy^{3+}	660 nm	red	up to 24 h	2003	[141]
	$Ca_2Al_2SiO_7$	Ce^{3+}	550 nm	green	up to 24 h	2003	[141]
Germanates	Na_2ZnGeO_4		525 nm	green	> 4 h	2015	[144]
	$(Mg,Zn)GeO_3$	Eu^{3+}, Yb^{3+}	670 nm	red	> 1 h	2018	[145]
	Zn_2GeO_4		535 nm	green	> 1.5 h	2019	[146]
	$MgGeO_3$		680 nm	red	> 15 h	2021	[147]
	$CaZnGe_2O_6$		650 nm	red	> 1 h	2008	[148]
Gallates	$ZnGa_2O_4$		505 nm	green	up to 1 h	2019	[149]
	$(Ca, Sr)Ga_4O_7$	Bi^{3+}	556 ↔ 580 nm	green ↔ yellow	> 20 h	2019	[150]
Phosphates	$Zn_2(PO_4)_3$	Sm^{3+}	620 nm	red	> 10 min	2005	[151]
	$Zn_3(PO_4)_2$	Ga^{3+}	616 nm	red	> 10 min	2007	[152]
	$Ca_3(PO_4)_2$		670 nm	red	> 1 h	2013	[153]
Other	$NaCa_2GeO_4F$	Li^+, Al^{3+}, N^{3-}, Ga^{3+}, B^{3+}, Mg^{2+}, F^-, Bi^{3+}, Zn^{2+}, Cd^{2+}, Sc^{3+}, Tm^{3+}	568 ↔ 627 nm	green ↔ red	up to 60 h	2016	[154]
	AlN		600 nm	red	> 2 h	2017	[155]

2.4.2. Persistent luminescence of Cr^{3+} activated materials

Cr^{3+} is considered an ideal activator for NIR phosphors. As host materials for Cr^{3+}-activated persistent phosphors, mostly gallates and gallogermanates have been researched since the incorporation of Cr^{3+} into octahedral Ga^{3+}(IV) site yields emission from 650 to 1000 nm. More importantly, these compounds typically contain an abundance of charge traps with suitable trap depths for PersL at RT [156]. Nevertheless, different hosts, such as

aluminates, stannates and germanates, are also considered. A selected number of Cr^{3+} activated PersL phosphors are presented in *Table 2.2*.

Table 2.2. Selection of Cr^{3+} activated long afterglow phosphors.

	Host	**Lum. band**	**Band type**	**Duration**	**Year**	**Ref.**
Aluminates	$ZnAl_2O_4$	670 – 730 nm	narrow	> 120 h	2018	[157]
	$Ca_{14}Zn_6Al_{10}O_{35}$	670 – 730 nm	narrow	> 1 h	2016	[158]
	$LaAlO_3$	670 – 730 nm	narrow	> 2 h	2015	[159]
Stannates	Mg_2SnO_4	700 – 1000 nm	broad	> 100 h	2021	[62]
	$Mg_{1.4}Zn0.6SnO_4$	675 – 850 nm	broad	> 3 h	2021	[160]
	$Zn_3Ga_2Sn1O_8$	660 – 750 nm	narrow	> 5 h	2014	[161]
	Zn_2SnO_4	700 – 1000 nm	broad	> 35 h	2015	[162]
Gallates	$LiGa_5O_8$	650 – 750 nm	narrow	> 120 h	2013	[163]
	$ZnGa_2O_4$	650 – 750 nm	narrow	> 3 h	2013	[164]
	$SrGa_{12}O_{19}$	650 – 950 nm	narrow + broad	> 2 h	2014	[135]
	$MgGa_2O_4$	600 – 750 nm	narrow	> 1 h	2017	[165]
	$Ca_{14}Zn_6Ga_{10}O_{35}$	650 – 750 nm	narrow	> 3 h	2016	[23]
Gallo-germanates	$Mg_4Ga_4Ge_3O_{16}$	700 – 1000 nm	broad	> 10 h	2019	[166]
	$Mg_3Ga_2GeO_8$	700 – 800 nm	narrow	> 15 h	2019	[167]
	$Li_5Zn_8Ga_5Ge_9O_{36}$	700 – 900 nm	narrow + broad	> 12 h	2019	[168]
	$Mg_4Ga_8Ge_2O_{20}$	650 – 1000 nm	narrow + broad	> 25 h	2016	[169]
	$Ca_3Ga_2Ge_3O_{12}$	700 – 1000 nm	broad	> 2 h	2017	[170]
	$Zn_3Ga_2Ge_2O_{10}$	650 – 800 nm	narrow + broad	> 360 h	2012	[79]
Germanates	$Mg_3Y_2Ge_3O_{12}$	700 – 1000 nm	broad	≈ 3 h	2021	[171]
	$Mg_3Y_2Ge_3O_{12}$	700 – 1100 nm	broad	> 2 h	2020	[172]
	$CaZnGe_2O_6$	700 – 1200 nm	broad	> 3 h	2018	[173]
	$Li_5Zn_8Al_5Ge_9O_{36}$	670 – 780 nm	narrow	> 12 h	2017	[174]
	$MgGeO_3$	700 – 1200 nm	broad	> 16 h	2022	[175]
Other	$Na_2CaGe_5SiO_{14}$	600–900 nm	broad	> 10 h	2020	[63]
	Sr_2MgWO_6	700 – 1000 nm	broad	> 2 h	2019	[176]
	Ca_2MgWO_6	700 – 1000 nm	broad	> 2 h	2018	[177]

2.4.3. $MgGeO_3$-based luminescent materials

The structure of $MgGeO_3$ is an analogue to Pbca enstatite. It consists of a three-dimensional network of $[GeO_4]$ tetrahedrons and two kinds of $[MgO_6]$ octahedrons: slightly distorted $[Mg(I)O_6]$ and more distorted $[Mg(II)O_6]$, which share joint edges. The volume of

the [Mg(II)O_6] site is marginally larger than [Mg(I)O_6] (12.180 and 12.048 $Å^{3,}$ respectively) [178]. The schematic crystal structure and its basic units are presented in **Fig. 2.5**.

The first report on $MgGeO_3$ as a possible host for PersL phosphor was published in 2003 by Iwasaki *et al.* [123]. They discussed Mn doped $MgGeO_3$, Mg_2GeO_4 and Mg_4GeO_6. Samples were prepared using a solid state synthesis method. It was concluded that of the three, $MgGeO_3$:Mn^{2+} has the best PersL properties. The red afterglow ≈ 600 – 750 nm with a maximum of 680 nm was observed for at least an hour.

Furthermore, it was found that the addition of the MgF_2 in the synthesis process will increase the initial intensity of the PersL up to 65 times. This effect was explained by the hypothesis that MgF_2 act as a catalyst for the formation of GeO; thus, the number of oxygen vacancies associated with Ge^{4+} ions increases, leading to improved PersL. Another material modification was done by adding a series of RE oxides. From here, it was concluded that the initial intensity of the Yb^{3+} doped sample increased approximately three times. This was explained by the tendency of the ytterbium ion to be in a divalent state, thus acting as an electron trap. The addition of other RE elements (Ce, Pr, Nd, Sm, Eu, Gd, Tb, Dy, Ho, Er, Tm) showed no improvement in the material's PersL properties. In the conclusions, the mechanism of red PersL in the $MgGeO_3$: Mn^{2+} was offered.

The above-mentioned publication has given a base for various research projects dedicated to $MgGeO_3$: Mn^{2+} based PersL materials. There has been an effort to further increase the intensity and longevity of the PersL by co-doping with a combination of Yb^{3+} and Eu^{3+} [179] or Bi^{3+}[180]. Since Mn^{2+} doped Zn_2GeO_4 material is characterised by green emission, there have been multiple successful attempts to create Mn^{2+} doped Zn-Mg-Ge-O long afterglow systems with green-yellow-red tuneable emission [145,181,182].

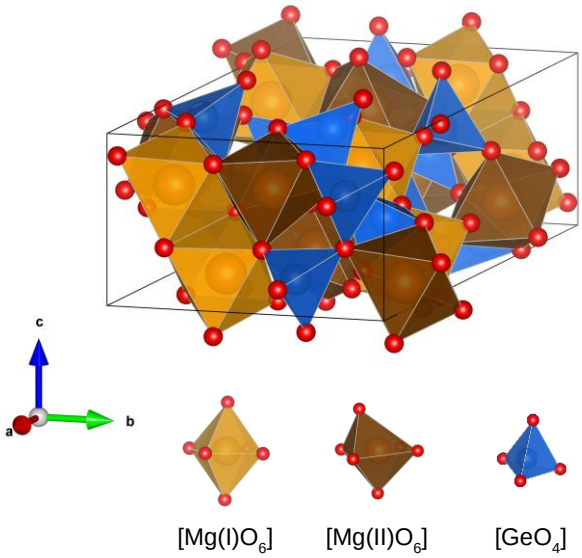

Fig. 2.5. *Crystal structure of the $MgGeO_3$ material and polyhedron of Mg^{2+} and Ge^{4+}.*

Recently there have been reports on $MgGeO_3$: Mn^{2+} based materials that could be used for bioimaging and optical information storage applications [183,184]. Possibly the most intriguing research comes from Zhang *et al.* 2020 publication [184], where they have designed PersL nanoparticles of $MgGeO_3$: Mn^{2+}, Yb^{3+}, Li^{+} with emission in the first and second

biological windows. Nanoparticles with a diameter of 50-100 nm were synthesised by the sol-gel method and proved suitable for bioimaging applications. *In vivo* test results showed that, when modified with folic acid, $MgGeO_3$: Mn^{2+}, Yb^{3+}, Li^{+} nanoparticles can effectively realise long-term targeted imaging of inflammatory. Additionally, nanoparticles can be recharged with soft X-rays and NIR lasers.

There are some reports of PersL in exclusively RE doped $MgGeO_3$. Dopants such as Pr^{3+} and Yb^{3+} have been considered [185,186]. These materials are characterised by strong emissions in red and NIR spectral regions, respectively.

Besides PersL, two reports on PL of $MgGeO_3$-based materials have been recently published. One focused on electron-transfer quenching in red-emitting Pr^{3+} doped $MgGeO_3$ material [187]. Other discuss the potential application of orange-red emitting $MgGeO_3$: Sm^{3+} in warm white light emitting devices [188].

The Author of this dissertation is the primary investigator and corresponding author of two publications devoted to $MgGeO_3$-based PersL materials. Corresponding references: Ref. [147] and Ref. [175]. The findings will be discussed in detail in the Results and Discussion part of this work.

2.4.4. Mg_2GeO_4 and Mg_2SiO_4-based luminescent materials

The crystal structure of the Mg_2SiO_4 and Mg_2GeO_4 compounds is illustrated in **Fig. 2.6**. There are three types of polyhedrons present in each structure: [GeO_4] or [SiO_4] tetrahedrons and two distinct [MgO_6] octahedrons. The two different cation octahedra form alternating chains parallel to the c axis. Although they have the same coordination, one of the octahedra ([Mg(II)O_6] in **Fig. 2.6**) is more distorted [189].

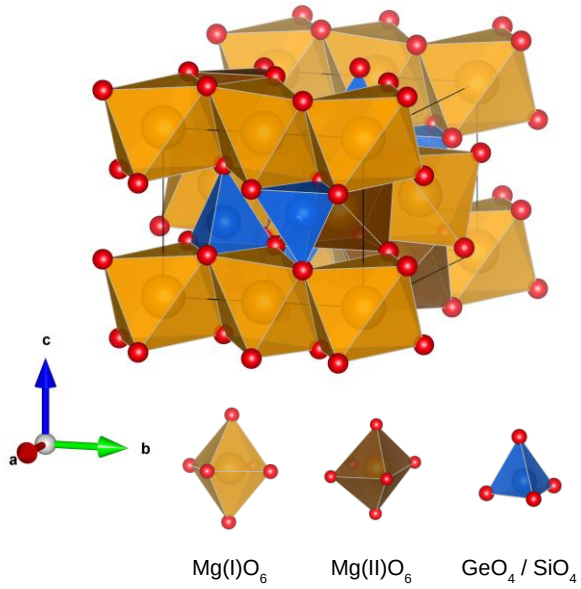

Fig. 2.6. *Crystal structure of Mg_2SiO_4 and Mg_2GeO_4 and polyhedron of Mg^{2+}, Si^{4+} and Ge^{4+}.*

Just as $MgGeO_3$, Mg_2GeO_4 was first considered a possible host for PersL phosphor by Iwasaki *et al.* [123]. The material was doped with manganese, and Mn^{2+} characteristic PersL bands were observed. Nevertheless, up to now, there is only one other report on Mg_2GeO_4 based PersL phosphor [124]. Here authors present a red PersL phosphor: Mg_2GeO_4: Mn^{4+} and claim that PersL originates from Mn^{4+} transition $^2E(^2G) \rightarrow {}^4A_2(^4F)$. This, however, contradicts not only results in Ref. [123] but also results analysed in the *Results and Discussion* section of this work, where it is shown that Mg_2GeO_4: Mn material can be characterised by the PersL of Mn^{2+}. Note that the same synthesis method was used in all three cases.

Besides, there are several reports on PL of RE, such as Eu^{3+} [190], Sm^{3+} [191], Tb^{3+} [192] doped Mg_2GeO_4 materials from the late 2000s.

Recently interest in Mg_2GeO_4 materials has resurfaced, and a couple of publications of Cr doped Mg_2GeO_4 materials have been published [193,194]. Here a broadband NIR PL has been discussed in detail as well as possible applications of the material as a light source for non-destructive analysis in food safety areas.

On the other hand, Mg_2SiO_4 phosphors have drawn broad interest from the scientific community since the 1990s. However, almost all the publications concentrate on PL instead of PersL. The most used dopant is Eu^{3+}; therefore, PL can be characterised by Eu^{3+} typical red luminescence with bands around 600 – 700 nm [107,195–198]. Other RE ions used in Mg_2SiO_4 phosphors are Tb^{3+} [199,200], Dy^{3+} [201,202], Sm^{3+} [203], etc. Mg_2SiO_4 has been reported as an appropriate host for several TM ions, such as Cr^{3+} [204,205], Ni^{2+} [206], V^{4+} [207] and Mn^{2+} [208,209].

The only report on PersL of Mn^{2+} doped Mg_2SiO_4 is the 2008 article by Lin *et al.,* where they report on a long-lasting red phosphor: Mg_2SiO_4: Dy^{3+}, Mn^{2+} [210]. They observed two overlapping broad emission bands with maxima around 645 and 723 nm, which were attributed to the optical transitions within Mn^{2+} ions substituting two non-equivalent Mg^{2+} sites. After removal of UV irradiation, the red afterglow of Mn^{2+} doped and Mn^{2+}/ Dy^{3+}co-doped samples was observed with the naked eye in the darkness for 6 and 17 min, respectively. Only the luminescence of Mn^{2+} was observed, and it was proposed that Dy^{3+} ions act as electron trap centres. No more details about the mechanism of PersL were suggested.

The Author of this dissertation is the primary investigator and corresponding author of a publication devoted to PersL properties of the manganese doped $Mg_2SiO_4 - Mg_2GeO_4$ solid solution. Corresponding reference: Ref. [211]. The findings will be discussed in detail in the Results and Discussion part of this work.

3. EXPERIMENTAL

3.1. Synthesis of samples

$MgGeO_3$: Mn^{2+}, $MgGeO_3$: Cr^{3+} and $Mg_2(Si_{1-x}Ge_x)O_4$: Mn samples were synthesised by a conventional solid state synthesis method. The base of the solid state synthesis method is a chemical reaction between powder-form precursors at high temperatures. It is the most used approach for preparing oxide, sulphide, and nitride-based phosphors due to its simplicity and suitability for mass production. Additionally, high temperature sintering can generally increase the population of intrinsic defects, which are essential for long afterglow generation in PersL materials [42].

During the synthesis, stoichiometric amounts of chemical compounds summarised in *Table 3.1.* were weighted and milled. To enhance the homogeneity of the mixture, wet milling was carried out in a non-polar solvent (analytically pure $CHCl_3$) that would not affect the chemical composition of the materials. After $CHCl_3$ was evaporated entirely, the mixture was ground in a marble mortar, transferred into a corundum crucible, and annealed:

- at 1250 °C for 2 h in either ambient or reducing (flux of N_2-H_2 mixture, 5% H_2) atmosphere to obtain polycrystalline $MgGeO_3$ materials doped with Mn^{2+};
- at 1250 °C for 2 h in an ambient atmosphere to obtain polycrystalline $MgGeO_3$ materials doped with Cr^{3+};
- at 1450 °C for 2 h in an ambient atmosphere to obtain polycrystalline $Mg_2(Si_{1-x}Ge_x)O_4$ materials doped with Mn.

A heating and cooling rate of 5 °C/min has been applied. After the synthesis, the samples were ground. For heat treatment, a high-temperature furnace Carbolite HTF18 was used.

Table 3.1. Chemical compounds used for the synthesis of $MgGeO_3$: Mn^{2+}, $MgGeO_3$: Cr^{3+} and $Mg_2(Si_{1-x}Ge_x)O_4$: Mn materials.

Materials	***Compounds***	***Purity***	***Manufacturer***
$MgGeO_3$:Mn^{2+}	$MgCO_3 \cdot Mg(OH)_2 \cdot 3H_2O$	99.996%	Alfa Aesar
	GeO_2	99.9999%	Alfa Aesar
	MnO_2	99.997%	Alfa Aesar
$MgGeO_3$:Cr^{3+}	$MgCO_3 \cdot Mg(OH)_2 \cdot 3H_2O$	99.9999%	Alfa Aesar
	GeO_2	99.997%	Alfa Aesar
	Cr_2O_3	99.999%	Alfa Aesar
$Mg_2(Si_{1-x}Ge_x)O_4$:Mn	$MgCO_3 \cdot Mg(OH)_2 \cdot 3H_2O$	99.996%	Alfa Aesar
	GeO_2	99.9999%	Alfa Aesar
	SiO_2		Alfa Aesar
	MnO_2	99.997%	Alfa Aesar

3.2. Structure analysis

The phase composition of prepared samples was studied with the powder X-ray diffraction (XRD) method. To obtain XRD patterns – the X-ray diffractometer Rigaku MiniFlex 600 was used. The general layout for measuring is shown in **Fig. 3.1**.

XRD is a common characterisation technique that allows for the identification of crystal orientations and interatomic spacing by using reflection and subsequent interference of one of the characteristic lines from the X-ray spectrum, typically K-alpha (for Cu cathode $\lambda_{K\alpha}$ = 1.5406 Å), together with the Bragg's law (*Eq. 3.1*).

$$n\lambda = 2d \sin\theta \tag{3.1}$$

Bragg's law describes the relationship for constructive interference in the case of X-rays with wavelength λ falling on the material at angle θ and being diffracted by crystal planes with the distance d between them. n here is the diffraction order. A peak in the XRD pattern will emerge if the Bragg condition is satisfied. Positions of these peaks can be compared to the International Centre for Diffraction Data (ICDD) Powder Diffraction File (PDF) databases to identify the phase composition of the sample [212].

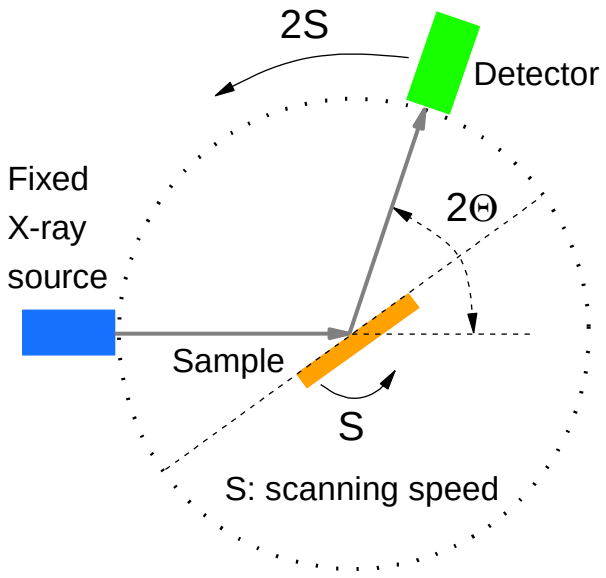

Fig. 3.1. *The general layout for measuring XRD patterns.*

Additionally, the phase purity of synthesised materials was confirmed using Rietveld refinement performed using *Profex* software [213]. Rietveld refinement is the most common powder XRD refinement technique used at the present day. It employs the non-linear least squares method to fit a calculated profile, including all structural and instrumental parameters, to measured XRD pattern [214].

The crystal structures were modelled with *VESTA* – a three-dimensional visualisation system for crystallographic studies and electronic state calculations [215].

3.3. Analysis of the optical properties

3.3.1. PL and PLE spectra and PL decay kinetics

Two separate systems were used to measure the PL and PL excitation (PLE) spectra. To measure PL spectra in NIR and VIS spectral regions, the measuring system shown in **Fig. 3.2.** was used. A Nd: YAG Q-switched laser NT342/3UV (pulse duration – 4 ns) from Ekspla (wavelength tuneable from 210 nm to 2300 nm, the linewidth is 4.3 cm^{-1}) was used as an excitation source. Laser wavelength control accuracy is 0.1 nm. The spectra were recorded with either the Andor DU-490-A CCD camera in the case of NIR PL or the Andor iSTAR DH-734 CCD camera in the case of VIS PL. CCD cameras were coupled to Andor SR-303i-B monochromator/spectrometer with a resolution better than 0.4 nm. For measuring PL decay kinetics, the same system with the photomultiplier tube (PMT) with a time resolution better than 10 ns, together with a digital oscilloscope Tektronix TDS 684A4 as a detection unit, was used.

To obtain PLE spectra, a Photoluminescence Spectrometer FLS1000 from Edinburgh Instruments was used. The excitation source of the system is a 450 W continuous xenon arc lamp. For both – excitation and emission, double Czerny-Turner type monochromators are used. The PMT with spectral coverage from 200 nm to ≈ 870 nm was used for signal detection. The general layout for the system is shown in **Fig. 3.3**.

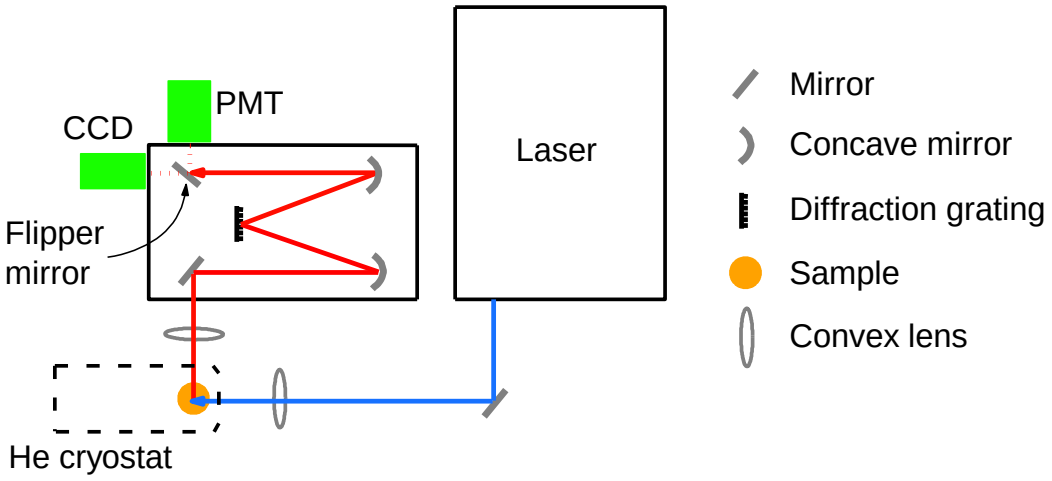

Fig. 3.2. *The general layout of experimental equipment for measuring PL and PersL spectra and PL kinetics.*

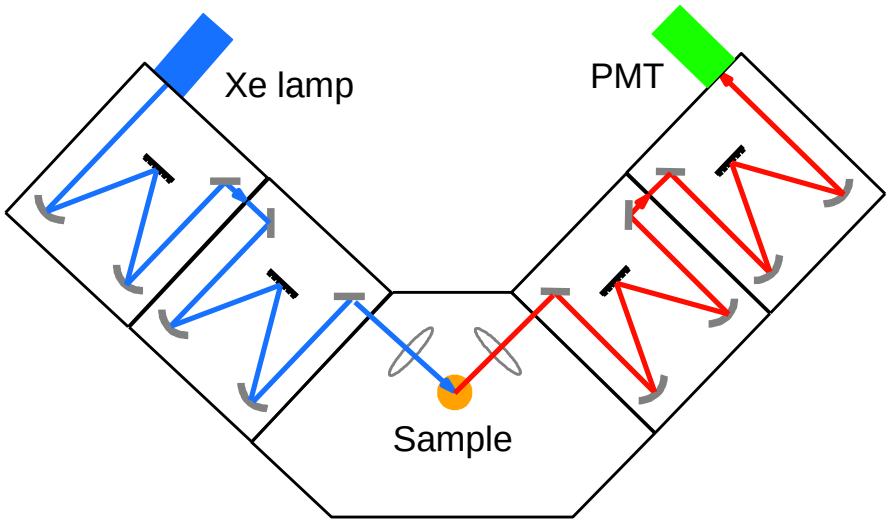

Fig. 3.3. *The general layout of Photoluminescence Spectrometer FLS1000 for measuring PL and PLE spectra.*

3.3.2. PersL spectra and decay kinetics

The PersL spectra were recorded with the same system as the PL spectra shown in ***Fig. 3.2.***

The isothermal PersL decay kinetics were measured using Lexsyg research fully automated TSL/OSL reader from Freiberg Instruments GmbH coupled with PMT Hamamatsu R13456 at 25 °C. As the irradiation source, a Q-switched short-pulsed UV laser DTL-389QT (wavelength 263 nm) from the Laser-compact Group was used.

All luminescence and excitation spectra measurements were corrected for the spectral sensitivity of the equipment.

3.4. Thermally stimulated luminescence

Thermally stimulated luminescence (TSL), also called thermoluminescence, is commonly acknowledged as one of the most efficient techniques for studying trap properties of PersL materials [216]. The fundamental principles of the production of TSL are essentially the same as those of PersL. Namely, some charge carriers are trapped by traps after irradiation but can be released if sufficient energy is accumulated. In the case of RT PersL, charges are slowly freed, and luminescence with decaying intensity is observed. In the case of TSL, the material is typically heated with a constant heating rate, and the luminescence signal may increase and decrease throughout all measuring processes, with increases corresponding to the traps at a specific depth. In the end, a glow curve consisting of one or more glow peaks as $I = f(T)$ will be obtained. Like PersL, the TSL process can be divided into first, second or general-order kinetic processes described in *Subsection 1.3.3.* of this work; however, most practical materials follow first-order kinetics [217].

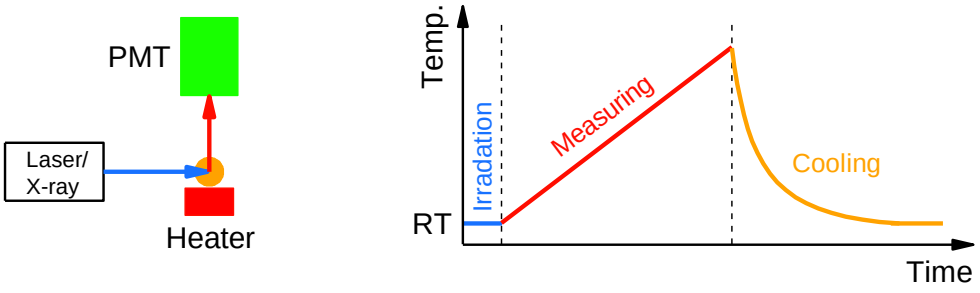

Fig. 3.4. *The general layout for measuring TSL and time-temperature dependence in a typical TSL measurement cycle.*

The TSL measurements were performed using Lexsyg research fully automated TSL/OSL reader from Freiberg Instruments GmbH coupled with photomultiplier Hamamatsu R13456. As the irradiation sources, a Q-switched short-pulsed UV laser DTL-389QT (wavelength 263 nm) from Laser-compact Group or X-ray tube VF-50 J/S, (40 kV, 0.5 mA, W-anode) were used. Used temperature range RT – 300 °C; heating rate, unless stated differently, was 1 °C/s. The general layout for measuring TSL and time-temperature dependence in a typical TSL measurement cycle is shown in **Fig. 3.4**.

A basic TSL glow curve may be used for the primary analysis of the trap properties. Firstly, the number of glow peaks represents the number of distinct traps in the material. Secondly, the position and intensity of each peak correspond to the trap depth and density of trapped charge carriers, respectively. Moreover, the shape of the glow peak depends on kinetic order [216]. A schematic representation of these properties is shown in **Fig. 3.5.**

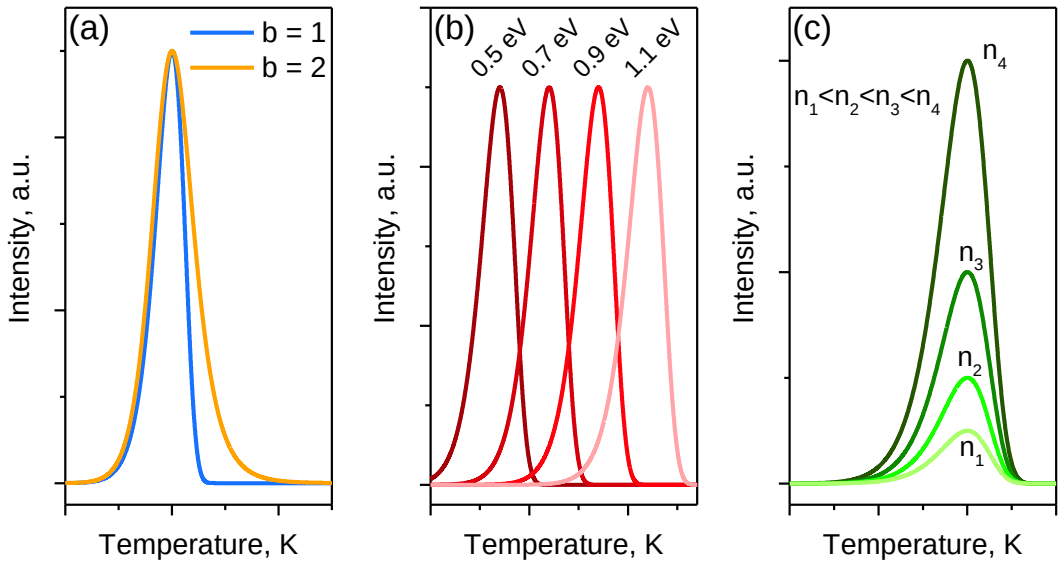

Fig. 3.5. (a)*Typical TSL glow peaks for different kinetic orders,* ***(b)*** *first-order TSL glow peaks for different trap depths and* ***(c)*** *first-order TSL glow peaks for different concentrations of trapped charge carriers after irradiation dose n.*

By applying more advanced measurement techniques, it is possible to evaluate the trap nature: whether there are discrete trapping sites or continuous distribution, as well as trap depth values, frequency factors, etc.

3.4.1. Evaluation of trap nature

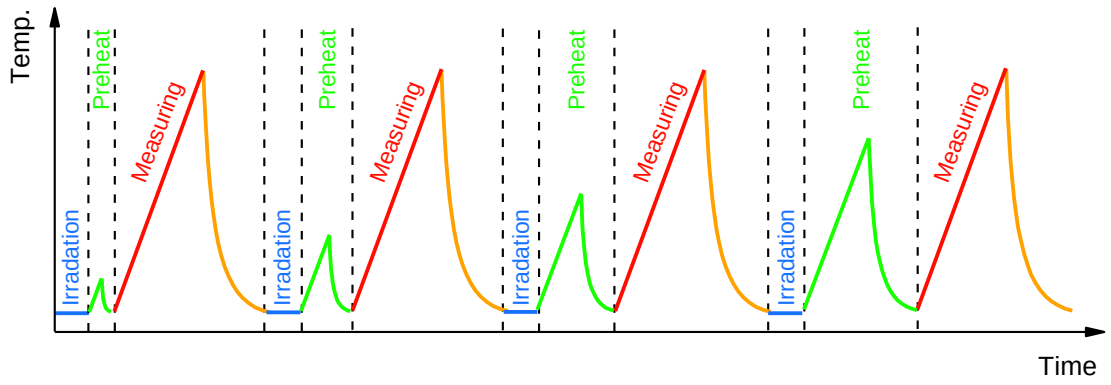

Fig. 3.6. *Basic scheme of the T_{max}-T_{stop} experiment measurement cycle.*

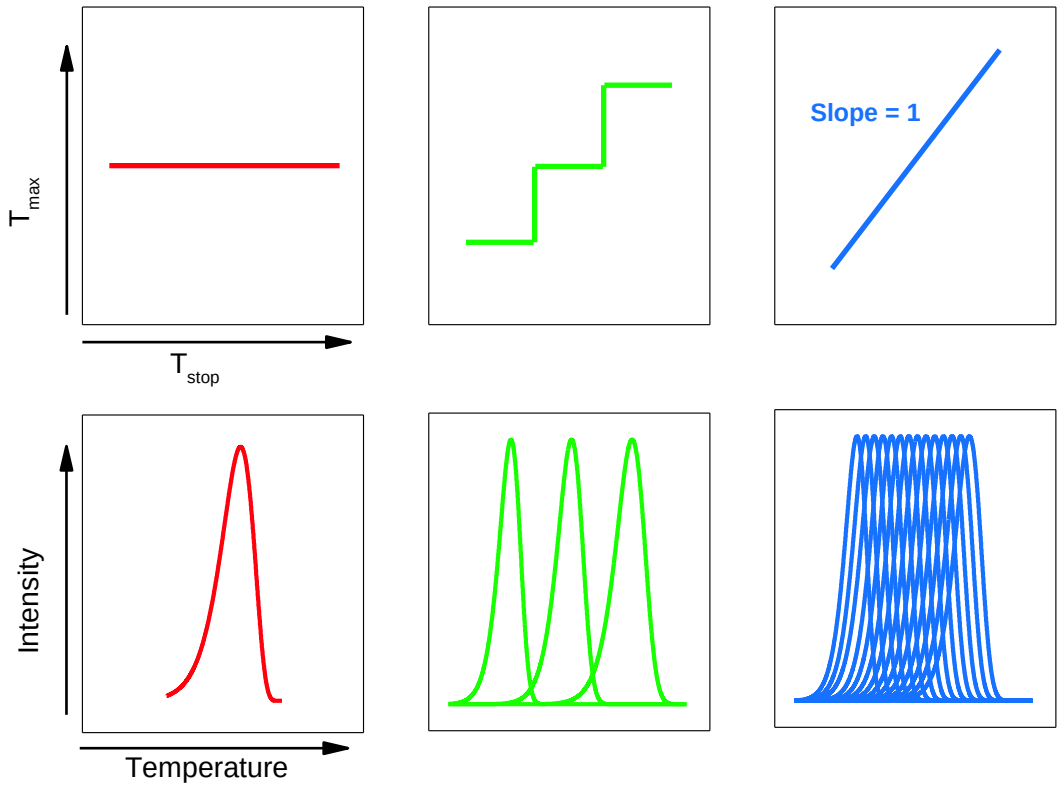

Fig. 3.7. *Schematic T_{max}-T_{stop} plots for first-order glow peaks. A single glow peak and corresponding straight line of slope = 0; three well separated glow peaks with a characteristic "staircase" structure and closely overlapping continuous distribution of glow peaks and a characteristic line with slope = 1.*

Developed by McKeever in 1980, T_{max} – T_{stop}, sometimes called partial thermal cleaning analysis, is a widely used experimental method for determining the number of glow

peaks and their maximum temperature, which typically correlates with trap depth. Additionally, this method gives information about the nature of traps [218]. The basis of T_{max} – T_{stop} is preheating of previously irradiated sample to chosen temperature $T_{stop,}$ thereby thermally cleaning the glow curve up to that temperature. Following, the sample is rapidly cooled down to RT, and a TSL glow curve, as usual, is measured. The entire process, including irradiation, is repeated multiple times; T_{stop} is increased by a few degrees each time. The basic scheme of the T_{max}-T_{stop} experiment measurement cycle is shown in **Fig 3.6.** For each residual glow curve, the temperature corresponding to the first local maximum T_{max} is determined, and a plot of the T_{max} versus T_{stop} is made. If there is a single trapping site in the material, a straight line with a slope of 0 is expected. If the number of trapping sites is more than one, but they can be viewed as discrete traps, a "staircase" structure with each plateau region indicating the presence of an individual peak will appear. Finally, if the number of traps is high and they can be considered rather distributed than discrete, a straight line with a slope close to 1 is expected [219,220]. **Fig. 3.7.** represents these three possibilities.

3.4.1.1. Evaluation of trap depth distribution

Continuous trap distributions may vary by their shape. For example – uniform, exponential, and Gaussian profiles have been considered. The method developed by Van den Eeckhout *et al*. [11] can be used to estimate trap depth density distribution. The premise of this method is a calculation of the difference between the integrated intensity of two consecutive TSL glow curves from the T_{max} – T_{stop} experiment. Since integrated intensity is directly related to the total number of filled traps after the sample has been heated to the T_{stop}, the difference between the integrated intensities is a measure of the change in the number of filled traps between the measurements. From this, the density of traps at different preheating temperatures can be acquired.

3.4.2. Evaluation of trap depth values

Trap depth value or activation energy E_a is arguably the most critical parameter for PersL phosphor; thus, many methods for E_a evaluation have been developed throughout the years. The simplest approximation states that $E_a = \frac{T_{max}(K)}{500}$ [221]; at the same time, glow curve deconvolution methods use complicated equations and fitting software [222]. In this work, two methods of evaluation of trap depth are used: various heating rate method and initial rise analysis (IRA).

3.4.2.1. Various heating rate method

One of the most widely accepted TSL analyses for trap depth estimation in the case of first-order kinetics is Hoogenstraaten's or various heating rate method [223], which evaluates the shift of the glow peak position depending on the heating rate. **Fig. 3.8.** shows a basic scheme of the various heating rate experiment. From each obtained glow curve T_{max}

– the temperature at the maximum intensity point is noted. Using different heating rates β and *Eq. (3.2)*, one can obtain both trap depth E_a and frequency factor s.

$$\frac{\beta E_a}{k_B T_{max}^2} = s \cdot exp\left(\frac{E_a}{k_B T_{max}}\right). \tag{3.2}$$

Here k_B is the Boltzmann constant. The plot of $\left(\frac{1}{k_B T_{max}}\right)$ versus $ln\left(\frac{T_{max}^2}{\beta}\right)$ should give a straight line with slope E_a and intercept $ln\left(-\frac{E_a}{sk_B}\right)$, which can be used to calculate the s value.

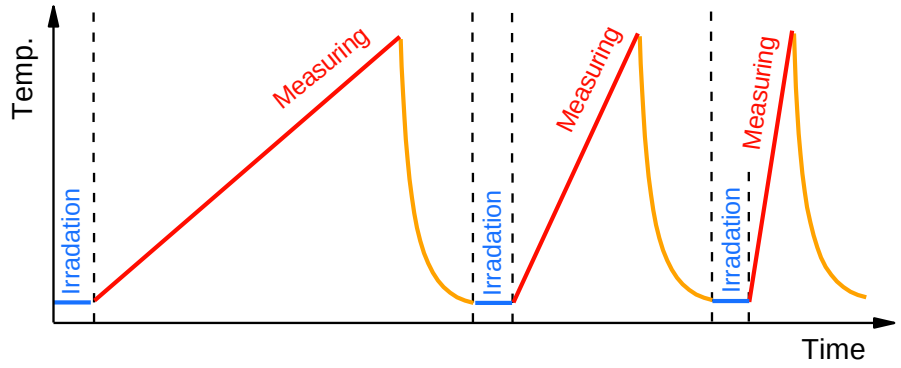

Fig. 3.8. *Basic scheme of the various heating rate experiment.*

3.4.2.2. Initial rise analysis

IRA is a widely used experimental technique for determining trap depth from the TSL glow peak of any kinetic order. This method is based on analysing the initial low-temperature side of the TSL peak. It is assumed that the initial rise of the glow peak will follow the Arrhenius equation [224]:

$$I(T) = \mathrm{C} \cdot \exp\left(-\frac{E_a}{k_B T}\right), \tag{3.3}$$

where $I(T)$ – intensity as a function of temperature, C – a constant that includes a frequency factor (assumed to be independent of temperature) and T is a temperature. According to *Eq. (3.3)*, if $ln(I)$ is plotted as a function of $\frac{1}{k_B T}$, a straight line with a slope -E_a is obtained to represent the initial rise part of the glow peak. When applying IRA, only the initial part of the glow peak can be used, not higher than 15% of maximum intensity [225].

The popularity of the IRA may be explained through two significant advantages of this method. Firstly, it does not depend on the order of kinetics, and secondly, since only the low-temperature side of the glow peak is used, the problems related to the overlapping of the nearby glow peaks are diminished [24].

3.5. Electron paramagnetic resonance

Electron paramagnetic resonance (EPR) spectroscopy, sometimes called electron spin resonance (ESR) spectroscopy, is a method for studying materials with unpaired electrons by recording the resonance of an atomic particle as a result of microwave absorption in the presence of an external magnetic field [22].

EPR spectroscopy is based on the quantum physics notions of magnetic moment and spin of an electron. Every electron has a magnetic moment and spin quantum number s = ½ with magnetic components m_s = ½ and m_s = -½. When an external magnetic field is applied, spin aligns either to or opposite the direction of the magnetic field, and the splitting of the electron spin sublevels occurs (**Fig. 3.9. (a)**). This effect is referred to as the electron Zeeman splitting [226].

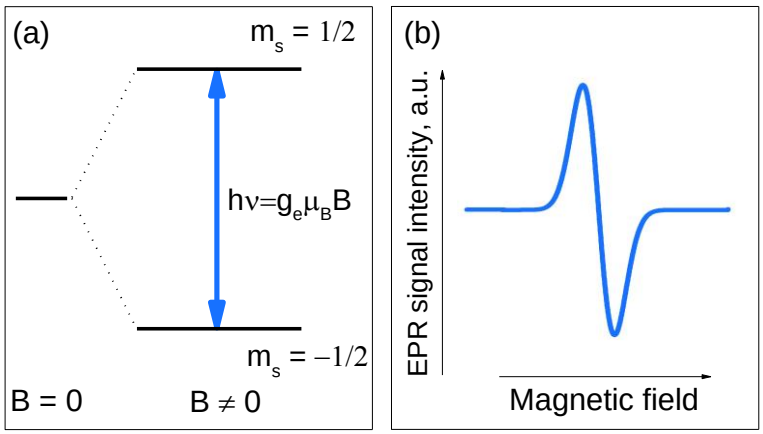

Fig. 3.9. (a) *Diagram of the splitting of electron spin states under B ≠ 0 and* ***(b)*** *typical EPR signal for the corresponding transition.*

Energy difference $h\upsilon$ between splitted levels can be expressed by the following equation:

$$h\nu = g\mu_B B \tag{3.4}$$

where h – Planck's constant, ν – frequency of absorbed electromagnetic radiation, μ_B is a constant – the Bohr magneton, B – the strength of the applied magnetic field and g is the spectroscopic splitting factor, also called g-factor. g-factor for free electron g_e is 2.0023 but varies significantly for paramagnetic ions in the solid state materials. *Eq. (3.4)* is called the electron paramagnetic resonance condition, and it can be satisfied by changing ν or B. In practice, EPR spectra are obtained by varying B at a constant frequency; typically, ≈ 9 or ≈ 35 GHz microwave (MW) bands are used. To improve the sensitivity, a small additional oscillating magnetic field at a typical frequency of 100 kHz is added, resulting in a signal that is the first derivative of MW absorption. A basic EPR signal is illustrated in **Fig. 3.9. (b)**.

In real crystal systems, in addition to interaction with the external magnetic field, other interactions may play a role in EPR spectra as well:

- ► electron-electron interaction in systems with multiple unpaired electrons appears in spectra as a “fine” structure;
- ► nucleus-electron interaction appears in spectra as a “hyperfine” structure;
- ► other interactions, such as the nuclear Zeeman interaction of the nuclear spins with the external magnetic field [227].

For the calculations and simulations, these interactions are typically described using the spin Hamiltonian (SH) formalism [228].

$$\breve{H} = \breve{H}_{EZ} + \breve{H}_{ZFS} + \breve{H}_{HFS} + \ldots \tag{3.5}$$

$$\breve{H}_{EZ} = g\mu_{\beta}BS \tag{3.6}$$

$$\breve{H}_{ZFS} = S\boldsymbol{D}S \tag{3.7}$$

$$\breve{H}_{HFS} = I\boldsymbol{A}S \tag{3.8}$$

Here $\breve{H}_{EZ}$ – Hamilton operator for the electron Zeeman interaction, $\breve{H}_{ZFS}$ – Hamilton operator for electron-electron interaction (zero-field splitting), and $\breve{H}_{HFS}$ – Hamilton operator for nucleus-electron interaction. S – electron spin operator; $\boldsymbol{D}$ – the zero-field splitting tensor, which can be expressed as $D = 3D_z/2$ and $E = \left(D_x - D_y\right)/2$ where D and E are SH parameters; $\boldsymbol{A}$ – the hyperfine coupling tensor; I – nuclear spin operator [229–231].

In this work, RT EPR spectra were measured with a Bruker ELEXSYS-II E500 CW-EPR spectrometer operated in the X (9.836 GHz) and Q (33.91 GHz) microwave frequency bands. The spectra acquisition parameters were: 10 mW microwave power and 0.2 mT magnetic field modulation amplitude. Stepwise sample annealing was performed in a custom-built furnace in the air with an estimated temperature uncertainty of ± 10 °C. For irradiation, an X-ray tube Spellman (40 kV, 20 mA, W anode) or a pulsed solid-state laser NT342/3UV from Ekspla was used. For EPR spectra simulations, the *EasySpin* software [232] was used. The general layout for EPR spectra measuring equipment is shown in **Fig. 3.10.**

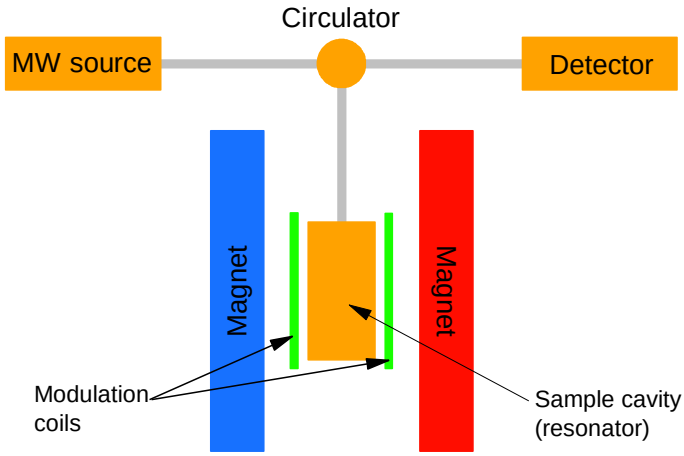

Fig. 3.10. *The general layout for EPR spectra measuring equipment.*

4. RESULTS AND DISCUSSION

4.1. Impact of synthesis atmosphere on $MgGeO_3$: Mn^{2+}

4.1.1. Short introduction

As discussed in the *Literature review*, $MgGeO_3$: Mn^{2+} as a compelling red PersL phosphor was first reported almost 20 years ago [123]. Since then, with varying results, several efforts have been made to enhance its PersL properties by co-doping [145,179,180,233].

Here the impact of the synthesis atmosphere on the luminescence properties of $MgGeO_3$: Mn^{2+} material will be discussed in detail, together with a comprehensive analysis of TSL and EPR data and a consequential discussion about trap properties.

Based on previous reports, a doping concentration of 0.1 mol% Mn^{2+} was chosen; thus, $MgGeO_3$: 0.1 mol% Mn^{2+} samples were synthesised in either an ambient or a reducing atmosphere. Obtained samples are denominated as aMGO and rMGO for ambient and reducing atmosphere synthesised materials, respectively.

4.1.2. Structure analysis

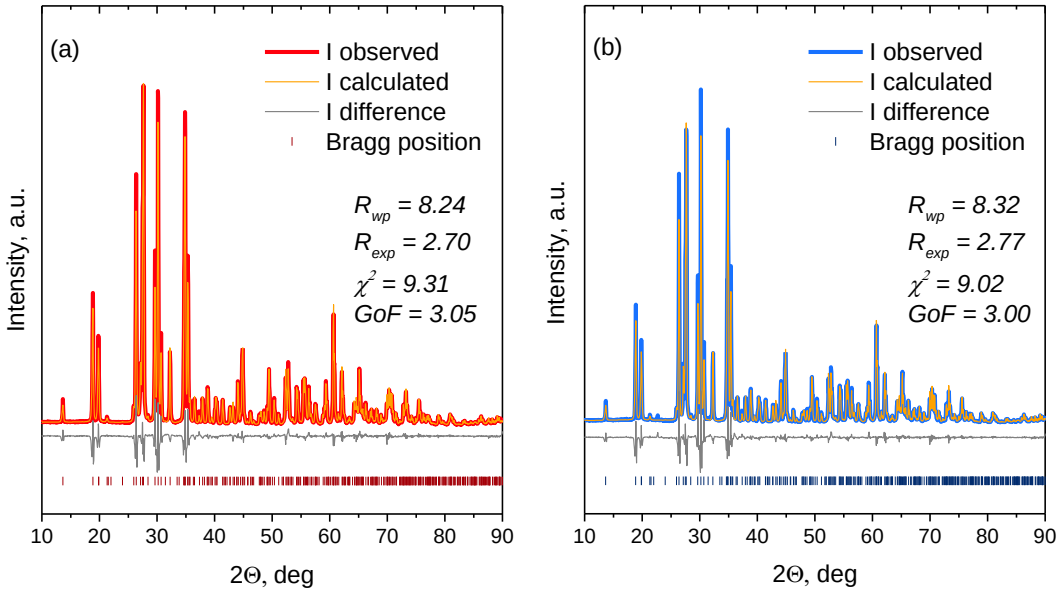

Fig. 4.1. *Rietveld refinement of* ***(a)*** *aMGO and* ***(b)*** *rMGO XRD data.*

The observed and calculated XRD patterns of aMGO and rMGO samples, along with the difference profile and the Bragg reflection positions for Rietveld refinement, are presented in **Fig. 4.1**. The values of the refinement factors R_{wp}, R_{exp}, χ^2 and GoF indicate that the refined results are reliable. Both samples can be characterised with a single-phase orthorhombic $MgGeO_3$ structure, corresponding to the PDF 00-034–0281. This suggests that manganese ions are well incorporated in the $MgGeO_3$ lattice. Based on the ionic radii of Ge^{4+}

(r = 0.39 Å, four-fold coordination), Mg^{2+} (r = 0.72 Å, six-fold coordination), Mn^{2+} (r = 0.67 Å, six-fold coordination), Mn^{2+} most likely occupies the Mg^{2+} sites [145,179]. No significant differences in the diffraction peaks were observed for the samples synthesised in various atmospheres.

4.1.3. Analysis of luminescence properties

Fig. 4.2. (a) shows PLE (λ_{em} = 680 nm) and PL (λ_{ex} = 263 nm) spectra for the samples synthesised in the air or reducing atmosphere. Due to the relatively weak intensity of Mn^{2+} intra-atomic transition related excitation bands, the 340 – 450 nm spectral region of PLE is magnified. All the observed excitation bands were assigned as follows: the excitation band around 215 nm, in good accordance with multiple previous studies [145,234], is the band-to-band transition of the host material. For overlapping bands between 225 nm and 325 nm, the most likely origins are CT transition from O^{2-} to Mn^{2+} (225 – 250 nm) [235] and photo-oxidation of Mn^{2+} and subsequent CT to CB: $Mn^{2+} \rightarrow Mn^{3+} + e^-$ (250 – 325 nm) [123,236], some contribution of host absorption related to intrinsic defects is expected as well [233]. From Mn^{2+} d-d transitions, only two bands were distinguishable 417 nm band corresponding to $^6A_1(^6S) \rightarrow {}^4A_1/{}^4E(^4G)$ transition and 370 nm band corresponding to $^6A_1(^6S) \rightarrow {}^4T_2(^4D)$ transition.

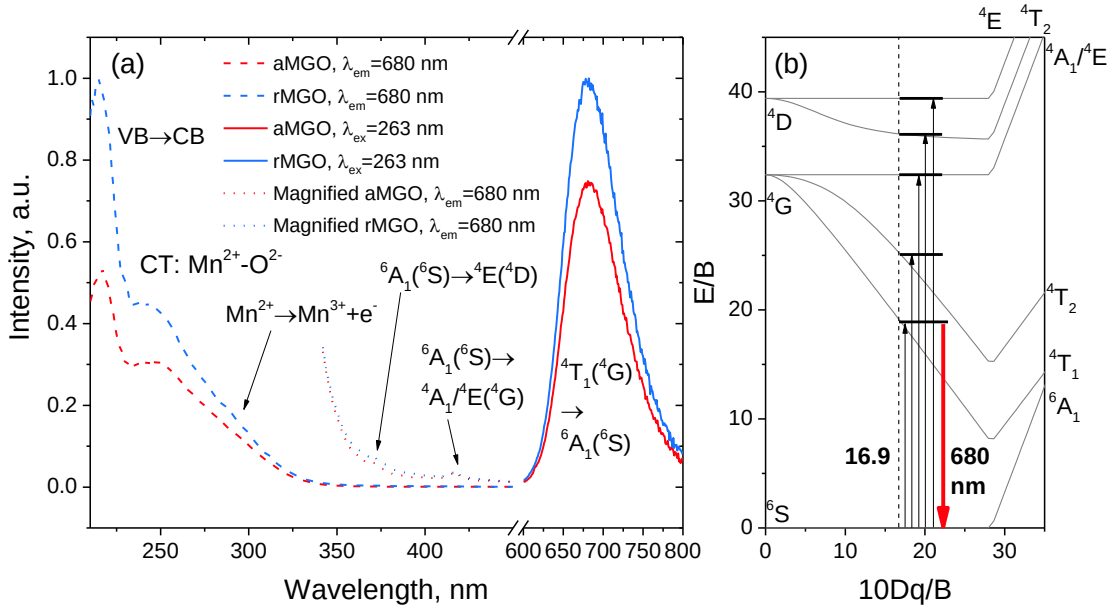

Fig. 4.2. (a) *The PLE (λ_{em} = 680 nm) spectra with magnified 340 – 450 nm part and PL (λ_{ex} = 263 nm) spectra of aMGO and rMGO samples and* ***(b)*** *simplified Tanabe-Sugano diagram of Mn^{2+} ions with roughly calculated energy level positions of Mn^{2+} in $MgGeO_3$.*

For both samples, an intense red/NIR PL band between 600 – 800 nm with a maximum at 680 nm was observed when excited with 263 nm. This band corresponds to the Mn^{2+} optical transition from the excited state $^4T_1(^4G)$ to the ground state $^6A_1(^6S)$ [237]. **Fig. 4.2. (b)** represents a simplified Tanabe-Sugano diagram for Mn^{2+} in the $MgGeO_3$ matrix with the crystal field parameters approximated following *Eq. (1.19)*. Note that for this calculation,

energy values for $^6A_1(^6S) \rightarrow {}^4A_1/{}^4E(^4G)$ and $^6A_1(^6S) \rightarrow {}^4E(^4D)$ transitions are necessary. The $^6A_1(^6S) \rightarrow {}^4E(^4D)$ transition in PLE spectra strongly overlaps with CTBs; thus, a precise energy value cannot be obtained. However, since the corresponding energy level position is somewhat insensitive to the crystal field surrounding the Mn^{2+} ion, the necessary value (≈ 350 nm, 28570 cm^{-1}) was approximated from several other sources [73,140,151,238–241]. Thus 10Dq/B value was estimated to be around 16.9.

It was observed that the synthesis in the reducing atmosphere enhances the intensity of PL. Furthermore, PL decay profiles of the red luminescence of aMGO and rMGO samples excited at 263 nm were measured. Both decay curves can be fitted using the sum of two exponential decay equations *Eq. (1.3)*. As shown in **Fig. 4.3**., both τ_1 and τ_2 values are slightly larger for the rMGO sample. Based on these parameters, the average lifetime τ_{avg} can be calculated by the following equation:

$$\tau_{avg} = \frac{C_1\tau_1^2 + C_2\tau_2^2}{C_1\tau_1 + C_2\tau_2} \tag{4.1}$$

From *Eq. (4.1),* the average lifetime of the PL of the aMGO sample is 13.3 ms, while the average lifetime of the PL of the rMGO sample is 15.6 ms. This increase is likely caused by oxygen vacancy related energy transfer from the host to Mn^{2+}. This effect has been previously observed in similar materials [242,243].

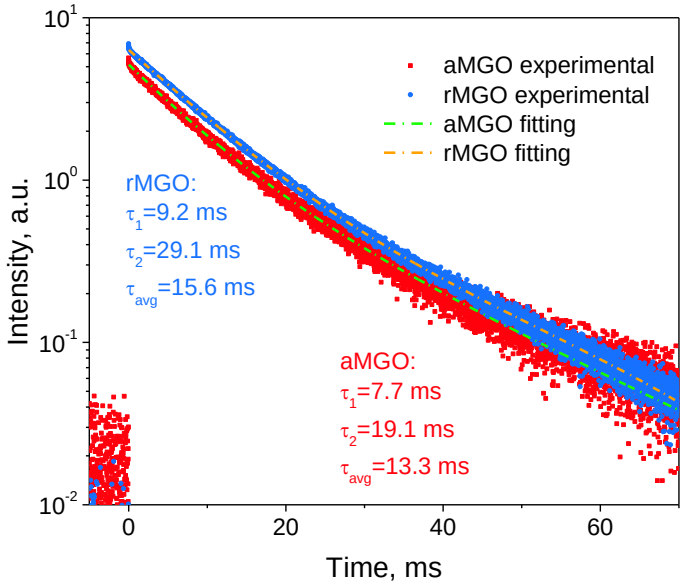

Fig. 4.3. *PL decay profiles monitoring the emission of 680 nm (λ_{ex} = 263 nm), fitted curves and corresponding decay time values τ_1 and τ_2 for the exponential components for aMGO and rMGO samples.*

The excitation with UV leads to the creation of PersL in both samples. After irradiation with 263 nm for 10 min, PersL can be observed for more than 10 hours. Throughout all decay process, the shape of the PersL emission spectra stays identical to the PL, indicating that the PersL emission originates from the same $^4T_1(^4G) \rightarrow {}^6A_1(^6S)$ transition of Mn^{2+} ions as PL. The PersL decay curves, drawn in the double-logarithmic scale, are shown in

Fig. 4.4. Inset shows PersL spectra of the aMGO sample at different times during the decay. For the first 3 hours, the rMGO sample has higher PersL intensity than the aMGO sample; after that, there is no significant difference.

As discussed in the *Theoretical background*, the PersL decay of most materials follows the power law (*Eq. (1.12)*). This type of curve in a double-logarithmic plot appears as a straight line. In the case of PersL of aMGO and rMGO, it is impossible to fit the decay profiles with a single line; however, multiple linear parts with different slopes can be observed in each curve. It is reasonable to expect complex decaying behaviour if various traps with distinct trap depths are involved in the production of PersL. Therefore, the decay profiles of the PersL in aMGO and rMGO samples indicate the presence of multiple types of traps.

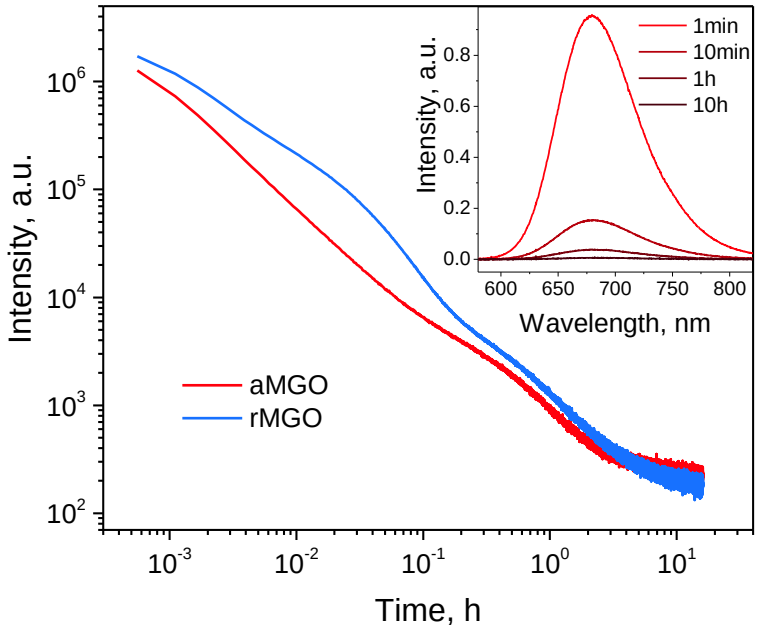

Fig. 4.4. *The afterglow decay curves of the aMGO and rMGO samples after irradiation for 10 min with 263 nm; inset: PersL spectra of aMGO sample at different time periods after irradiation has stopped.*

4.1.4. Analysis of trap properties

To analyse the properties of the traps present in aMGO and rMGO samples, TSL measurements were carried out by increasing temperature from RT up to 300 °C at a rate of 1 °C/s. The obtained glow curves are shown in **Fig. 4.5.** Glow curves of both samples cover most of the measured temperature region and consist of five peaks, with the dominant glow peak around 125 °C. There are some differences in the glow curves depending on the synthesis atmosphere. Although glow peaks appear at the same temperature regions in both cases, the synthesis in a reducing atmosphere promotes the relative intensity of glow peaks at lower temperatures strongly suggesting an increased relative density of shallow traps. This coincides with PersL decay profiles since RT PersL will mostly be affected by shallow traps. Interestingly, the most prominent glow peak at 125 °C has a higher intensity in the

case of the aMGO sample; however, this does not yield a big difference in PersL at RT for at least the first few hours.

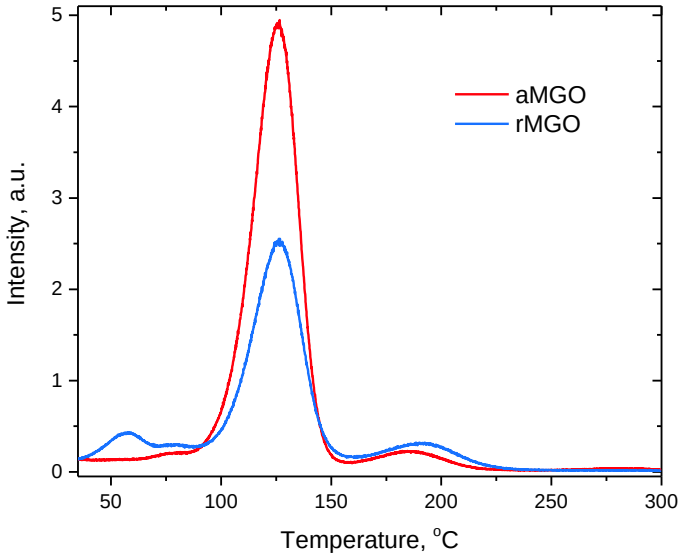

Fig. 4.5. *TSL glow curves of aMGO and rMGO samples irradiated with 263 nm for 30s; heating rate 1 °C/s.*

To determine a precise number of glow peaks, their maximum temperature and obtain information about the nature of traps (whether there are discrete trapping states or closely overlapping trapping states forming a continuous distribution), the $T_{max} - T_{stop}$ experimental method was applied. The obtained glow curves and corresponding $T_{max} - T_{stop}$ plots are shown in **Fig. 4.6. (a,b)** for aMGO and **Fig. 4.6. (c,d)** for rMGO. Results show that in the case of aMGO, there are five discrete traps in the temperature range from RT to 300 °C. There are no substantial shifts in T_{max} values which are approximately 53; 72; 122; 182; 276 °C, with changing T_{stop}. Therefore, it is expected that trap depths stay the same as well. If the sample is synthesised in a reducing atmosphere, the first four traps have slightly higher T_{max} values; however, they are still discrete by nature, and each can be characterised with a single trap depth value. A notable distinction between $T_{max} - T_{stop}$ plots of aMGO and rMGO samples appear in the high-temperature range where T_{stop} > 200 °C. The "staircase" shaped pattern in rMGO disappears, and the plot can be fitted with a straight line with the slope m = 0.99 ± 0.08. This result indicates that synthesis in a reducing atmosphere causes the emergence of a group of closely overlapping glow peaks related to continuous trap distribution [244–246]. The difference in the behaviour of the high-temperature glow peak of aMGO and rMGO samples during $T_{max} - T_{stop}$ experiment is well observable in the insets of **Fig. 4.6. (a,c).** While in the case of the aMGO sample, the glow peak at 275 °C stays at the same position, regardless of T_{stop}, the maximum of the corresponding glow peak of rMGO continuously moves to higher temperatures when T_{stop} is increased. This effect is indicated with green and orange arrows.

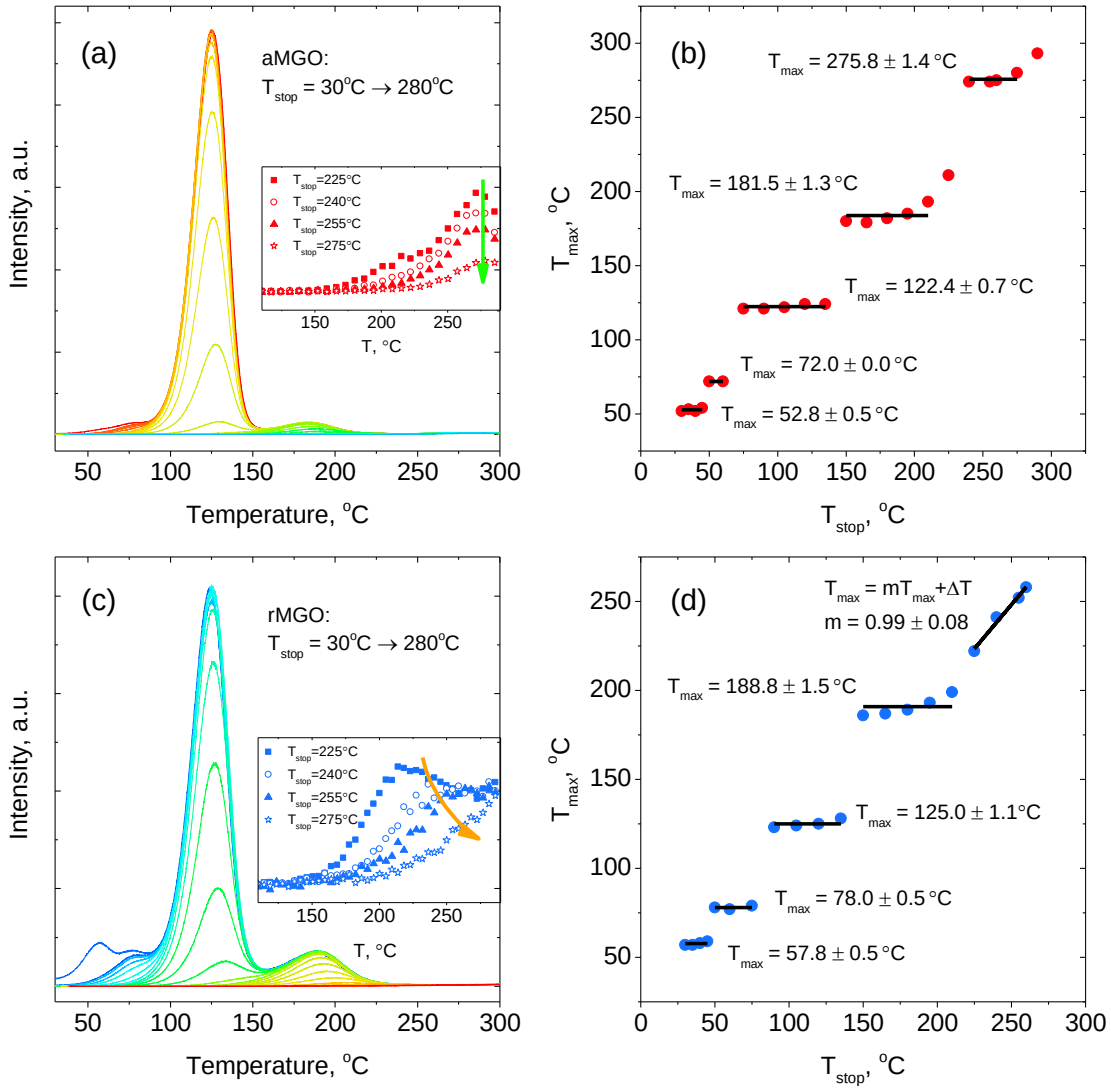

Fig. 4.6. *The glow curves of aMGO* ***(a)*** *and rMGO* ***(c)*** *samples measured after preheating temperatures T_{stop}. Insets show magnified end parts of glow curves with varying preheating temperatures. Green, in the case of aMGO, and orange, in the case of rMGO, arrows indicate the shift of T_{max} according to the change of T_{stop}.* ***(b)*** *and* ***(d)*** *represents the T_{max} – T_{stop} plots for aMGO and rMGO samples, respectively.*

The next step for the PersL material characterisation is determining the trap depth. Since it was shown in Ref. [247] that there are no significant differences in PL, PersL spectra and the glow peak positions between X-ray and UV irradiated samples, for convenience, further analysis was made for X-ray irradiated samples. To determine appropriate method for trap depth estimation, the kinetic order of the TSL mechanism must be known. As a rule, if the position and shape of the glow peak do not change depending on radiation dose, the TSL mechanism follows first-order kinetics [216]. Both aMGO and rMGO samples abide by this condition. A representative example of dose-response TSL measurements by varying the irradiation time for an X-ray irradiated aMGO sample is shown in **Fig. 4.7.**

First-order kinetics theory assumes that charge carrier retrapping during the heating of the material is negligible compared to recombination. Nevertheless, it is worth mentioning that this idea has been challenged by several sources [217,248]; therefore, no far-reaching conclusions about the physical mechanisms should be made.

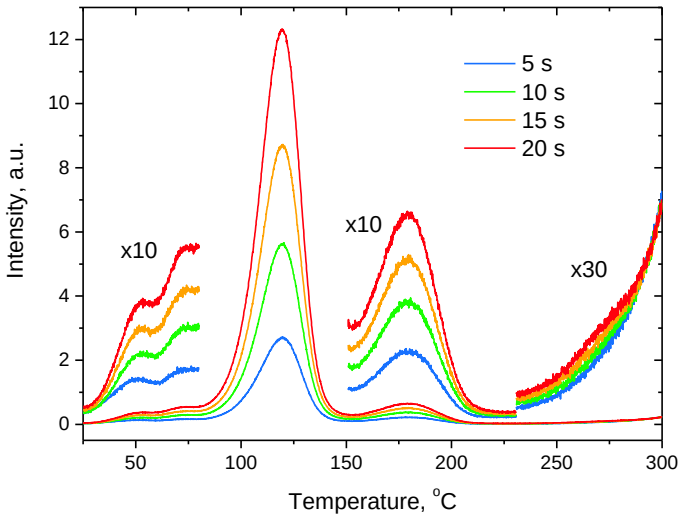

Fig. 4.7. *The dose-response TSL glow curves of the aMGO sample obtained after irradiation with X-rays for different periods of time. The less pronounced glow peaks are multiplied by 10 or 30.*

In the case of first-order kinetics, the varying heating rate or Hoogenstraaten's method to evaluate E_a can be employed. **Fig. 4.8. (a)** shows glow curves of the aMGO sample heated at different rates β = 0.25, 0.50, 1.00, 2.00, 4.00 °C/s after irradiation with X-rays. The exact measurements were done for the rMGO sample as well. Using different heating rates and *Eq. (3.2)*, trap depths and frequency factors corresponding to each peak were obtained. **Fig. 4.8. (b)** shows sets of 5 points relevant to the specific glow peaks for both samples and respective linear fits.

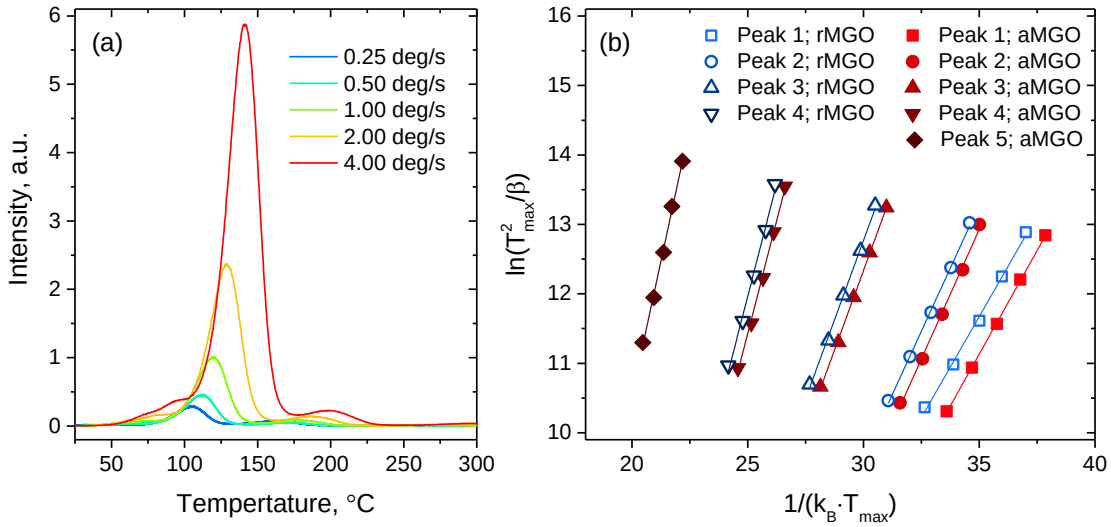

Fig. 4.8. (a) *Glow curves of aMGO sample heated at different rates after irradiation with X-rays and* ***(b)*** *heating rate plots of rMGO and aMGO samples. The glow peaks have been labelled as Peak 1 to Peak 5 from the lowest to the highest corresponding T_{max}.*

Obtained trap depth E_a and frequency factor s values are summarised in *Table 4.1.* The glow peaks have been labelled Peak 1 to Peak 5 from the lowest to the highest

corresponding T_{max}. Additionally, the theoretical mean lifetimes τ at T = 20 °C of the glow peaks were calculated using *Eq. (1.4)*.

Due to low signal intensity and interfering black-body radiation, reliable trap depth values of continuously distributed traps in the high-temperature range of the rMGO glow curves could not be determined. However, these values are expected to be around the activation energy estimated for the Peak 5 of aMGO.

Results show that the trap depth values for specific glow peaks within the margin of errors do not change depending on the synthesis atmosphere; however, the frequency factor and, consequently, mean lifetime vary between the two samples. This is likely a result of different rates of additional detrapping mechanisms such as tunnelling, etc.

Effective thermal promotion of electrons from traps to CB leading to exceptional PersL performance at RT can be expected in the materials where the trap depths extend up to 0.8 eV [5,23]. In the case of aMGO and rMGO, the first two traps fit into this range, and the activation energy of the most populated trap is 0.91 eV, which is quite close, leading to the long PersL observed in both samples. The most significant difference in trap properties between in air and in reducing atmosphere synthesised samples can be observed in the deep traps, which most likely give no contribution to RT PersL.

Table 4.1. Estimated trap depths E_a, eV and frequency factors s, s^{-1} derived from the heating rate plot and τ (20 °C) - mean lifetime at 20 °C of the corresponding TSL peak.

aMGO

Peak	**E_a, eV**	**s, s^{-1}**	**τ (20 °C)**
#1	0.60 ± 0.01	$(1.21 \pm 0.02) \cdot 10^8$	≈ 3 min
#2	0.75 ± 0.02	$(3.63 \pm 0.21) \cdot 10^9$	≈ 40 min
#3	0.91 ± 0.01	$(2.44 \pm 0.05) \cdot 10^{10}$	≈ 2.3 days
#4	1.30 ± 0.04	$(1.03 \pm 0.05) \cdot 10^{13}$	≈ 80 years
#5	1.55 ± 0.04	$(4.83 \pm 0.22) \cdot 10^{12}$	$\approx 3.4 \cdot 10^6$ years

rMGO

Peak	**E_a, eV**	**s, s^{-1}**	**τ (20 °C)**
#1	0.58 ± 0.02	$(3.93 \pm 0.29) \cdot 10^8$	≈ 4 min
#2	0.73 ± 0.01	$(1.28 \pm 0.05) \cdot 10^9$	≈ 50 min
#3	0.91 ± 0.02	$(1.46 \pm 0.07) \cdot 10^{10}$	≈ 3.8 days
#4	1.30 ± 0.06	$(5.04 \pm 0.36) \cdot 10^{12}$	≈ 160 years

Additionally, EPR investigations before and after irradiation with X-rays were performed. The representative results for the rMGO sample are shown in **Fig. 4.9. (a)**. The spectra were measured using 0.2 mT field modulation amplitude to avoid broadening spectral features; the 9.83 GHz microwave frequency was used.

After irradiation, a change in the Mn^{2+} spectrum shape at 351 mT (g = 1.998) appears. A subtraction of spectra for the samples after and before irradiation reveals an additional Gaussian-shaped component with a peak-to-peak linewidth of 0.7 mT. This additional signal was measured for 8 h after irradiation. To evaluate the change of signal in time, the double integral (DI) value is used. The results are shown in the inset of **Fig. 4.9. (a).**

A free-electron *g* value is 2.0023, and shifting to a smaller value may indicate that the signal belongs to an F-type centre [249]. Similar *g* values have been previously reported in different oxide hosts [250]. Here the EPR signal is linked to an F^+ centre – one electron trapped in an oxygen vacancy: $V_O^{\bullet\bullet} + e^- \rightarrow V_O^{\bullet}$. The decay time of the observed EPR signal correlates with the decay time of the PersL of the samples. A detailed analysis of the absolute value of the EPR signal decay in comparison with the decay curve of PersL for the rMGO sample is given in **Fig. 4.9. (b)**; both signals are normalised at t = 3 min. In a double-logarithmic plot, data points of both curves significantly overlap, which strongly indicates that the *g* = 1.998 EPR signal and decay of PersL are interconnected. The additional EPR signal is not stable at RT; nevertheless, it could be completely bleached out of the EPR spectrum only after heat treatment at 200 °C. Therefore, the experimental results indicate a relationship between the observed paramagnetic centre and thermally stimulated processes in samples from RT to 200 °C, a temperature range corresponding to the first four glow peaks in the TSL glow curve.

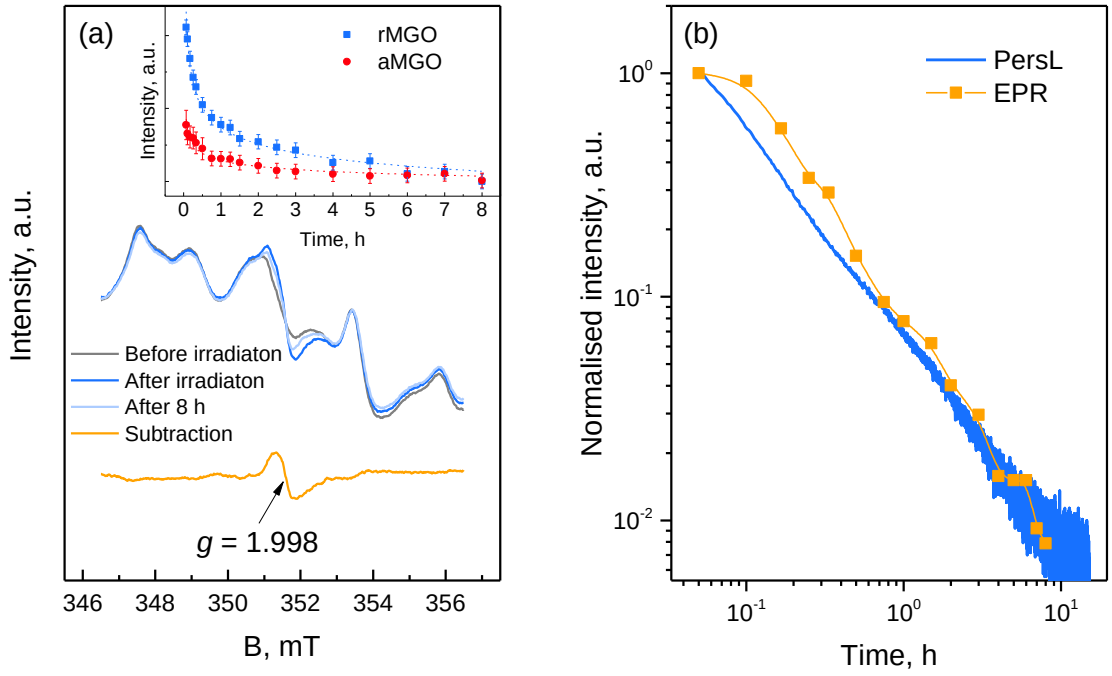

Fig. 4.9. (a) *EPR spectra of rMGO sample before and after X-ray irradiation. Inset: the decay of double integral value of EPR signal intensity for rMGO and aMGO samples and* ***(b)*** *a comparison of g = 1.998 EPR signal decay and PersL decay curve after rMGO irradiation with X-rays.*

4.1.5. Mechanism of the luminescence processes

Based on the obtained results, possible mechanisms of the PL and PersL in $MgGeO_3$: Mn^{2+} phosphor are illustrated in **Fig. 4.10.** Note that the locations of the energy levels and traps are shown schematically and not to scale. Irradiation at 263 nm predominantly excites Mn^{2+}-O^{2-} CTB bringing electrons from VB to CTB near CB and leaving holes in VB. Due to photoionisation, some of the electrons from CTB can be delocalised to the CB. Delocalised electrons move through CB and get captured by traps that partially consist of oxygen

vacancies. At the same time, holes are captured by unidentified hole traps. After ceasing the excitation, charge carriers may be thermally liberated and transferred via the host to Mn^{2+}, where recombination occurs, and red PersL emission emerges.

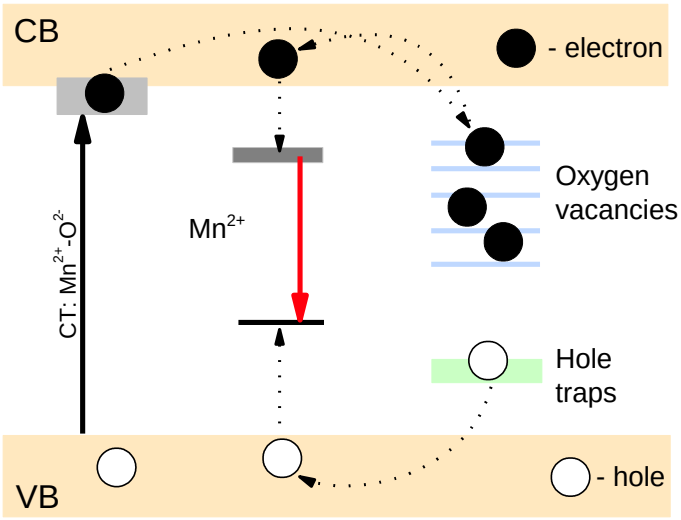

Fig. 4.10. *The schematic diagram of the luminescence processes in $MgGeO_3:Mn^{2+}$ material.*

4.1.6. Summary

In conclusion, $MgGeO_3$ material doped with 0.1 mol% Mn^{2+} was successfully synthesised by the solid state reaction at 1250 °C in the air or reducing atmosphere.

Regardless of the synthesis atmosphere, a broad red Mn^{2+} ($^4T_1(^4G) \rightarrow {}^6A_1(^6S)$) PL and PersL band with the maximum wavelength at 680 nm was observed. Synthesis in a reducing atmosphere slightly increases the luminescence intensity of $MgGeO_3$: Mn^{2+} material. After irradiation with 263 nm, PersL was observed to last for at least 10 h for both samples. However, for the first few hours, the intensity of the PersL of the sample synthesised in a reducing atmosphere is higher than that of the sample synthesised in air. The observed PersL is a complex process involving multiple traps and is correlated with the decay of a g = 1.998 EPR signal, which appears after irradiation with X-rays.

TSL experiments determined that within the measured region sample synthesised in the air has five discrete traps with activation energies between 0.60 and 1.55 eV. In the case of the sample synthesised in a reducing atmosphere, the first four traps have the same activation energies as the traps of in the air synthesised sample. A significant difference in trap properties was observed for the deep traps. The synthesis in the reducing atmosphere promotes the emergence of closely overlapping trap levels. Additionally, the difference in the synthesis atmosphere impacts the distribution of filled traps in material: synthesis in a reducing atmosphere promotes an increase of shallow traps, thus, providing better PersL properties.

4.2. NIR emission of $MgGeO_3$: Cr^{3+}

4.2.1. Short introduction

Cr^{3+}-doped phosphors have drawn the attention of the scientific community ever since the discovery of the ruby laser in 1960. Recently a renewed interest has been evoked due to their use as NIR emitting luminescent materials [156,251].

NIR emitters are highly desired for applications in pharmaceutical, medical, cosmetics, food sciences, and agricultural industries [60]; thus, research and development of new effective materials are necessary.

This section of the dissertation reports on a novel broadband NIR emitting long afterglow phosphor $MgGeO_3$: Cr^{3+}. A series of samples with varying concentrations of Cr^{3+} was synthesised. Obtained samples will be denominated as MGO, and concentration of Cr^{3+} will be indicated with x where x = 0.10, 0.25, 0.50, 0.75, 1.00, 2.00 and 4.00 mol%. The optical properties were analysed using PL and PLE spectra, PersL spectra and kinetics. TSL and EPR measurements were performed to investigate the trap properties of the material.

4.2.2. Structure analysis

The phase composition of MGO samples was studied by powder XRD. The obtained XRD patterns and the standard PDF 00-034-0281 corresponding to $MgGeO_3$ are shown in **Fig. 4.11. (a)**. All the samples correspond to the single-phase orthorhombic $MgGeO_3$ phase. There is no meaningful difference between the XRD patterns for samples with varying Cr^{3+} concentrations, implying that Cr^{3+} fully incorporates into the lattice of $MgGeO_3$ without any significant changes in the host matrix. In addition, the phase purity of MGO samples was confirmed using Rietveld refinement. **Fig. 4.11. (b)** shows the result of the refinement for the sample with x = 0.25 mol%. The refinement factors indicate that the refined results are reliable. The change in cell volume obtained by the refinement is shown in **Fig. 4.11. (c)**. At first, cell volume decreases with increased Cr^{3+} doping level, an expected result if Cr^{3+} substitutes cation with a larger ionic radius. When the Cr^{3+} concentration exceeds 0.75 mol%, cell volume slightly increases with a further increase of the doping concentration. This could be explained by the incorporation of Cr^{3+} ions in interstitial sites or by forming Cr^{3+} clusters.

As previously discussed, $MgGeO_3$ consists of a three-dimensional network of [GeO_4] tetrahedrons and two types of [MgO_6] octahedrons. The ionic radii of the relevant cations are as follows: r(Ge^{4+}) = 0.39 Å (four-fold coordination), r(Mg^{2+}) = 0.72 Å (six-fold coordination) and r(Cr^{3+}) = 0.615 Å (six-fold coordination) [51]. Cr^{3+}, as a smaller ion, is expected to incorporate predominantly in the [Mg(I)O_6] site since it has a smaller volume than the [Mg(II)O_6] site [252]; however, if the concentration of Cr^{3+} is high enough, the substitution of other cationic positions may occur as well. Based on the crystal field stabilisation energy difference for Cr^{3+} in tetrahedral and octahedral environments, the incorporation of Cr^{3+} in the tetrahedral Ge^{4+} site is very unlikely [22]. It should be noted that aliovalent substitution is a complex process involving different charge compensation mechanisms; therefore, multiple Cr^{3+} centre configurations may originate from the same

lattice site. A striking example of this is seemingly simple MgO. Although there is only one obvious cation site for substitution, at least four Cr^{3+} centres have been reported [253].

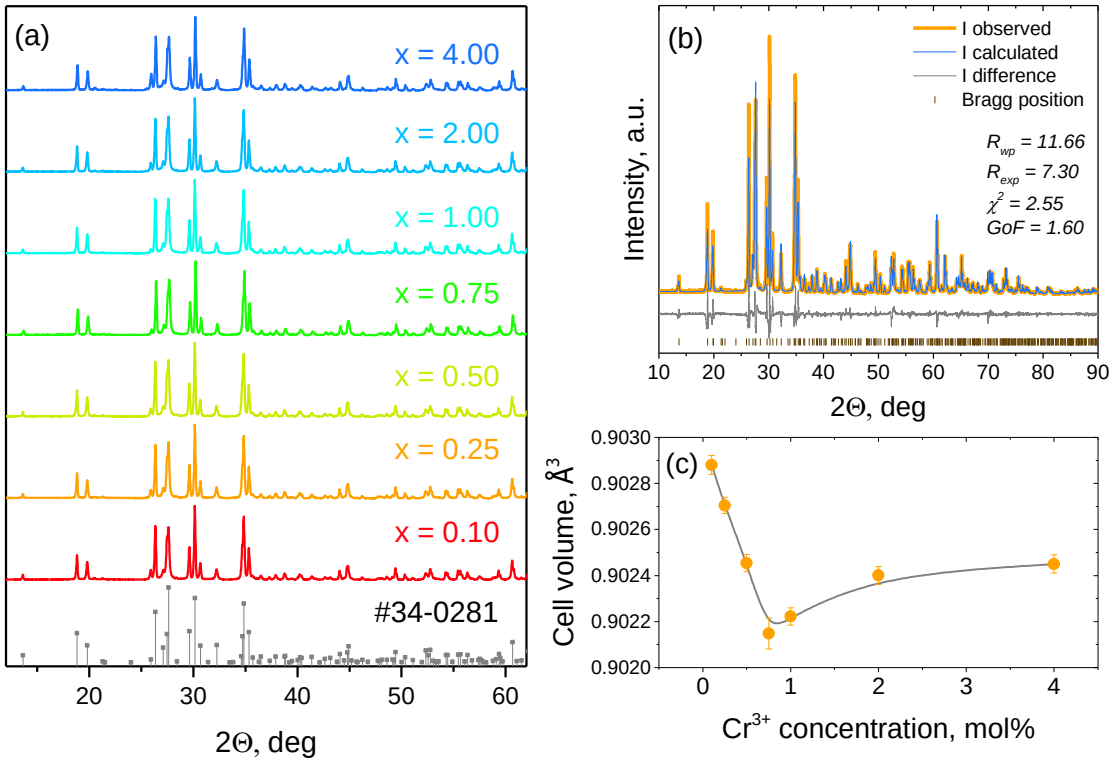

Fig. 4.11. (a) *XRD patterns of MGO samples and theoretical positions of MGO diffraction peaks according to JCPDS 34-0281,* ***(b)*** *observed and calculated powder XRD patterns, difference profile and the Bragg reflection positions for Rietveld refinement of the x = 0.25 mol% sample;* ***(c)*** *the unit cell volume of MGO samples.*

In order to analyse Cr^{3+} ion incorporation in MGO, EPR measurements and EPR spectra simulations were conducted; the results are shown in **Fig. 4.12.** In the case of large zero-field splitting, EPR spectra acquired at a higher microwave frequency are easier to interpret; thus, the Q microwave frequency band [230,254] was used. The x = 0.25 mol% sample was selected as a representative.

A comparison between the experimental EPR spectrum and simulated powder patterns of S = 3/2 systems, according to Ref. [230], suggests the presence of multiple Cr^{3+} centres in MGO. Tentative simulations of several signals in a model of S = 3/2 using the SH according to *Eq. (3.7)* were performed to obtain a superposition of simulated spectra corresponding to the experimental EPR spectrum. SH parameters (g, D and E) were manually adjusted to compare resonance positions in the experimental and simulation spectra. The obtained SH parameters are compiled in *Table. 4.2.*

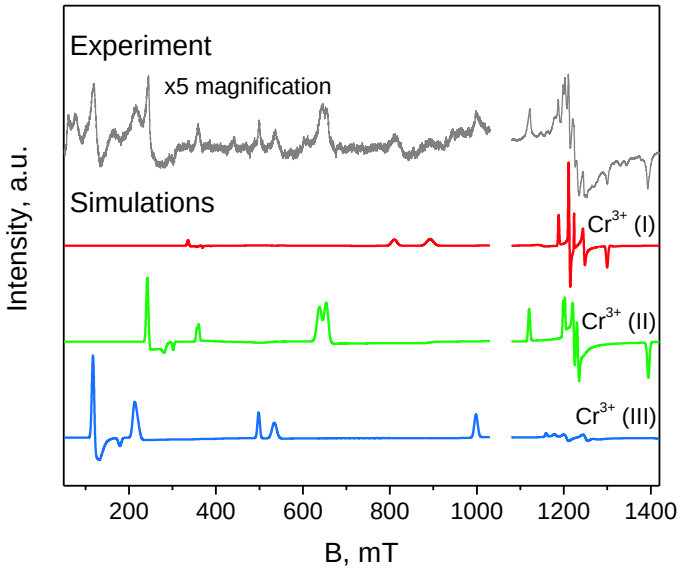

Fig. 4.12. *Experimental and simulated Q-band spectra of the x = 0.25 mol% sample; the 50 – 1030 mT range is shown in a 5-fold magnification.*

Table. 4.2. Evaluated SH parameters of Cr^{3+} centres in MGO.

Centre	***g***	***D, MHz***	***E, MHz***
Cr^{3+} (I)	1.973 ± 0.005	5800 ± 100	1200 ± 100
Cr^{3+} (II)	1.974 ± 0.005	8500 ± 200	2700 ± 100
Cr^{3+} (III)	1.974 ± 0.005	12100 ± 200	3600 ± 100

The simulation results coincide with the notion of multi-site occupancy of Cr^{3+} in the MGO lattice; Cr^{3+} ions incorporate into at least three isolated sites. However, additional investigations would be necessary, for unequivocal characterisation of the Cr^{3+} local structure in MGO.

4.2.3. Analysis of luminescence properties

Fig. 4.13. depicts PLE and PL emission spectra of MGO samples. All samples can be characterised with the same PLE bands with maxima at around 215 nm, 290 nm, 453 nm, and 650 nm. The 215 nm PLE band is attributed to the VB → CB transition of the host material, which is consistent with previously discussed aMGO and rMGO samples. The other three PLE bands are ascribed to the transitions of Cr^{3+}: $^4A_2(^4F) \rightarrow {}^4T_1(^4P)$ in the case of 290 nm, $^4A_2(^4F) \rightarrow {}^4T_1(^4F)$ in the case of 453 nm, and $^4A_2(^4F) \rightarrow {}^4T_2(^4F)$ in the case of 650 nm [118,255].

A broadband emission in the NIR spectral region (around 700-1200 nm) was observed for all samples when excited with 263 nm. The broad PL band consists of multiple sub-bands, with the two most prominent bands having maxima at 790 nm and 980 nm.

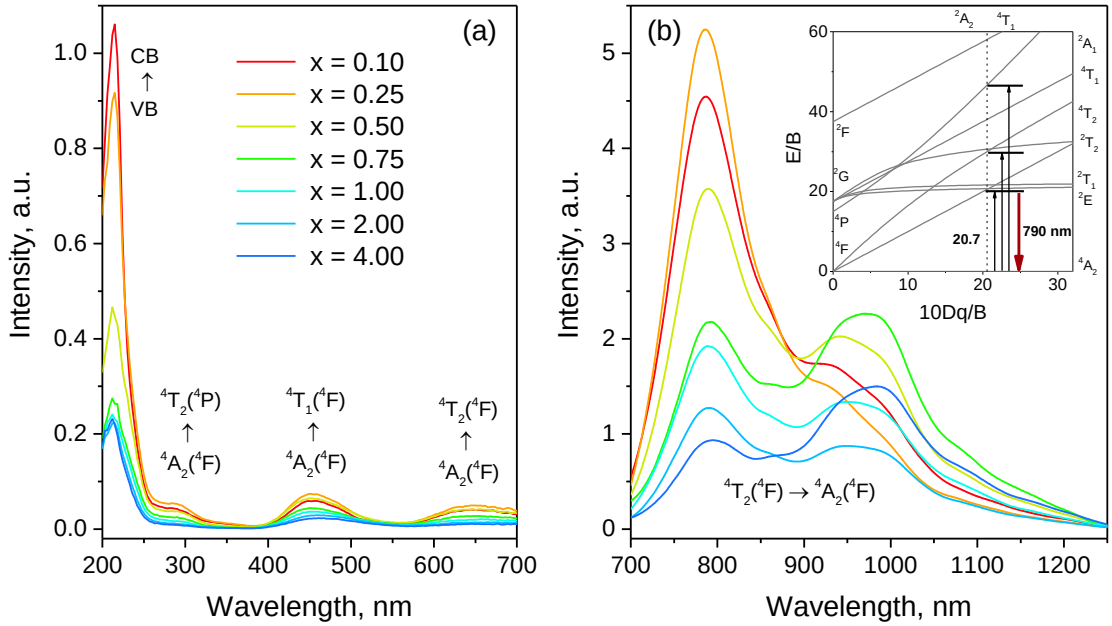

Fig. 4.13. (a) *PLE spectra of the MGO samples monitored at 800 nm and* ***(b)*** *PL spectra excited with 263 nm. Inset: simplified Tanabe–Sugano diagram of Cr^{3+} ions in MGO with calculated energy level positions.*

The inset of **Fig. 4.13. (b)** shows a simplified Tanabe–Sugano diagram of Cr^{3+} ion energy levels in the octahedral coordination together with *Dq/B* value estimated using *Eq. (1.16 – 1.18)* and PLE spectrum of x = 0.25 mol% sample. Out of the PL spectrum, only for the 790 nm peak, a PLE spectrum was obtained; thus, the results in the diagram represent only this one peak. Nevertheless, lower energy PL bands would represent Cr^{3+} in a weaker crystal field environment. From calculations, the *Dq/B* value is estimated to be around 2.07 ± 0.15, which is smaller than the threshold value of 2.3; thus, the crystal field of the host can be considered weak, and observed luminescence bands originate from the $^4T_2(^4F) \rightarrow {}^4A_2(^4F)$ Cr^{3+} transition.

For a detailed analysis of the PL properties of MGO samples, emission spectra were deconvoluted into sub-peaks by a Gaussian multiple peak fitting method. Selected examples (x = 0.1; 1.0; 4.0 mol%) are shown in **Fig. 4.14. (a-c)**. All PL spectra were easily fitted with the sum of three Gaussian peaks suggesting that there are at least three types of luminescence centres. This observation correlates with EPR measurements and simulations.

For the P1 and P3 sub-peaks, the PL decay profiles excited with 453 nm were measured and fitted with either one or the sum of two exponential equations *Eq. (1.3)*, respectively (**Fig. 4.15.**). According to the fit, the luminescence lifetime value for the P1 sub-band is τ_1 = 62.8 µs. The P3 sub-band could not be fitted with a single exponent and is characterised by fast τ_1 = 12.6 µs and slow τ_2 = 60.4 µs components. Luminescence lifetime on the order of µs is expected for the spin-allowed $^4T_2(^4F) \rightarrow {}^4A_2(^4F)$ transition of Cr^{3+}, and obtained results are comparable to the τ values of Cr^{3+} found in similar materials [256–258]; therefore, P1 and P3 are attributed to the luminescence from Cr^{3+} in two non-equivalent Mg^{2+}positions in the $MgGeO_3$ lattice. The $[Mg(I)O_6]$ site has a shorter average Mg-O bond length and smaller volume; thus, a relatively stronger crystal field is expected. Therefore, P1 most likely originates from the Cr^{3+} ions in $[Mg(I)O_6]$ site, while P3 is ascribed to Cr^{3+} in the

[Mg(II)O_6] site. On the other hand, the origin of the P2 sub-band is less clear. It could be assigned to either the PL of Cr^{3+} in the third isolated site revealed by EPR analysis or to the PL of Cr^{3+}–Cr^{3+} ion pairs. Previous reports [259,260] on Cr^{3+}–Cr^{3+} ion pairs have concluded that PL lifetime values of pair luminescence are around an order of magnitude smaller than the lifetime value of single Cr^{3+} luminescence. However, the intensity of P2 compared to P1 and P3 is insignificant, and it is not possible to make certain statements. Additionally, some other, weaker luminescence signals may be hidden under the sum of the three Gaussian peaks.

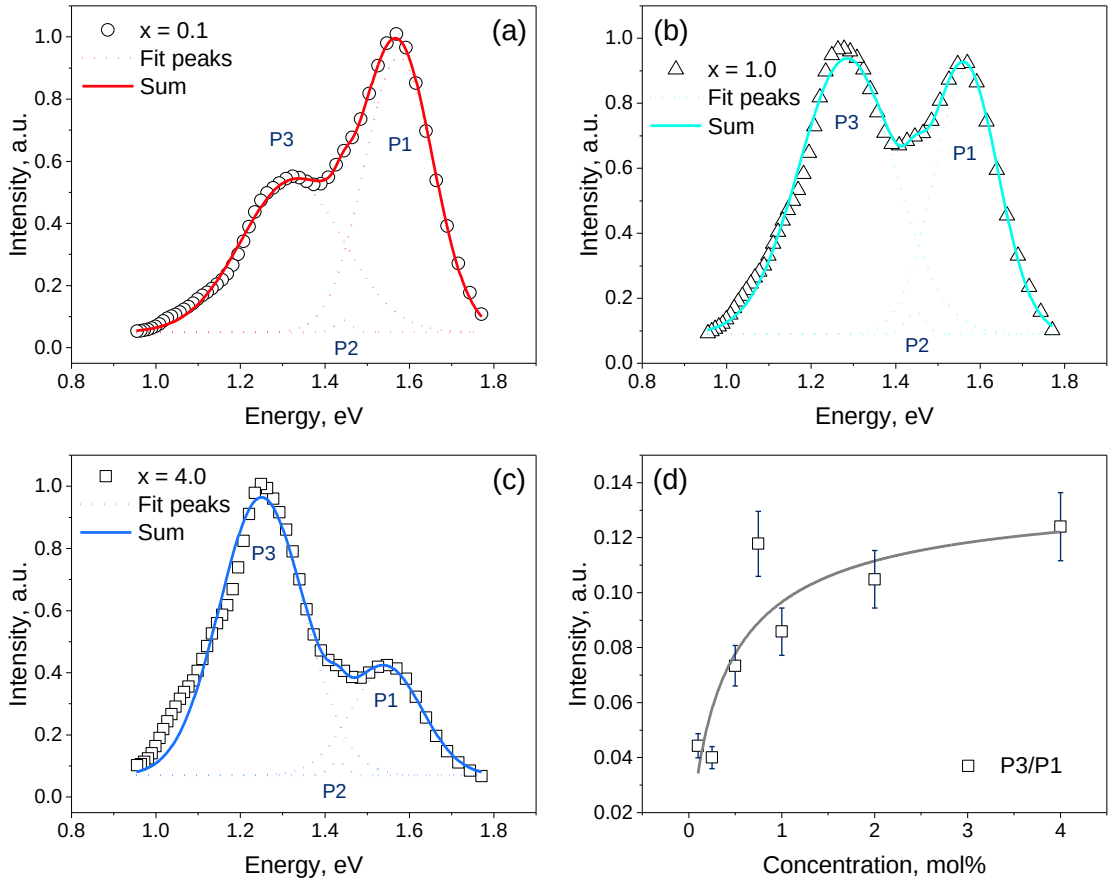

Fig. 4.14. *Gaussian peak decomposition of the selected emission spectra of MGO samples (x = 0.1; 1.0; 4.0 mol%) under the excitation of 263 nm* ***(a, b, c)****, and the ratio of P3 vs P1* ***(d)****.*

Fig. 4.14. (d) depicts the ratio of P1 and P3 intensities which changes depending on Cr^{3+} concentration with a general tendency to increase the relative intensity of the lower energy sub-peak P3 with the increase of dopant concentration. Hence, the luminescence of MGO is tuneable. This could be explained by an interplay of several previously reported effects in Cr^{3+} doped germanate materials. Firstly, as previously mentioned, when the Cr^{3+} doping concentration is small, there is a site occupancy preference in favour of the [Mg(I)O_6] site [261]. Secondly, if the Cr^{3+} concentration increases, the distance between the Cr^{3+} ions decreases, possibly resulting in concentration quenching. This effect is more prominent for adjacent Cr^{3+} in sites with shorter average bond lengths [261,262]. Therefore, P1 should be more affected than P3. And thirdly, it is reported [263] that the energy migration between nearby Cr^{3+} ions from an excited Cr^{3+} ion to a Cr^{3+} ion with a lower $^4T_2(^4F)$ level is likely. In the

case of MGO, this could lead to the increased population of the excited state of Cr^{3+} in the $[Mg(II)O_6]$ site through energy migration from the Cr^{3+} in the $[Mg(I)O_6]$ site.

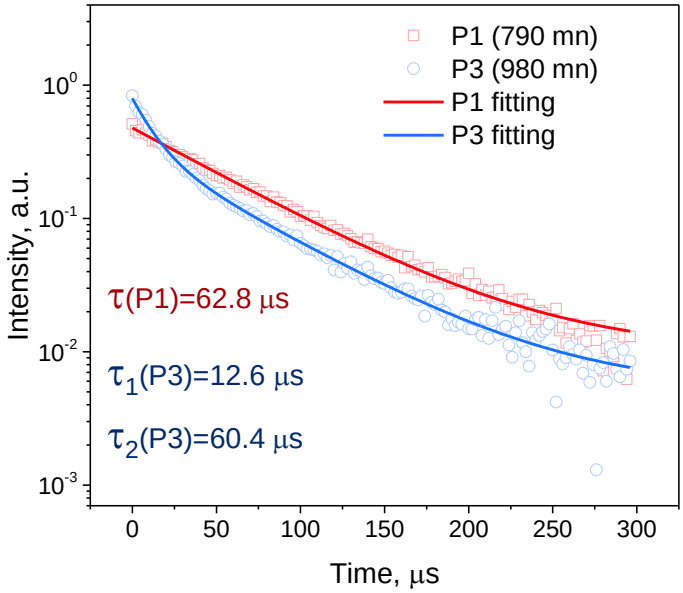

Fig. 4.15. *Decay kinetics of PL of x = 0.25 mol% sample excited with 453 nm and monitored at 790 (P1) or 980 nm (P3).*

After irradiation for 10 min with 263 nm, an afterglow of the Cr^{3+} NIR luminescence band is easily detectable for more than 16 h. The PersL decay curves of the MGO samples are shown in **Fig. 4.16**. The best PersL properties were observed for the x = 0.25 mol% sample, closely followed by the x = 0.10 mol% sample. Further increase of the Cr^{3+} concentration leads to a decrease in the initial intensity and the longevity of the afterglow. As discussed, PersL decay generally follows *Eq. (1.12)* and, in a double-logarithmic scale, appears as a straight line with a slope of $-l$. If the l value is close to 1, the mechanism of PersL is governed by tunnelling; the trapped electron can move from the trap to a nearby excited state of the luminescence centre without thermal detrapping to the CB. In the case of MGO samples, regardless of the concentration of Cr^{3+}, the principal parts of the decay profiles are easily fitted with *Eq. (1.12)*, with l values oscillating between 0.95 and 1.03.

Unlike the classical "trap centre → CB → luminescence centre" model, detrapping of charge carriers through tunnelling does not require additional thermal energy; thereby, PersL should be expected in low-temperature conditions. MGO maintains its PersL phosphor properties not only at 150 K but even at 10 K temperatures. The afterglow decay curves of the x = 0.25 mol% sample at low temperatures are shown in the inset of **Fig. 4.16.** Note that TSL measurements in the 10 – 300 K temperature range were performed, and no glow peaks were detected. This clearly affirms the presence of the athermal tunnelling mechanism in the PersL process in the MGO material.

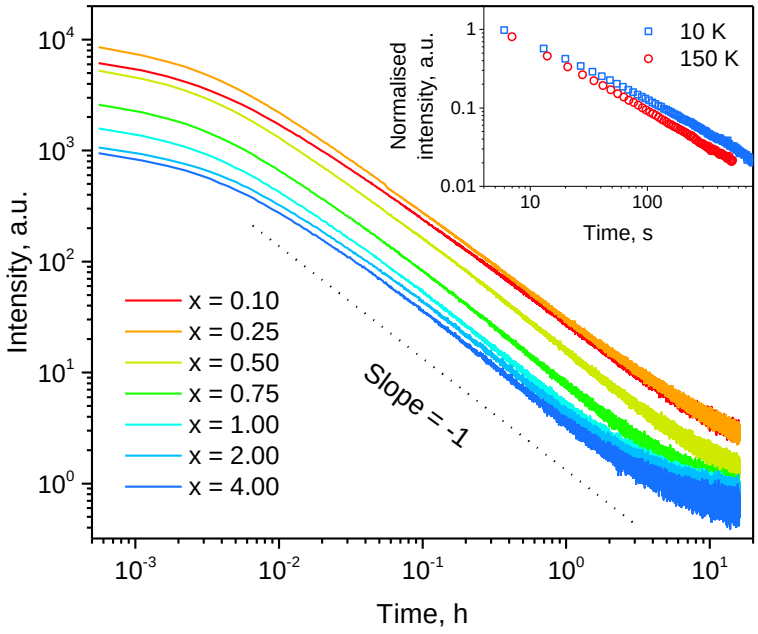

Fig. 4.16. *The afterglow decay curves of the MGO samples after irradiation for 10 min with 263 nm at 25 °C. Inset: the afterglow decay curves of the x = 0.25 mol% sample after irradiation for 10 min with 263 nm at 10 K and 150 K temperature, double-logarithmic plot.*

4.2.4. Analysis of trap properties

To investigate the trap properties of the MGO material, several TSL and EPR measurements and analyses were performed. TSL glow curves of the MGO samples after irradiation with 263 nm and a heating rate of 1 °C/s are shown in **Fig. 4.17**.

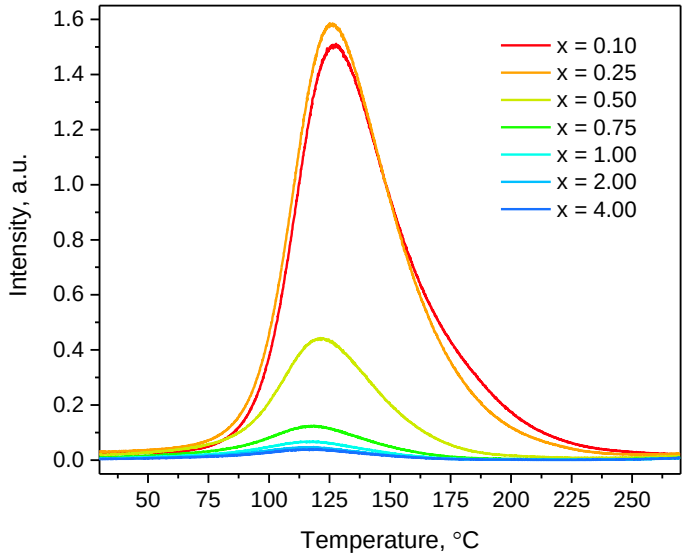

Fig. 4.17. *TSL glow curves of the MGO samples after irradiation with 263 nm.*

There is no significant change in the structure and peak positions of the glow curves; thus, increasing the concentration of Cr^{3+} ions does not create new trap centres. On the

contrary, the intensity of the TSL signal varies a lot. As a rule, the higher intensity of the glow peak at an appropriate temperature range results in better PersL properties – higher initial intensity and/or greater longevity. Based on the TSL data, out of the series, the best PersL materials are x = 0.10 and x = 0.25 mol% samples; this result coincides with the afterglow decay measurements (**Fig. 4.16.**).

An extensive analysis of the x = 0.25 mol% sample was conducted to determine the nature of trap centres and corresponding trap depth values. First, the T_{max} – T_{stop} method was applied. The TSL glow curves of the sample after preheating from T_{stop} = 30 °C to T_{stop} = 230 °C with a step of 5 °C were measured and are shown in **Fig. 4.18. (a)**, the T_{max} – T_{stop} plot is demonstrated in **Fig. 4.18. (b)** as blue squares. Two linear equations can easily fit it. Up to T_{stop} = 100 – 120 °C, the T_{max} value is around 125 °C. This could be perceived as an indication of a discrete trap centre. However, in this case, the most likely explanation is that when T_{stop} is below a threshold value, the relatively deep traps present in MGO material are not significantly affected; thus, the peak of the glow curve does not change its position. When T_{stop} > 120 °C, T_{max} values increase linearly, suggesting continuously distributed or closely overlapping trapping levels.

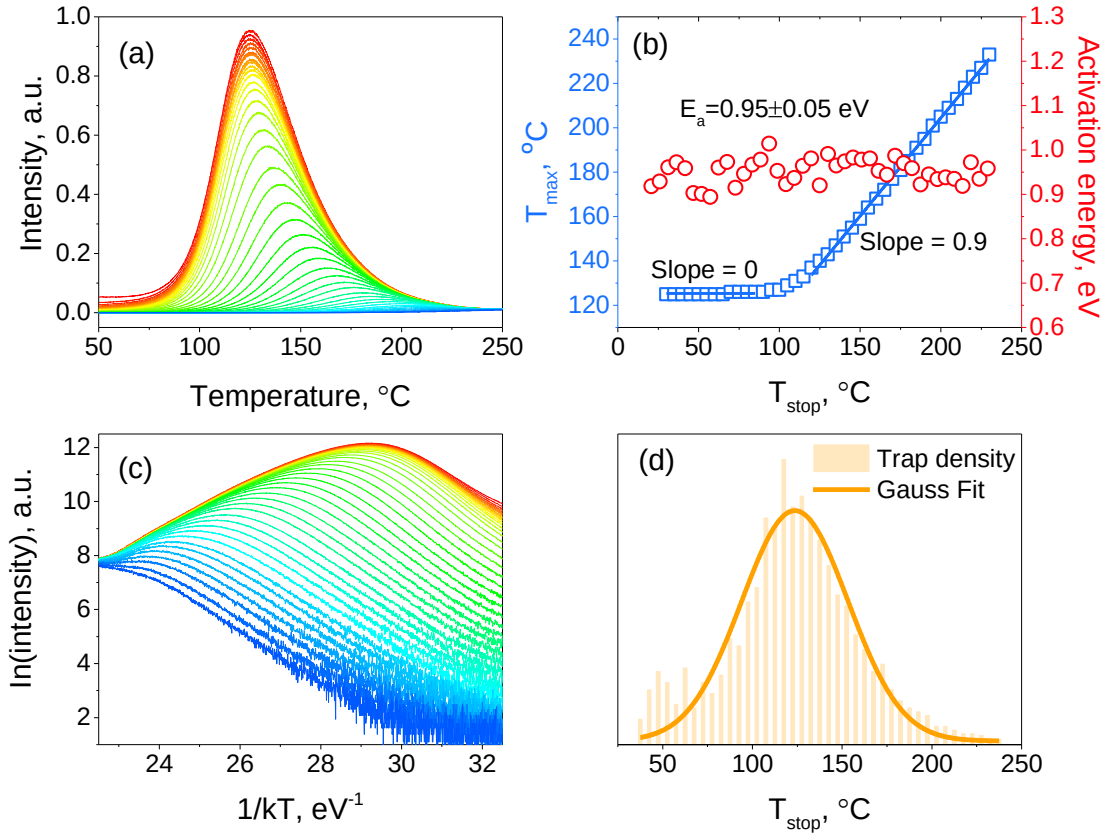

Fig. 4.18. (a) *TSL glow curves of the x = 0.25 mol% sample measured after preheating to T_{stop} from 30 °C to 230 °C;* ***(b)*** *T_{max} – T_{stop} plot and E_a values obtained by IRA;* ***(c)*** *IRA of the data obtained from T_{max} – T_{stop} experiment and* ***(d)*** *the calculated trap density distribution. The sample was charged with 263 nm.*

The T_{max} – T_{stop} measurements were used to determine the activation energy E_a. For this purpose, the IRA was used. According to *Eq. (3.3).*, if *ln(I)* is plotted as a function of *1/(kT)*, a straight line with a slope - E_a is obtained. The Arrhenius plots are shown in **Fig. 4.18.**

(c); the determined E_a values are shown as the red circles in **Fig. 4.18. (b)**. The E_a value was found to be constant: 0.95 ± 0.05 eV, which considering the $T_{max} - T_{stop}$ plot, is somewhat counterintuitive. However, similar results have been reported previously [24,264], and it has been suggested that in the case of a continuous trap distribution, IRA may predominantly give the E_a value of the shallower traps. Thus, it is concluded that relatively deep, closely overlapping trapping levels exist in the MGO material.

Continuous trap distributions may vary by shape. Analysing $T_{max} - T_{stop}$ glow curves based on the technique described in *Subsection 3.4.1.1.,* the trap density distribution of MGO material was found. It likely follows a Gaussian profile **Fig. 4.18. (d)**. The Gaussian profile could indicate that the TSL glow curve and, consequently, PersL are produced by detrapping a single defect type with varied surroundings

Since the trap depth in the MGO material is deep, efficient PersL should not be expected; however, results have proven the opposite. This is another indication that the detrapping process in the MGO material at RT is dominated by the athermal tunnelling of charge carriers from the traps to the luminescence centres.

To investigate defect creation in MGO, EPR measurements before and after UV radiation exposure were conducted; the results are shown in **Fig. 4.19**. To minimise the contribution of Cr^{3+} signals to the EPR spectra, the sample with the smallest doping concentration (x = 0.10 mol%) was used for the analysis. After the irradiation with UV, complex EPR signals in the 342 – 361 mT range emerge.

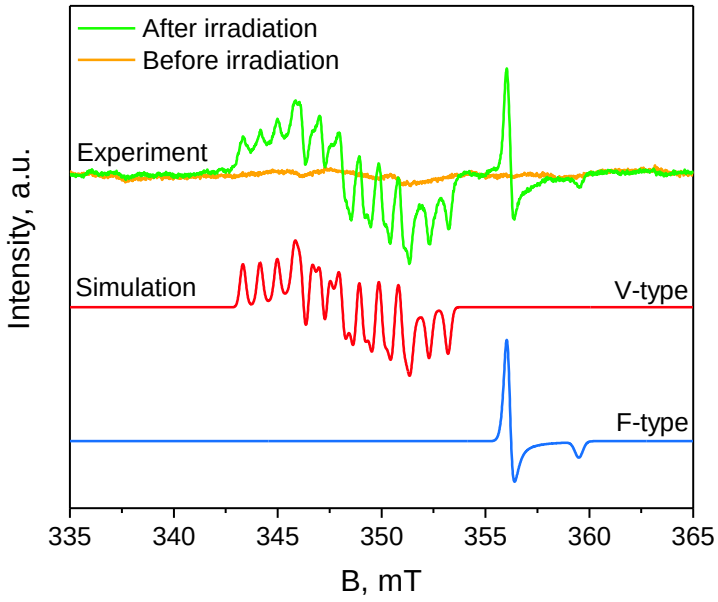

Fig. 4.19. *EPR spectra of the x = 0.10 mol% sample before and after UV irradiation.*

To determine the SH parameters of the UV-generated paramagnetic centres, EPR spectra simulations were performed. The SH used in the simulations: *Eq. (3.8).* The experimental spectrum was determined to be a superposition of signals of two S = 1/2 systems labelled "V-type" and "F-type". For the V-type centre, hyperfine interaction with a I = 5/2 nucleus was resolved in the spectrum. The fitted SH parameter values for the two identified centres are summarised in *Table 4.3*.

Table 4.3. The fitted SH parameters of the UV-generated paramagnetic centres.
Δg_i = 0.0005; ΔA_i = 0.5 MHz.

Centre	g_1	g_2	g_3	A_1, MHz	A_2, MHz	A_3, MHz
V-type	2.0346	2.0160	2.0025	23.6	26.8	25.4
F-type	1.9734	1.9734	1.9548			

The determined values indicate the presence of single hole (V-type) and electron (F-type) centres in MGO. In oxide hosts, holes are commonly trapped on oxygen ions, forming S = 1/2 O^- centres. The centres are typically characterised by *g*-factor with the values in the range of 2.00 – 2.05 [265–268], which coincide with the results in *Table 4.3.* The detected centre in MGO exhibits a hyperfine structure with a 100 % abundant I = 5/2 nucleus. Possible candidates could be ^{27}Al and ^{55}Mn isotopes, which are expected trace impurities from the precursors. From the detection of the hyperfine structure, it can be concluded that the holes are captured on oxygen ions with the respective impurity ions nearby. Common electron traps in oxides are oxygen vacancies. A single electron trapped at an oxygen vacancy, i.e., the F^+ centre, is the most straightforward S = 1/2 F-type centre. The axial symmetry of the *g*-factor suggests that the electron could be localised at a complex consisting of an oxygen vacancy and another lattice defect [267–269]; however, since there is not a hyperfine structure, nothing more can be concluded.

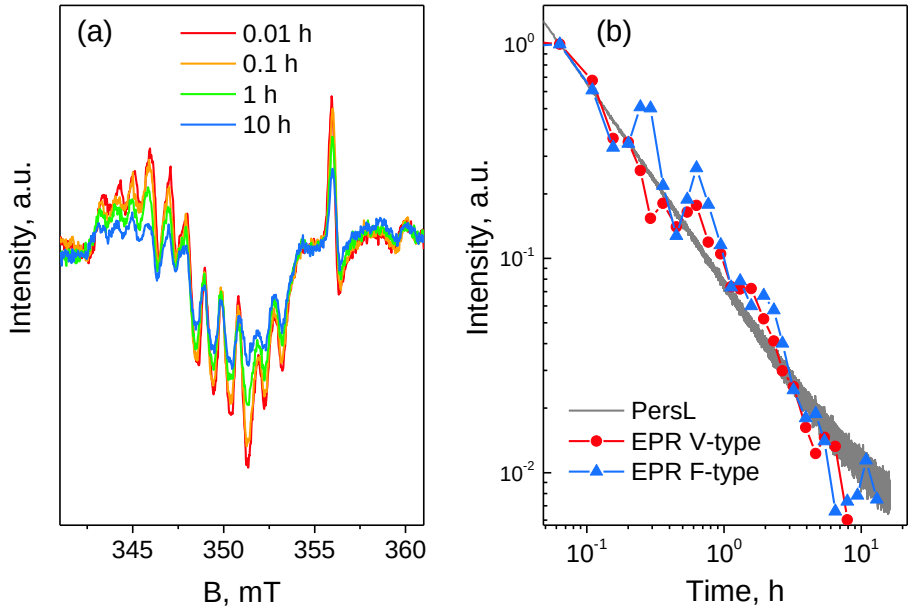

Fig. 4.20. (a) *EPR spectra decay with time of the x = 0.1 mol% sample after UV irradiation;* ***(b)*** *EPR signal intensity decay compared to PersL decay kinetics; double logarithmic plot.*

To determine the role of the identified centres in the PersL of MGO, the decay of the EPR spectra with time was monitored (**Fig. 4.20. (a)**). The gradual decay of both paramagnetic centres was observed at RT. The EPR signal intensity change was evaluated the same as in the case of aMGO and rMGO samples. Obtained results overlayed with the

PersL decay profile of the same sample are shown in **Fig. 4.20. (b)**. The analysis demonstrates that the decay rate of the paramagnetic centres is correlated with the decay of PersL. Therefore, the experimental results strongly indicate that the detected V-type and F-type centres in MGO play a critical role in the mechanism of PersL.

To correlate the EPR and TSL data, annealing of the paramagnetic centres was carried out. The obtained results are shown in **Fig. 4.21.** The V-type and F-type centres generated by irradiation with UV rapidly decay after annealing temperature reaches the 75 – 150 °C range; this is in agreement with both the temperature maxima of the TSL glow curves in **Fig. 4.17.** and trap density distribution in **Fig 4.18. (d)**. The V-type centre exhibits slightly higher temperature stability than the F-type centre. A similar effect has been previously reported and explained by an alternative recombination channel for the V-type centre with other host defects [270].

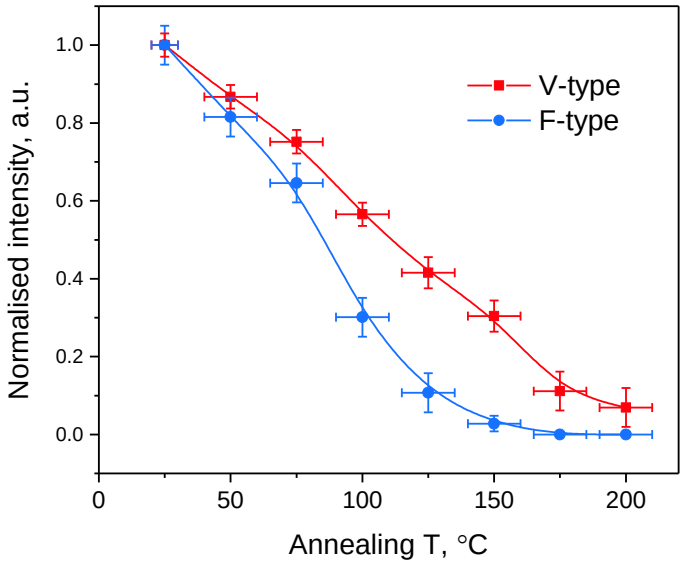

Fig. 4.21. *Paramagnetic centre annealing behaviour of the x = 0.1 mol% sample after UV irradiation.*

4.2.5. Mechanism of the PersL

Based on the results above, the primary mechanism of PersL in MGO is proposed in **Fig. 4.22**. Note that the locations of the energy levels and traps are shown schematically and not to scale. Firstly, electrons are excited directly to the CB under UV irradiation, leaving holes in the VB. Charge carriers move through the bands until either recombination resulting in the PL of Cr^{3+} occurs, or the carriers are captured by the traps. Most of the trap centres themselves are linked to oxygen atoms. Oxygen vacancies serve as the electron traps: $V_O^{\bullet\bullet} + e^- \rightarrow V_O^{\bullet}$ or $V_O^{\bullet\bullet} + 2e^- \rightarrow V_O^{\times}$, at the same time, the holes are trapped on oxygen ions and form O^- centres: $O^{2-} + h^+ \rightarrow O^-$.

When irradiation is stopped, charge carriers may escape the traps. Since the determined E_a values are too large for effective detrapping through CB and VB at RT, the main route of detrapping is athermal tunnelling from the traps directly to Cr^{3+} ions. As the last step, the recombination at Cr^{3+} ions substituting different positions in the host matrix occurs, resulting in long broadband NIR PersL.

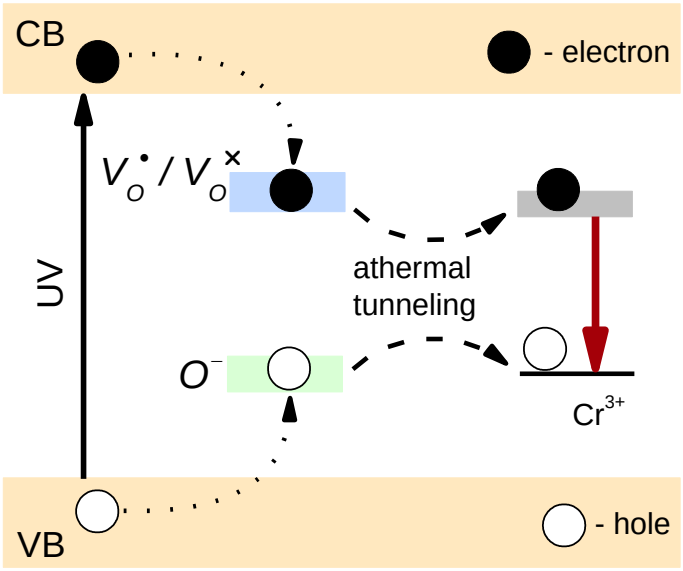

Fig. 4.22. A schematic diagram of the PersL mechanism in the MGO material.

4.2.6. Summary

A novel broadband NIR PersL phosphor $MgGeO_3$, doped with various concentrations of Cr^{3+}, has been successfully synthesised by the solid state reaction synthesis method. The most likely origin of the broadband NIR luminescence is the $^4T_2(^4F) \rightarrow {}^4A_2(^4F)$ optical transition of Cr^{3+} ions substituting predominantly two non-equivalent Mg^{2+} positions present in the host matrix.

For the best performing samples: x = 0.10 and 0.25 mol%, a strong PersL signal can be detected for at least 16 h after irradiation with 263 nm UV light for 10 min.

Analysis of the EPR and TSL measurements revealed that the main trap centres responsible for PersL are intrinsic and can be categorised into two types: oxygen vacancies that serve as electron traps and oxygen ions that serve as hole traps. The traps in the material can be considered deep and are closely overlapping with $E_a \geq 0.9$ eV. The trap density distribution closely follows the Gaussian profile.

The primary detrapping mechanism in MGO is athermal tunnelling from traps directly to the luminescence centres. Therefore, the MGO material is a promising NIR persistent phosphor for applications not only at room or higher temperatures but also at low-temperature conditions. This may be beneficial in advanced fields such as anti-counterfeiting, night-vision surveillance, etc. Additionally, since the emission of MGO covers the first and partially second biological windows, where low scattering and absorption of light guarantee deeper tissue penetration, a great potential for numerous biological applications for this material is evident.

4.3. Red emission of $Mg_2Si_{1-x}Ge_xO_4$: Mn

4.3.1. Short introduction

A composition modification of the host structure is a promising strategy to create an optimal environment for the activators and, thus, improve PersL properties [271]. Due to excellent solubility, several germanate–silicate solid solution systems such as $Y_2Si_{1-x}Ge_xO_5$: Pr^{3+} [272], $LiLuSi_{1-x}Ge_xO_4$: Eu^{3+} [273], $Mg_3Y_2(Ge_{1-x}Si_x)_3O_{12}$: Ce^{3+} [102], etc., have been proposed. Significant changes in PL, PersL, and TSL behaviours have been observed in most of these materials, depending on the Si/Ge ratio. To my knowledge, there are no reports on the spectroscopic properties of manganese doped $Mg_2Si_{1-x}Ge_xO_4$ solid solutions.

In this section of the dissertation, a design of manganese doped $Mg_2Si_{1-x}Ge_xO_4$ (x = 0.0 - 1.0) solid solutions and their PL and PersL properties are discussed in detail. TSL and EPR spectroscopy analysis is performed to obtain insight into the nature and properties of the traps. As a result, the optimal Si/Ge ratio is determined, and the possible PersL mechanism in the material is discussed.

Here a doping concentration of Mn is set at 0.1 mol%, and $Mg_2Si_{1-x}Ge_xO_4$: 0.1 mol% Mn (x = 0.0; 0.1; 0.2; 0.3; 0.4; 0.5; 0.6; 0.7; 0.8; 0.9; 1.0) materials will be denominated as MSGO with x values indicated where applicable.

4.3.2. Structure analysis

The structure of MSGO samples was characterised by XRD measurements. The obtained XRD patterns and standard cards PDF 01-084-1402 corresponding to orthorhombic Mg_2SiO_4 and PDF 00-036-1479 corresponding to orthorhombic Mg_2GeO_4 are shown in **Fig. 4.23**. The peak positions of the samples matched well with the PDF patterns, and no additional phases could be identified, confirming the formation of $Mg_2Si_{1-x}Ge_xO_4$ solid solutions. The XRD peak positions gradually shift to smaller 2Θ values when Ge^{4+} content increases in the samples. This is an expected effect due to the isovalent substitution of relatively smaller Si^{4+} ions with larger Ge^{4+} ions leading to the expansion of interplanar distances. Slight broadening of XRD peaks for samples x = 0.4 – 0.6 could be associated with crystal lattice distortion due to random replacement of Si^{4+} positions with Ge^{4+} or slight exsolution.

Rietveld refinement was applied to the XRD patterns, and the lattice parameters depending on the x value were determined. Change of the lattice parameters follows Vegard's law, and data points can be well fitted with a straight line (**Fig. 4.24.)**.

The crystal structure of the Mg_2SiO_4 and Mg_2GeO_4 compounds consists of two distinct [MgO_6] octahedrons and either [GeO_4] or [SiO_4] tetrahedrons. The ionic radii of the present cations are r(Ge^{4+}) = 0.39 Å (four-fold coordination), r(Si^{4+}) = 0.26 Å (four-fold coordination), r(Mg^{2+}) = 0.72 Å (six-fold coordination), r(Mn^{2+}) = 0.67 Å (six-fold coordination), r(Mn^{4+}) = 0.53 Å (six-fold coordination) and r(Mn^{4+}) = 0.39 Å (four-fold coordination) [51]. According to the ionic radii and the valence, Mn^{2+} ions most likely occupy both Mg^{2+} sites. Likewise, one could expect that Mn^{4+} ions would substitute Ge^{4+} ions. However, it is known that Mn^{4+} ions strongly prefer an octahedral environment [274,275].

Therefore, the most likely positions of Mn^{4+} in the lattice are [MgO_6] octahedrons as well. However, in this case, a significant charge compensation would be necessary. Thus, an insignificant amount of Mn^{4+} is expected in MSGO samples.

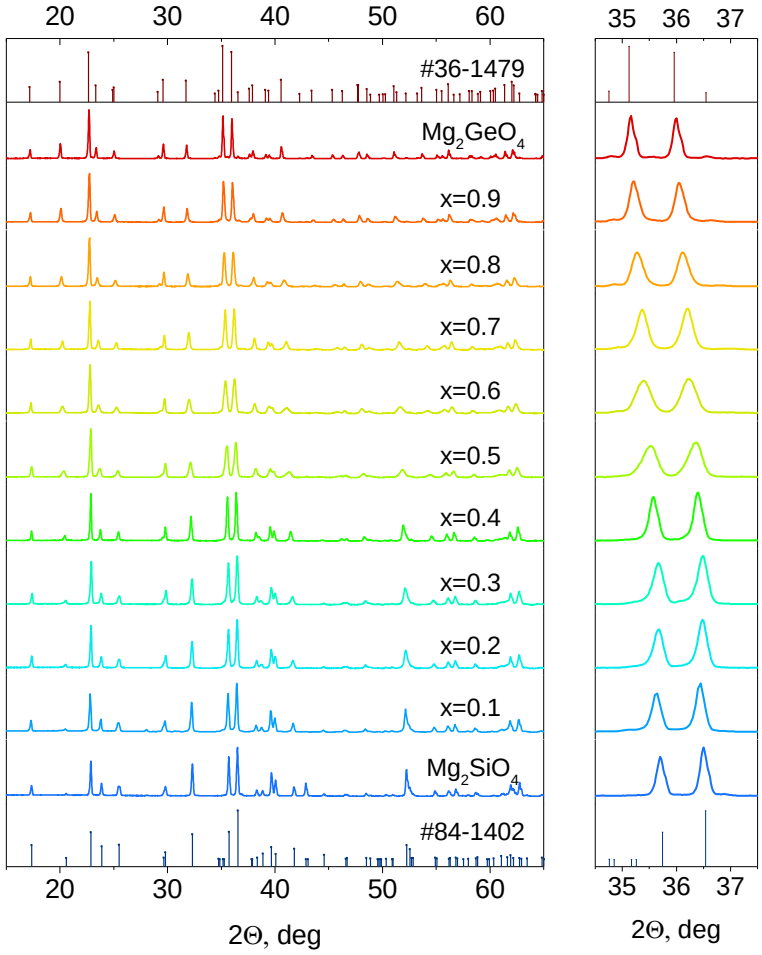

Fig. 4.23. *XRD patterns of MSGO samples and theoretical positions of Mg_2SiO_4 (PDF 01-084-1402) and Mg_2GeO_4 (PDF 00-036-1479) and enlarged partial image.*

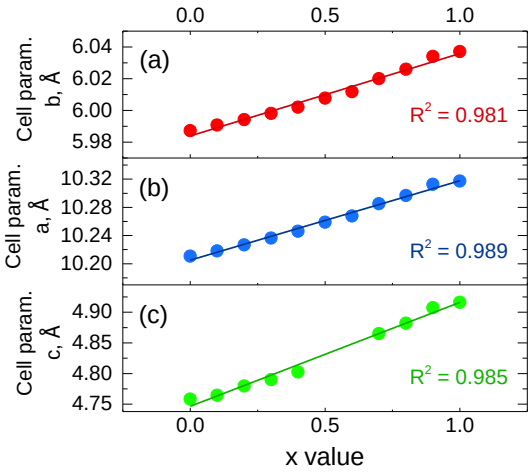

Fig. 4.24. *Dependence of the lattice parameters of MSGO samples on x value.*

4.3.3. Analysis of luminescence properties

The PL measurements reveal the coexistence of Mn^{2+} and Mn^{4+} in most of the MSGO samples. The normalised and as-measured PL spectra of selected samples excited with 263 nm are shown in **Fig. 4.25. (a, b)**. The Mg_2SiO_4 sample has a relatively weak Mn^{2+} luminescence band with a maximum at 740 nm. A PL covering the visible part of the spectrum was also observed. The most likely origin of this emission is a sum of host-related luminescence in the blue and green regions and another Mn^{2+} band in the red region. Once Ge^{4+} is introduced into the material, a Mn^{4+} typical relatively sharp red PL band with a maximum at 660 nm emerges. With an increased Ge^{4+} content, the relative intensity of the Mn^{4+} band increases and starting from x = 0.3, it completely dominates in the spectrum. The highest PL intensity was observed for the Mg_2GeO_4 sample.

Excitation with 263 nm simultaneously coincides with multiple relatively broad PLE bands related to Mn^{2+} and Mn^{4+}, one of which is the Mn^{4+} transition from the ground state $^4A_2(^4F)$ to excited state $^4T_1(^4F)$ [276]; this transition is spin-allowed; thus, even at minuscule doping concentration, an efficient Mn^{4+} PL is not surprising. On the contrary, the change of Mn^{4+} PL intensity depending on the x value can not be unambiguously explained. This behaviour is likely linked to a complex charge compensation mechanism in the case of aliovalent substitution of Mg^{2+} with Mn^{4+}; however, additional experiments are necessary for precise interpretation.

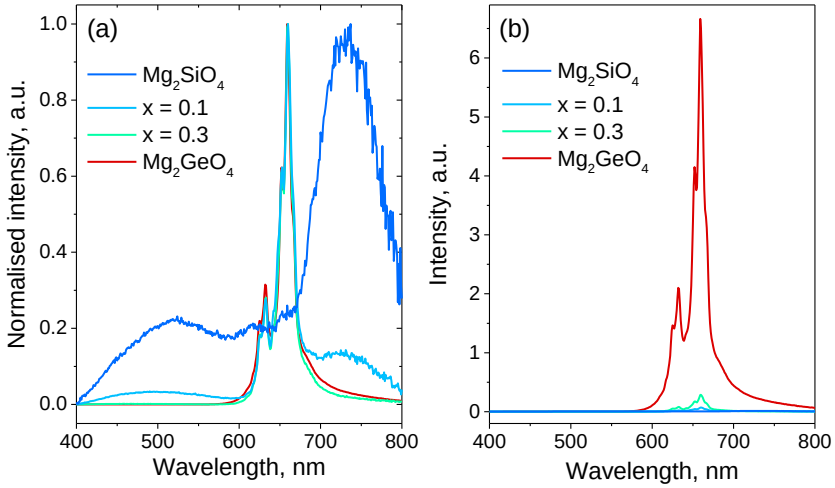

Fig. 4.25. (a) *Normalised PL spectra of Mg_2SiO_4, Mg_2GeO_4, and MSGO x = 0.1 and 0.3 samples excited with 263 nm,* ***(b)*** *the same spectra as-measured.*

For an in-depth analysis of PL properties, the x = 0.1 sample was chosen. The PL-PLE contour plot and selected PL and PLE spectra are shown in **Fig. 4.26 (a)** and **(b)**, respectively. By selecting specific excitation wavelengths, it is possible to observe three distinct PL bands: an above discussed Mn^{4+} band resulting from the $^2E(^2G) \rightarrow {}^4A_2(^4F)$ optical transition and two broad Mn^{2+} bands with maxima at 637 and 730 nm corresponding to $^4T_1(^4G) \rightarrow {}^6A_1(^6S)$ optical transition of Mn^{2+} in two non-equivalent Mg^{2+} sites [209]. If the sample is excited with 205 nm, corresponding to the VB → CB transition, a broad PL band matching the sum of both

Mn^{2+} bands emerge. The same emission bands appear in the PersL spectra, as will be discussed later.

All PLE bands, including CTBs and inter-atomic bands of Mn^{2+} and Mn^{4+} ions, correspond to previous reports on similar materials [210,236,277].

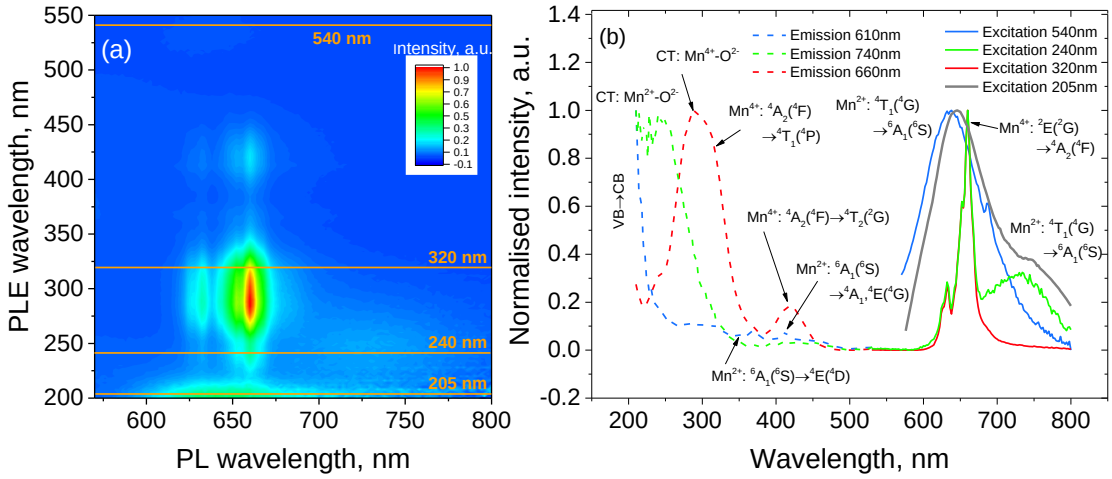

Fig. 4.26. (a) *PL-PLE contour plot of x = 0.1 sample;* ***(b)*** *PLE (λ_{em} = 610, 660, 740 nm) spectra and PL (λ_{ex} = 205, 240, 320, 540 nm) spectra of the x = 0.1 sample.*

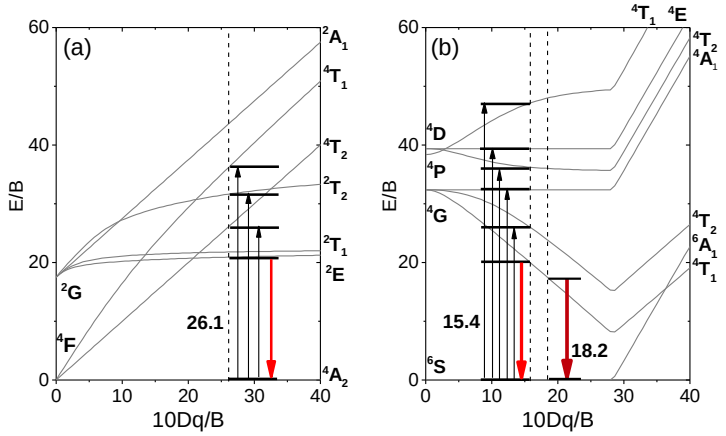

Fig. 4.27. *Simplified Tanabe–Sugano diagram for Mn^{4+}* ***(a)*** *and Mn^{2+}* ***(b)*** *electron configuration in the octahedral crystal field with estimated energy level positions in the case of x = 0.1 sample.*

By using *Eq. (1.16 – 1.19)* and PLE and PL spectra of the MSGO x = 0.1 sample presented in **Fig. 4.26 (b)**, simplified Tanabe-Sugano diagrams for Mn^{4+} and Mn^{2+} electron configurations in the octahedral crystal field with estimated energy level positions were obtained. The resulting diagrams are shown in **Fig. 4.27.** The dashed lines represent estimated *10Dq/B* values. In the case of Mn^{2+}, the value of *B* was calculated to be 782 cm^{-1}. The energy *E* of 637 nm emission is 15699 cm^{-1}; accordingly, the *E/B* value was calculated to be 20.08. Based on the *E/B* value and Tanabe-Sugano diagram shown in **Fig. 4.27 (b),** the *10Dq/B* value is estimated to be around 15.4. The same calculations were applied for the 730 nm band, and a *10Dq/B* value of 18.2 was obtained. The crystal field parameter *10Dq/B* of Mn^{4+} was estimated to be around 26.1. Some PLE and PL band position changes

depending on the x value were observed; however, no meaningful conclusions can be drawn since there is a substantial overlap of both the PL and PLE bands, which makes it challenging to determine the exact energy values necessary for calculations.

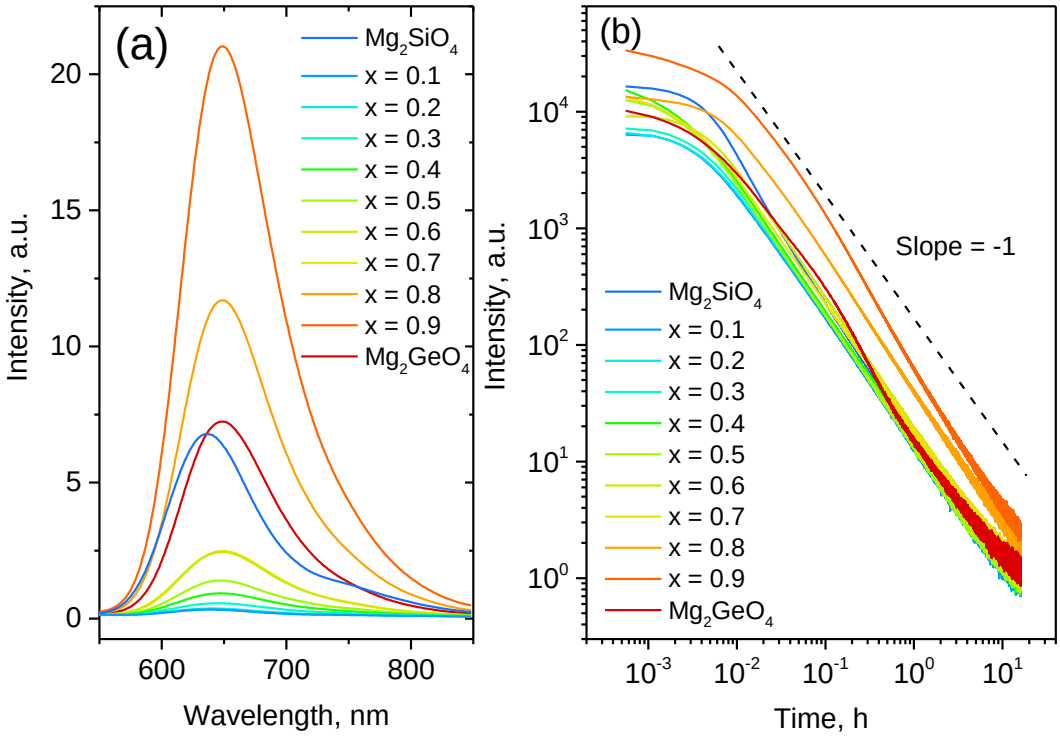

Fig. 4.28. (a) *PersL spectra of the MSGO samples a few minutes after cessation of irradiation with 263 nm and* ***(b)*** *the afterglow decay curves of the same samples after irradiation for 3 min with 263 nm at 25 °C temperature*.

After cessation of the 263 nm excitation, all samples can be characterised with two strongly overlapping PersL bands ascribed to the Mn^{2+} transition $^4T_1(^4G) \rightarrow {}^6A_1(^6S)$ of Mn^{2+} in two non-equivalent Mg^{2+} sites. As evident from **Fig. 4.28. (a)**, no detectable Mn^{4+} afterglow can be observed, thus, confirming the notion of insignificant Mn^{4+} concentration in samples. Additionally, the shorter wavelength luminescence band, corresponding to a weaker crystal field position, dominates in the PersL spectra of all MSGO samples.

Based on the PersL decay curves, the most perspective red PersL phosphor out of the MSGO series is the x = 0.9 sample. PersL of all samples could be easily detected for at least 16 h after 3 min irradiation with 263 nm. Decay curves of the PersL of all samples plotted in a double-logarithmic scale are shown in **Fig. 4.28. (b)**. A dashed line represents a slope of -1. Most of the samples cannot be fitted with a single line, indicating the complexity of the PersL process with the involvement of multiple trap centres. The sample with the best PersL properties, x = 0.9, clearly does not follow the "-1" line; thus, although tunnelling cannot be entirely ruled out, it is doubtful that it plays a significant role in the RT PersL processes of MSGO materials. Even more, the coinciding of PersL and PL spectra when excited with 205 nm strongly suggests that the PersL mechanism includes electron movement through CB before reaching the recombination centre, i.e., it is based on thermal detrapping.

4.3.4. Analysis of trap properties

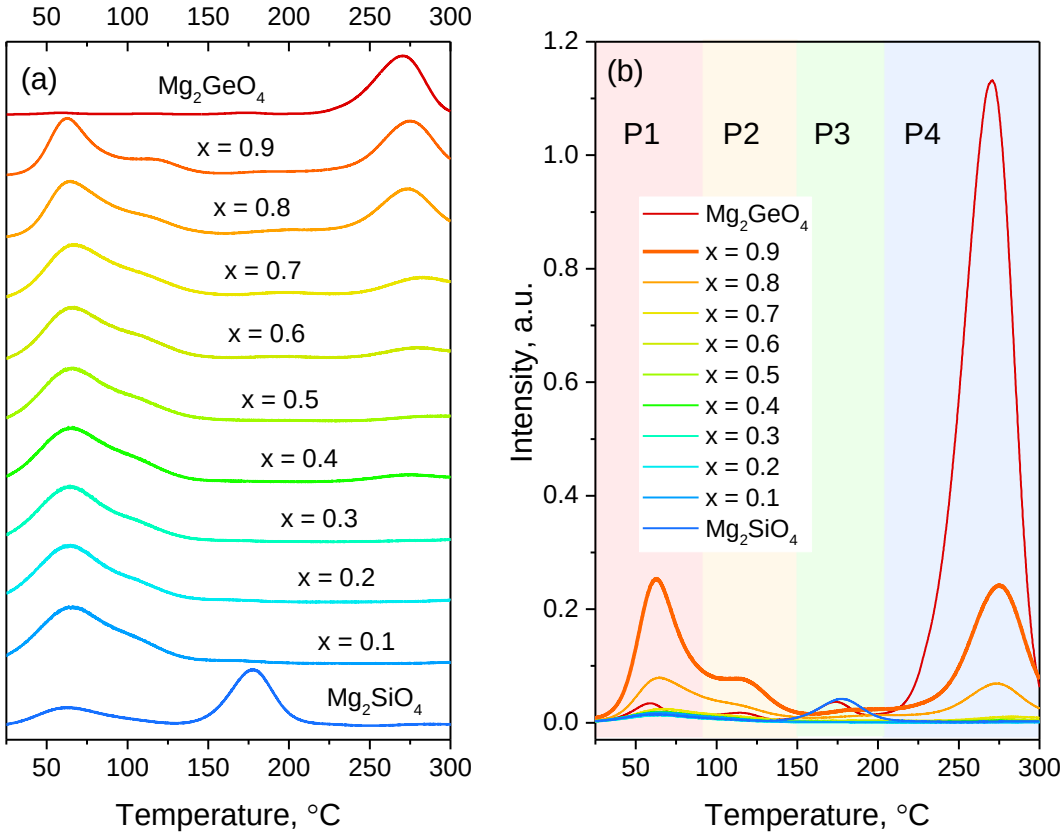

Fig. 4.29. *TSL glow curves of the MSGO samples after irradiation with 263 nm for 30 s.*

To study the trap properties, TSL glow curves of the MSGO samples were measured after irradiation with 263 nm. TSL measurements were carried out by increasing temperature from RT up to 300 °C with a heating rate of 1 °C/s. **Fig. 4.29 (a,b)** depicts the measured glow curves. Multiple semi-overlapping glow peaks were detected throughout all measured temperature range. Obtained glow curves can be approximately divided into four regions - P1 (25 – 90 °C), P2 (90 – 150 °C), P3 (150 – 210 °C) and P4 (210 – 300 °C). As for the intensity of glow peaks, two samples stand out. The Mg_2GeO_4 has the highest overall TSL glow curve intensity. However, its most prominent peak is P4 which represents a deep trap unlikely to play a significant role for RT PersL. On the contrary, MSGO x = 0.9 sample has the highest intensity of relatively shallow traps representing peaks P1 and P2. This result is consistent with PersL decay measurements since RT PersL is expected to be affected mainly by the shallow traps.

In-detail analysis of the trap properties was carried out for the x = 0.9 sample. To determine the nature of the traps and trap depths, the $T_{max} – T_{stop}$ experimental method and IRA were applied. The $T_{max} – T_{stop}$ measurements are shown in **Fig. 4.30. (a)**. T_{stop} values were chosen from 35 – 280 °C with a step of 5 °C. Corresponding $T_{max} – T_{stop}$ plot is provided in **Fig. 4.30. (b)**. As expected from the discussion above, four distinct parts of the plot can be identified. However, only the high-temperature peak corresponding to T_{max} = 280 °C shows apparent features of a discrete trapping state. The patterns of the P1, P2 and P3 parts do not follow the description of either discrete traps or continuous distribution of traps. This is

most likely linked to the significant overlapping of the glow peaks and consequent difficulties in obtaining precise T_{max} values.

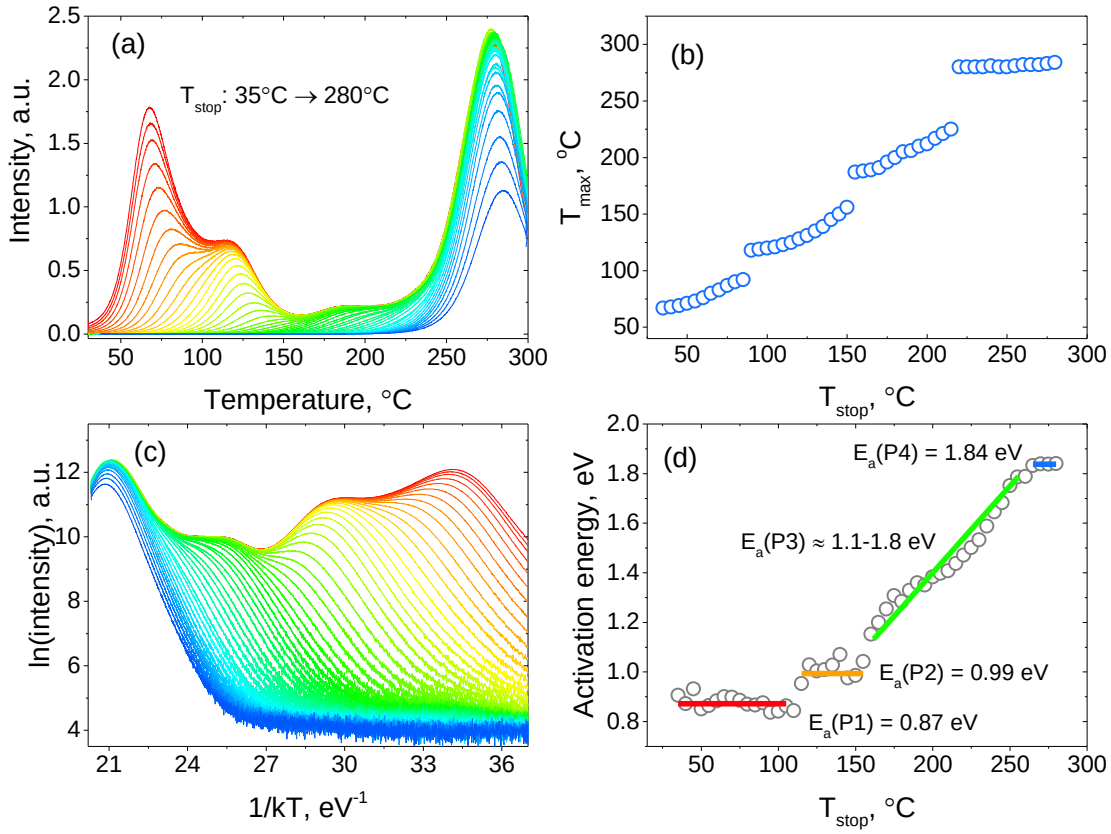

Fig. 4.30. (a) *TSL glow curves of the MSGO x = 0.9 sample measured after preheating to T_{stop} from 35 °C to 280 °C;* ***(b)*** *corresponding $T_{max} – T_{stop}$ plot;* ***(c)*** *IRA of the data obtained from $T_{max} – T_{stop}$ experiment and* ***(d)*** *$E_a – T_{stop}$ plot.*

By applying IRA to the glow curves shown in **Fig. 4.30. (a)** the trap depths E_a were determined. The corresponding IRA plots are presented in **Fig. 4.30. (c),** while obtained E_a values are shown in **Fig. 4.30. (d)**. Here, IRA results not only give information on the E_a values but also clear up the ambiguity of the nature of the traps. The trap depth values corresponding to P1, P2 and P4 fluctuate around constant value for each peak: $E_a(P1)$ = 0.87 ± 0.01 eV, $E_a(P2)$ = 0.99 ± 0.01 eV and $E_a(P4)$ = 1.84 ± 0.01 eV. Thus, P1, P2 and P4 represent discrete trapping sites. Between P2 and P4 lies a relatively low-intensity glow curve region P3. The trap depth value of the P3 continuously increases from around 1.1 eV to 1.8 eV with increased T_{stop}. A broad, plateau type, TSL band corresponding to continuous trap depth distribution has been previously interpreted as related to the thermally assisted tunnelling process [278,279].

EPR spectroscopy analysis of UV-generated paramagnetic centres in the undoped MSGO x = 0.9 sample is shown in **Fig. 4.31.** EPR spectra demonstrate the formation of several paramagnetic centres under UV irradiation. Before the irradiation, only trace impurity signals (marked by the asterisks in **Fig. 4.31.(a)**) could be detected. After the irradiation, a broad signal centred at ≈ 348 mT (g = 2.02) and a better-resolved signal at ≈ 352 mT (g = 1.99) emerges in EPR spectra The g values represent the type of trap centres;

therefore, EPR spectra simulations were carried out for more precise characterisation. The signals were modelled as spin S = 1/2 centres using *Eq. (3.6).* The best fit to the experimental spectrum was achieved by using the SH parameters summarised in *Table 4.4.*

Table 4.4. The fitted SH parameters of the UV-generated paramagnetic centres. Δg_i = 0.001.

Centre	g_1	g_2	g_3
V-type	2.021		
F-type	2.001	1.997	1.995

For the V-type centre, g anisotropy is concealed by the broad lineshape of the signal, which is governed by the relaxation characteristics of the spin system. Based on previous research in similar complex oxide hosts, the identified EPR signals are most likely related to a single trapped hole O^- (V-type centre) and a single trapped electron F^+ centres (F-type centre) [280].

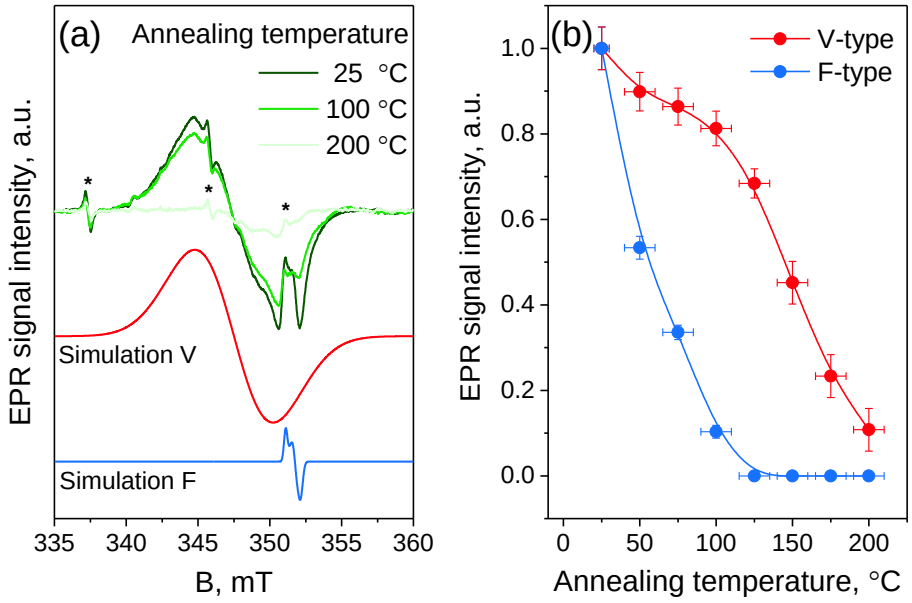

Fig. 4.31. (a) *EPR spectra of undoped MSGO x = 0.9 sample after UV irradiation and subsequent annealing;* ***(b)*** *the decay of paramagnetic centres as a function of sample annealing temperature.*

As evident from **Fig. 4.31.(b)**, the observed paramagnetic centres exhibit distinct annealing decay profiles. The F-type centre decays rapidly in the temperature range up to 100 °C. On the other hand, the annealing process of the V-type centre can be divided into two phases: the first is correlated with the decay of the F-type centre, while the second extends up to 200 °C. This suggests that the V-type centre has multiple complementary electron centres to recombine. The higher stability of the hole traps was observed in the case of MGO samples discussed in the previous chapter as well. The annealing decay profiles correlate with the previously discussed behaviour of TSL glow curves during $T_{max} - T_{stop}$, which suggests that the identified paramagnetic centres play a role in the PersL of the material.

4.3.5. Mechanism of the PersL

Based on the above-discibed results, the primary mechanism of PersL in MSGO samples is proposed in **Fig. 4.32.** The locations of energy levels and traps are schematic and not on the scale. Under 263 nm irradiation, both Mn^{2+}-O^{2-} and Mn^{4+}-O^{2-} CTBs are excited simultaneously. Due to the close distance between the bottom of CB and CTBs, some electrons from CTBs can delocalise to the CB of the host via photoionisation. Electrons are captured and trapped by the electron traps, while holes are trapped by hole traps. Based on EPR analysis, a significant part of traps is associated with oxygen ions and vacancies. When irradiation stops, detrapping of the charge carriers to the CB and VB by phonon assistance occurs. Charge carriers transfer through the host to Mn^{2+}, where recombination occurs, resulting in red broadband PersL.

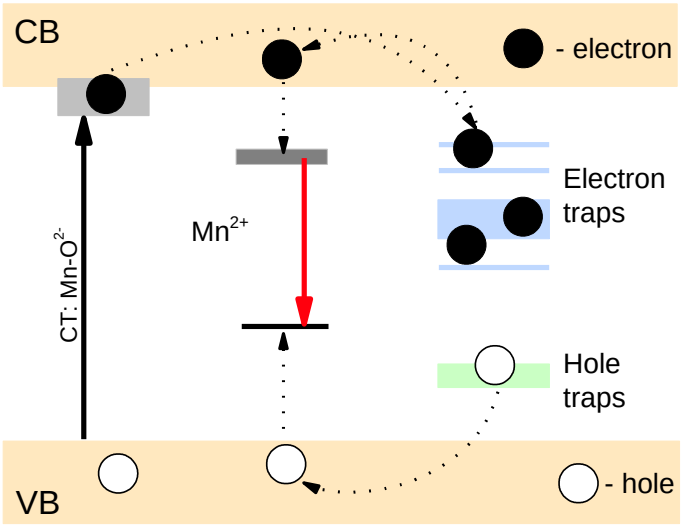

Fig. 4.32. *An energy level scheme of MSGO samples illustrating the luminescence processes and proposed mechanisms.*

4.3.6. Summary

The solid state synthesis method has been successfully applied to synthesise $Mg_2Si_{1-x}Ge_xO_4$ (x = 0.0 – 1.0) solid solutions doped with 0.1 mol% Mn. When excited with 263 nm, all samples except the Mg_2SiO_4 could be characterised by a narrow red Mn^{4+} PL band with a maximum at 660 nm. The origin of this PL emission is $^2E(^2G) \rightarrow {}^4A_2(^4F)$ optical transition. The same 263 nm excitation can induce PersL in all MSGO samples. PersL emission consists of two broad overlapping Mn^{2+} bands. The maxima of the bands are around 637 and 730 nm, corresponding to $^4T_1(^4G) \rightarrow {}^6A_1(^6S)$ optical transitions of Mn^{2+} ions in two non-equivalent Mg^{2+} positions. The simultaneous presence of Mn^{2+} and Mn^{4+} ions in the material and consequent dissimilar spectral features of PL and PersL spectra make the MSGO material desirable for advanced multimode anti-counterfeiting applications.

The best PersL properties were observed for the $Mg_2Si_{0.1}Ge_{0.9}O_4$: Mn sample. When irradiated for 3 min with 263 nm, the sample can be characterised with red afterglow for at least 16 hours at 25 °C temperature.

The TSL analysis revealed a complex system of traps present in the material. Three distinct trap centres and a continuous distribution of closely overlapping trap levels were identified. The activation energy values of distinct traps are 0.87 eV, 0.99 eV, and 1.84 eV, while activation energy values of the distribution are around 1.1 – 1.8 eV. The EPR analysis determined the presence of two distinct paramagnetic centres associated with single trapped electron F^+ centres and single trapped hole O^- centres. Thermal decay of these centres correlates with the behaviour of TSL glow curves during the $T_{max} – T_{stop}$ experiment; thus, they likely play a role in the PersL process.

Optical measurements strongly suggest that PersL in MSGO samples is realised through the classical “trap centre → CB → luminescence centre” model.

THESES

- Synthesis of $MgGeO_3$: Mn^{2+} in reducing atmosphere not only improves the intensity of the afterglow signal by increasing the concentration of the shallow trapping centres, but also leads to the creation of continuous distribution of deep trapping centres in the material.

- Under the influence of UV radiation, deep, oxygen-related trapping centres are formed in $MgGeO_3$: Cr^{3+} material. Charge carriers from the from the trapping centres are transferred mainly by athermal tunnelling to the luminescence centre.

- The photoluminescence spectrum of $Mg_2Si_{1-x}Ge_xO_4$: Mn material, is dominated by characteristic signal of Mn^{4+} while the persistent luminescence spectrum is dominated by that of Mn^{2+}, which is explained by vastly different concentration and excitation efficiency of Mn^{2+} and Mn^{4+} ions in the material.

LIST OF PUBLICATIONS

Publications reflecting the theses

1. **G. Doke**, A. Antuzevics, G. Krieke, A. Kalnina, M. Springis, A. Sarakovskis, UV and X-ray excited red persistent luminescence in Mn^{2+} doped $MgGeO_3$ material synthesized in air and reducing atmosphere, J. Lumin. 234 (2021) 117995. https://doi.org/10.1016/j.jlumin.2021.117995.

2. **G. Doke**, A. Antuzevics, G. Krieke, A. Kalnina, A. Sarakovskis, Novel broadband near-infrared emitting long afterglow phosphor $MgGeO_3$: Cr^{3+}, J. Alloys Compd. 918 (2022) 165768. https://doi.org/10.1016/j.jallcom.2022.165768.

3. **G. Doke**, G. Krieke, A. Antuzevics, A. Sarakovskis, B. Berzina, Optical properties of red-emitting long afterglow phosphor $Mg_2Si_{1-x}Ge_xO_4$: Mn^{2+}/Mn^{4+}, Opt. Mater. (Amst). 137 (2023) 113500. https://doi.org/10.1016/j.optmat.2023.113500.

Other publications

1. A. Antuzevics, **G. Doke**, G. Krieke, P. Rodionovs, D. Nilova, J. Cirulis, A. Fedotovs, U. Rogulis, Shortwave Ultraviolet Persistent Luminescence of $Sr_2MgSi_2O_7$: Pr^{3+}, Materials (Basel). 16 (2023) 1776. https://doi.org/10.3390/ma16051776.
2. G. Krieke, **G. Doke**, A. Antuzevics, I. Pudza, A. Kuzmin, E. Welter, Tuneable persistent luminescence of novel $Mg_3Y_2Ge_3O_{12}$ garnet, J. Alloys Compd. 922 (2022) 166312. https://doi.org/10.1016/j.jallcom.2022.166312.
3. **G. Doke**, A. Kalnina, J. Cipa, M. Springis, A. Sarakovskis, Optical properties of near infrared persistent phosphor $CaZnGe_2O_6$: Cr^{3+}, M^{3+} (M^{3+} = B^{3+}; Al^{3+}; Ga^{3+}), Solid State Commun. 354 (2022) 114894. https://doi.org/10.1016/j.ssc.2022.114894.
4. A. Antuzevics, G. Krieke, **G. Doke**, B. Berzina, The origin of bright cyan persistent luminescence in Ca_2SnO_4:La^{3+}, Materialia. 21 (2022) 101374. https://doi.org/10.1016/j.mtla.2022.101374.
5. A. Supe, S. Spolitis, E. Elsts, R. Murnieks, **G. Doke**, U. Senkans, S. Matsenko, J. Grube, V. Bobrovs, Recent Developments in Cladding-Pumped Doped Fiber Amplifiers for Telecommunications Systems, in: 2020 22nd Int. Conf. Transparent Opt. Networks, IEEE, 2020: pp. 1–6. https://doi.org/10.1109/ICTON51198.2020.9203436.
6. A. Tuomela, V. Pankratov, A. Sarakovskis, **G. Doke**, L. Grinberga, S. Vielhauer, M. Huttula, Oxygen influence on luminescence properties of rare-earth doped $NaLaF_4$, J. Lumin. 179 (2016) 16–20. https://doi.org/10.1016/j.jlumin.2016.06.021.
7. A. Fedotovs, D. Berzins, U. Rogulis, K. Smits, **G. Doke**, A. Medvids, P. Onufrijevs, Angular dependence of recombination luminescence-detected EPR in a ZnO crystal, Phys. Scr. 90 (2015). https://doi.org/10.1088/0031-8949/90/9/094016.
8. A. Sarakovskis, G. Krieke, **G. Doke**, J. Grube, L. Grinberga, M. Springis,

Comprehensive study on different crystal field environments in highly efficient $NaLaF_4:Er^{3+}$ upconversion phosphor, Opt. Mater. (Amst). 39 (2015) 90–96. https://doi.org/10.1016/j.optmat.2014.11.004.

9. J. Grube, A. Sarakovskis, **G. Doke**, M. Springis, Impact of Er^{3+} concentration on luminescence in $NaLaF_4$, Latv. J. Phys. Tech. Sci. 51 (2014) 42–50. https://doi.org/10.2478/lpts-2014-0018.
10. **G. Doke**, A. Sarakovskis, J. Grube, M. Springis, Photoluminescence of neodymium and erbium doped $NaLaF_4$ material, Radiat. Meas. 56 (2013) 27–30. https://doi.org/10.1016/j.radmeas.2013.03.009.
11. U. Rogulis, E. Elsts, J. Jansons, A. Sarakovskis, **G. Doke**, A. Stunda, K. Smits, Cathodoluminescence of oxyfluoride glass-ceramics, Radiat. Meas. 56 (2013) 120–123. https://doi.org/10.1016/j.radmeas.2012.12.020.
12. U. Rogulis, E. Elsts, J. Jansons, A. Sarakovskis, **G. Doke**, A. Stunda, K. Kundzins, Rare earth activated oxyfluoride glasses and glass-ceramics for scintillation applications, IEEE Trans. Nucl. Sci. 59 (2012) 2201–2206. https://doi.org/10.1109/TNS.2012.2212724.
13. A. Sarakovskis, M. Voss, **G. Doke**, D. Jankovica, J. Grube, Synthesis of cubic and hexagonal $NaYF_4:Er^{3+}$, IOP Conf. Ser. Mater. Sci. Eng. 38 (2012) 012038. https://doi.org/10.1088/1757-899X/38/1/012038.
14. A. Sarakovskis, M. Voss, **G. Doke**, J. Grube, M. Springis, Novel synthesis of up-conversion phosphor based on rare-earth doped NaLaF4, IOP Conf. Ser. Mater. Sci. Eng. 23 (2011) 1–5. https://doi.org/10.1088/1757-899X/23/1/012003.
15. A. Sarakovskis, J. Grube, **G. Doke**, M. Springis, Selective excitation of up-conversion luminescence by Yb^{3+}-Er^{3+} energy transfer in glass and crystalline phase of oxyfluoride glass ceramics, Opt. Mater. (Amst). 32 (2010) 832–835. https://doi.org/10.1016/j.optmat.2010.03.003.
16. A. Fedotovs, D. Berzins, A. Sarakovskis, U. Rogulis, **G. Doke**, EPR studies of the oxyfluoride glass ceramics using Mn^{2+} as a paramagnetic probe, IOP Conf. Ser. Mater. Sci. Eng. 15 (2010) 012068. https://doi.org/10.1088/1757-899X/15/1/012068.
17. A. Sarakovskis, J. Grube, **G. Doke**, M. Springis, Excited state absorption and energy-transfer mechanisms of up-conversion luminescence in Er^{3+}-doped oxyfluoride glass ceramics at different temperatures, J. Lumin. 130 (2010) 805–811. https://doi.org/10.1016/j.jlumin.2009.11.037.

LIST OF INTERNATIONAL CONFERENCES AND SUMMER SCHOOLS

1. *The 6th International Conference on the Physics of Optical Materials and Devices and The 5th International Workshop of Persistent and Photostimulable Phosphors 2022*, Belgrade, Serbia, August 29 – September 2, **G. Doke**, A. Antuzevics, G. Krieke, A. Sarakovskis, "Red and NIR persistent luminescence of magnesium germanate based materials", Book of abstracts, p. P-47.
2. *The Seventh International Workshop on Advanced Spectroscopy and Optical Materials 2022*, Gdańsk, Poland, July 10. – 15., 2022, **G. Doke**, G. Krieke, A. Antuzevics, B. Berzina, A. Sarakovskis, "Optical properties of red-emitting long afterglow phosphor $Mg_2Si_{1-x}Ge_xO_4$: Mn material", Book of abstracts, p. 95.
3. *Joint International Conference Functional Materials and Nanotechnologies and Nanotechnology and Innovation in the Baltic Sea Region 2022*, Riga, Latvia, July 3. – 6., **G. Doke**, A. Antuzevics, G. Krieke, A. Kalnina, A. Sarakovskis *"Novel broadband near-infrared emitting long afterglow phosphor $MgGeO_3$: Cr^{3+}"*, Book of abstracts, p. 137.
4. *Developments in Optics and Communications 2022*, Riga, Latvia, April 21. – 22., **G. Doke**, A. Kalnina, M. Springis, A. Sarakovskis "Optical properties of near infrared persistent phosphor $CaZnGe_2O_6$:Cr^{3+}, M^{3+} (M^{3+} = B^{3+}; Al^{3+}; Ga^{3+})", Book of abstracts, p. 56.
5. *Developments in Optics and Communications 2021*, Riga, Latvia, April 14.-16., **G. Doke**, G. Krieke, M. Springis, A. Sarakovskis „Near infrared long persistent luminescence of $CaZnGe_2O_6$:Cr^{3+} material" Book of abstracts, p. 22
6. *Developments in Optics and Communications 2019*, Riga, Latvia, April 11.-12., **G. Doke**, G. Krieke, M. Springis, A. Sarakovskis, „Short-wave infra-red long persistent luminescence of $MgGeO_3$:Yb^{3+} material" Book of abstracts, p. 16.
7. *XVIIth International Krutyn Summer School 2015*, Krutyn, Poland, June 14.-20., **G. Doke**, J. Narvaiss, J. Grube, A. Sarakovskis, M. Springis, „Impact of the presence of hydroxyl groups on mechanisms of up-conversion luminescence of $NaLaF_4$:Er^{3+}" Book of abstracts, p. 35.
8. *Developments in Optics and Communications 2014*, Riga, Latvia, April 10.-12., **G. Doke**, J. Grube, A. Sarakovskis, M. Springis, „The impact of synthesis atmosphere on characteristics of up-conversion luminescence of $NaLaF_4$:Er^{3+}" Book of abstracts, p. 58.
9. *EcoBalt 2013*, Vilnus, Lithuania, October 25.-27., **G. Doke**, M. Voss, J. Grube, A. Sarakovskis, M. Springis, „Synthesis and photoluminescence in $NaLaF_4$:Eu^{3+}material", Book of abstracts, p. 80.
10. *Functional materials and nanotechnologies 2013*, Tartu, Estonia, April 21.-24., **G. Doke**, M. Voss, J. Grube, A. Sarakovskis, M. Springis, „Synthesis and photoluminescence in Eu^{3+} doped $NaLaF_4$ material", Book of abstracts, p. 245.
11. *Developments in Optics and Communications 2013*, Riga, Latvia, April 10.-12., **G. Doke**, J. Grube, A. Sarakovskis, M. Springis, „Impact of synthesis conditions on the properties of up-conversion luminescence in $NaLaF_4$:Er^{3+}" Book of abstracts, p. 58.
12. *LUMDETR 2012, 8th International conference on Luminescenct detectors and Tramsformers of Ionizing Radiotion*, Halle (Saale), Germany, September 10.-14., **G.**

Doke, M. Voss, J. Grube, A. Sarakovskis, and M. Springis, „Photoluminescence and Energy Transfer in Nd^{3+} and Er^{3+} doped $NaLaF_4$ Material", Book of Abstracts, P-Tue-65.

13. *Functional materials and nanotechnologies 2012*, Riga, Latvia, April 17.-20., **G. Doke**, M. Voss, J. Grube, A. Sarakovskis, M. Springis „Photoluminescence and energy transfer in Nd^{3+} and Er^{3+} doped $NaLaF_4$ material", Book of abstracts, p. 323.
14. *Functional materials and Nanotehnologies 2011*, Riga, Latvia, April 5.-8., **G. Doke**, M. Voss, J. Grube, A. Sarakovskis, M. Springis, „Multicolor up-conversion luminescence in rare-earth doped $NaLaF_4$", Book of abstracts, p. 295.
15. *Developments in Optics and Communications 2010*, Riga, Latvia, April 23.-25., **G. Doke**, J. Grube, A. Sarakovskis, M. Springis, „Up-conversion luminescence of erbium doped sodium lanthanum fluoride", Book of abstracts, p. 82.
16. *Functional materials and Nanotehnologies 2010*, Riga, Latvia, March 16.-19., **G. Doke**, A. Sarakovskis, J. Grube, A. Misnovs, M. Springis, „Synthesis and Up-conversion luminiscence in erbium doped $NaLaF_4$", Book of abstracts, p. 212.
17. *Developments in Optics and Communications 2009*, Riga, Latvia, April 24.-26., **G. Doke**, A. Sarakovskis, J. Grube, A. Misnovs, M. Springis, „Energy transfer in Er^{3+} and Yb^{3+} doped silicate glass and glass ceramics", Book of abstracts, p. 80.

ACKNOWLEDGEMENTS

I want to express sincere gratitude to the scientific supervisor Professor Dr. Phys. Anatolijs Sarakovskis, for the support and motivation throughout the years since the beginning of our cooperation in 2008.

I would also like to thank the collective of the Laboratory of Spectroscopy, especially Dr.habil.phys. Maris Springis, Dr. Phys. Jurgis Grube, Professor Dr.habil.phys. Uldis Rogulis, Dr.habil.phys. Baiba Berzina, MSc. Aija Kalnina and MSc. Janis Cipa.

Special thanks to my closest colleagues, collaborators, motivators, listeners, comforters, encouragers, and game night adversaries, PhD Guna Krieke, Dr. Phys. Andris Antuzevics and (soon to be) PhD Meldra Kemere.

And without a doubt, the most immense gratitude to my family for their support and love. Especially to my parents Ilze and Gaidis, the partner in all sorts of crimes Martins and our little hurricanes Raimonds and Ernests.

Institute of Solid State Physics, University of Latvia as the Center of Excellence has received funding from the European Union's Horizon 2020 Framework Programme H2020-WIDESPREAD-01-2016-2017-TeamingPhase2 under grant agreement No. 739508, project CAMART²

Financial support provided from following sources is greatly acknowledged:

- "Strengthening of the Capacity of Doctoral Studies at the University of Latvia within the Framework of the New Doctoral Model", identification No. 8.2.2.0/20/I/006;
- The Latvian Council of Science project "Defect engineering of novel UV-C persistent phosphor materials" grant No. LZP-2021/1-0118;
- The Latvian Council of Science project "Novel persistent luminescent material – red light emitter" grant No. LZP-2019/1–0443;
- Scientific Research Project for Students and Young Researchers Nr. SJZS/2019/8;
- Scientific Research Project for Students and Young Researchers Nr. SJZ/2018/6.

NATIONAL DEVELOPMENT PLAN 2020

EUROPEAN UNION
European Social Fund

INVESTING IN YOUR FUTURE

REFERENCES

[1] P. Kumar, S. Singh, B.K. Gupta, Future prospects of luminescent nanomaterial based security inks: from synthesis to anti-counterfeiting applications, Nanoscale. 8 (2016) 14297–14340. https://doi.org/10.1039/C5NR06965C.

[2] B. Valeur, M.N. Berberan-Santos, A brief history of fluorescence and phosphorescence before the emergence of quantum theory, J. Chem. Educ. 88 (2011) 731–738. https://doi.org/10.1021/ed100182h.

[3] K.V.R. Murthy, H.S. Virk, Luminescence Phenomena: An Introduction, Defect Diffus. Forum. 347 (2013) 1–34. https://doi.org/10.4028/www.scientific.net/DDF.347.1.

[4] K.V.R. Murthy, Luminescence Applications Few Basics, Int. J. Lumin. Appl. 5 (2015) 302–315.

[5] S.W.S. McKeever, Thermoluminescence of solids, 1983.

[6] E.M.J. Weber, A.A. Kaminskii, M.J. Weber, M.J. Weber, M.J. Weber, Phosphor Handbook, CRC Press, 2018. https://doi.org/10.1201/9781315222066.

[7] M. Gaft, R. Reisfeld, G. Panczer, Modern Luminescence Spectroscopy of Minerals and Materials, 2015. https://doi.org/10.1007/978-3-319-24765-6.

[8] C.R. Ronda, Luminescence. From Theory to Applications, Wiley-VCH Verlag GmbH & Co. KGaA, Weinheim, Germany, 2007. https://doi.org/10.1002/9783527621064.

[9] J. Garlick, F. Wilkins, Short period phosphorescence and electron traps, Proc. R. Soc. London. Ser. A. Math. Phys. Sci. 184 (1945) 408–433. https://doi.org/10.1098/rspa.1945.0026.

[10] K. Mahesh, P. Weng, C. Furetta, Thermoluminescence in solids and its applications, Nuclear Technology Publishing, 1989.

[11] J. Włodarczyk, B. Kierdaszuk, Interpretation of Fluorescence Decays using a Power-like Model, Biophys. J. 85 (2003) 589–598. https://doi.org/10.1016/S0006-3495(03)74503-2.

[12] J. Xu, S. Tanabe, Persistent luminescence instead of phosphorescence: History, mechanism, and perspective, J. Lumin. 205 (2019) 581–620. https://doi.org/10.1016/j.jlumin.2018.09.047.

[13] T. Matsuzawa, Y. Aoki, N. Takeuchi, Y. Murayama, A New Long Phosphorescent Phosphor with High Brightness, $SrAl_2O_4$: Eu^{2+}, Dy^{3+}, J. Electrochem. Soc. 143 (1996) 2670–2673. https://doi.org/10.1149/1.1837067.

[14] Y. Jin, Y. Hu, L. Chen, G. Ju, H. Wu, Z. Mu, M. He, F. Xue, Luminescent properties of a green long persistent phosphor Li_2MgGeO_4: Mn^{2+}, Opt. Mater. Express. 6 (2016) 929. https://doi.org/10.1364/OME.6.000929.

[15] Z. Zou, X. Tang, C. Wu, D. Wang, J. Zhang, Z. Ci, S. Du, Y. Wang, How to tune trap properties of persistent phosphor: Photostimulated persistent luminescence of $NaLuGeO_4$: Bi^{3+}, Cr^{3+} tailored by trap engineering, Mater. Res. Bull. 97 (2018) 251–259. https://doi.org/10.1016/j.materresbull.2017.09.011.

[16] D. Kulesza, J. Trojan-Piegza, E. Zych, Lu_2O_3: Tb, Hf storage phosphor, Radiat. Meas. 45 (2010) 490–492. https://doi.org/10.1016/j.radmeas.2009.12.008.

[17] P. Leblans, D. Vandenbroucke, P. Willems, Storage phosphors for medical imaging, Materials (Basel). 4 (2011) 1034–1086. https://doi.org/10.3390/ma4061034.

[18] S. Liu, X. Liu, J. Yuan, J. Bao, Multidimensional Information Encryption and Storage: When the Input Is Light, Research. 2021 (2021) 1–17. https://doi.org/10.34133/2021/7897849.

[19] B. Zones, Luminescence and the Solid State, 2004. https://doi.org/10.1016/S0169-3158(04)80010-0.

[20] H. Young, R. Freedman, University physics with modern physics, 2007.

[21] R. Chen, V. Pagonis, Thermally and Optically Stimulated Luminescence: A Simulation Approach, 2011. https://doi.org/10.1002/9781119993766.

[22] R.C. Ropp, Solid State Chemistry, 2003.

[23] F. Sun, R. Xie, L. Guan, C. Zhang, Cr^{3+} doped $Ca_{14}Zn_6Ga_{10}O_{35}$: A near-infrared long persistent luminescence phosphor, J. Lumin. 180 (2016) 251–257. https://doi.org/10.1016/j.jlumin.2016.08.043.

[24] K. Van den Eeckhout, A.J.J. Bos, D. Poelman, P.F. Smet, Revealing trap depth distributions in persistent phosphors, Phys. Rev. B. 87 (2013) 045126. https://doi.org/10.1103/PhysRevB.87.045126.

[25] W.F. Hornyak, R. Chen, Thermoluminescence and phosphorescence with a continuous distribution of activation energies, J. Lumin. 44 (1989) 73–81. https://doi.org/10.1016/0022-

2313(89)90023-9.
[26] V. Vitola, D. Millers, I. Bite, K. Smits, A. Spustaka, Recent progress in understanding the persistent luminescence in $SrAl_2O_4$: Eu, Dy, Mater. Sci. Technol. (United Kingdom). 35 (2019) 1661–1677. https://doi.org/10.1080/02670836.2019.1649802.
[27] Q. Zhou, L. Dolgov, A.M. Srivastava, L. Zhou, Z. Wang, J. Shi, M.D. Dramićanin, M.G. Brik, M. Wu, Mn^{2+} and Mn^{4+} red phosphors: Synthesis, luminescence and applications in WLEDs. A review, J. Mater. Chem. C. 6 (2018) 2652–2671. https://doi.org/10.1039/c8tc00251g.
[28] J.T. Randall, M.H.F. Wilkins, Phosphorescence and electron traps - I. The study of trap distributions, Proc. R. Soc. London. Ser. A. Math. Phys. Sci. 184 (1945) 365–389. https://doi.org/10.1098/rspa.1945.0024.
[29] J.T. Randall, M.H.F. Wilkins, Phosphorescence and electron traps. II. The interpretation of long-period phosphorescence, Proc. R. Soc. London. Ser. A. 184 (1945) 390–407. https://doi.org/10.1098/rspa.1945.0025.
[30] D. Jia, J. Zhu, B. Wu, Improvement of persistent phosphorescence of $Ca_{0.9}Sr_{0.1}S$: Bi^{3+} by codoping Tm^{3+}, J. Lumin. 91 (2000) 59–65. https://doi.org/10.1016/S0022-2313(00)00208-8.
[31] D.J. Huntley, An explanation of the power-law decay of luminescence, J. Phys. Condens. Matter. 18 (2006) 1359–1365. https://doi.org/10.1088/0953-8984/18/4/020.
[32] G.F.J. Garlick, A.F. Gibson, The Electron Trap Mechanism of Luminescence in Sulphide and Silicate Phosphors, Proc. Phys. Soc. 60 (1948) 574–590. https://doi.org/10.1088/0959-5309/60/6/308.
[33] C.E. May, J.A. Partridge, Thermoluminescent kinetics of alpha-irradiated alkali halides, J. Chem. Phys. 40 (1964) 1401–1409. https://doi.org/10.1063/1.1725324.
[34] Y. Kirsh, R. Chen, Analysis of the blue phosphorescence of x-irradiated albite using a TL-like presentation, Int. J. Radiat. Appl. Instrumentation. Part D. Nucl. Tracks Radiat. Meas. 18 (1991) 37–40. https://doi.org/10.1016/1359-0189(91)90089-Z.
[35] J. Trojan-Piegza, E. Zych, J. Hölsä, J. Niittykoski, Spectroscopic Properties of Persistent Luminescence Phosphors: Lu_2O_3: Tb^{3+}, M^{2+} (M = Ca, Sr, Ba), J. Phys. Chem. C. 113 (2009) 20493–20498. https://doi.org/10.1021/jp906127k.
[36] M. Kitaura, A. Sato, K. Kamada, A. Ohnishi, M. Sasaki, Phosphorescence of Ce-doped $Gd_3Al_2Ga_3O_{12}$ crystals studied using luminescence spectroscopy, J. Appl. Phys. 115 (2014) 083517. https://doi.org/10.1063/1.4867315.
[37] T. Jiang, H. Wang, M. Xing, Y. Fu, Y. Peng, X. Luo, Luminescence decay evaluation of long-afterglow phosphors, Phys. B Condens. Matter. 450 (2014) 94–98. https://doi.org/10.1016/j.physb.2014.04.080.
[38] R. Kohlrausch, Theorie des elektrischen Rückstandes in der Leidener Flasche, Ann. Phys. 167 (1854) 56–82. https://doi.org/10.1002/andp.18541670103.
[39] J. Linnros, N. Lalic, A. Galeckas, V. Grivickas, Analysis of the stretched exponential photoluminescence decay from nanometer-sized silicon crystals in SiO_2, J. Appl. Phys. 86 (1999) 6128–6134. https://doi.org/10.1063/1.371663.
[40] M.N. Berberan-Santos, E.N. Bodunov, B. Valeur, Mathematical functions for the analysis of luminescence decays with underlying distributions 1. Kohlrausch decay function (stretched exponential), Chem. Phys. 315 (2005) 171–182. https://doi.org/10.1016/j.chemphys.2005.04.006.
[41] A. Bos, Thermoluminescence as a Research Tool to Investigate Luminescence Mechanisms, Materials (Basel). 10 (2017) 1357. https://doi.org/10.3390/ma10121357.
[42] Y. Li, M. Gecevicius, J. Qiu, Long persistent phosphors - from fundamentals to applications, Chem. Soc. Rev. 45 (2016) 2090–2136. https://doi.org/10.1039/C5CS00582E.
[43] J. Trojan-Piegza, J. Niittykoski, J. Hölsä, E. Zych, Thermoluminescence and Kinetics of Persistent Luminescence of Vacuum-Sintered Tb^{3+}-Doped and Tb^{3+}, Ca^{2+}-Codoped Lu_2O_3 Materials, Chem. Mater. 20 (2008) 2252–2261. https://doi.org/10.1021/cm703060c.
[44] A. Vedda, M. Fasoli, Tunneling recombinations in scintillators, phosphors, and dosimeters, Radiat. Meas. 118 (2018) 86–97. https://doi.org/10.1016/j.radmeas.2018.08.003.
[45] V. Liepina, D. Millers, K. Smits, A. Zolotarjovs, I. Bite, X-ray excited luminescence of $SrAl_2O_4$: Eu, Dy at low temperatures, J. Phys. Chem. Solids. 115 (2018) 381–385. https://doi.org/10.1016/j.jpcs.2017.12.040.
[46] P. Avouris, T.N. Morgan, A tunneling model for the decay of luminescence in inorganic phosphors: The case of Zn_2SiO_4: Mn, J. Chem. Phys. 74 (1981) 4347–4355.

https://doi.org/10.1063/1.441677.
[47] C. Furetta, Handbook of Thermoluminescence, WORLD SCIENTIFIC, 2009. https://doi.org/10.1142/7187.
[48] S. Wu, Z. Pan, R. Chen, X. Liu, Long Afterglow Phosphorescent Materials, Springer International Publishing, Cham, 2017. https://doi.org/10.1007/978-3-319-60421-3.
[49] H.L. Tuller, S.R. Bishop, Point defects in oxides: Tailoring materials through defect engineering, Annu. Rev. Mater. Res. 41 (2011) 369–398. https://doi.org/10.1146/annurev-matsci-062910-100442.
[50] C.M. Sunta, Unraveling Thermoluminescence, Springer India, New Delhi, 2015. https://doi.org/10.1007/978-81-322-1940-8.
[51] R.D. Shannon, Revised effective ionic radii and systematic studies of interatomic distances in halides and chalcogenides, Acta Crystallogr. Sect. A. 32 (1976) 751–767. https://doi.org/10.1107/S0567739476001551.
[52] A.R. Denton, N.W. Ashcroft, Vegard's law, Phys. Rev. A. 43 (1991) 3161–3164. https://doi.org/10.1103/PhysRevA.43.3161.
[53] Y. Liu, B. Lei, Persistent Luminescent Materials, in: Phosphors, Up Convers. Nano Part. Quantum Dots Their Appl., Springer Singapore, Singapore, 2016: pp. 167–214. https://doi.org/10.1007/978-981-10-1590-8_6.
[54] B. Di Bartolo, J. Collins, Handbook of Applied Solid State Spectroscopy, Springer. (2006).
[55] T.E. Peters, R.G. Pappalardo, R.B. Hunt, Solid State Luminescence, Springer Netherlands, Dordrecht, 1993. https://doi.org/10.1007/978-94-011-1522-3.
[56] B. Di Bartolo, V. Goldberg, D. Pacheco, Luminescence of Inorganic Solids, Springer US, Boston, MA, 1978. https://doi.org/10.1007/978-1-4684-3375-3.
[57] Y. Tanabe, S. Sugano, On the Absorption Spectra of Complex Ions. I, J. Phys. Soc. Japan. 9 (1954) 753–766. https://doi.org/10.1143/JPSJ.9.753.
[58] Y. Tanabe, S. Sugano, On the Absorption Spectra of Complex Ions II, J. Phys. Soc. Japan. 9 (1954) 766–779. https://doi.org/10.1143/JPSJ.9.766.
[59] S. Lakshmi, T. Endo, G. Siva, Electronic (Absorption) Spectra of 3d Transition Metal Complexes, Adv. Asp. Spectrosc. (2012) 3–48. https://doi.org/10.5772/48089.
[60] G.N.A. De Guzman, M.-H. Fang, C.-H. Liang, Z. Bao, S.-F. Hu, R.-S. Liu, Near-infrared phosphors and their full potential: A review on practical applications and future perspectives, J. Lumin. 219 (2020) 116944. https://doi.org/10.1016/j.jlumin.2019.116944.
[61] M. Back, E. Trave, J. Ueda, S. Tanabe, Ratiometric optical thermometer based on dual near-infrared emission in Cr^{3+}-doped bismuth-based gallate host, Chem. Mater. 28 (2016) 8347–8356. https://doi.org/10.1021/acs.chemmater.6b03625.
[62] W. Xie, W. Jiang, R. Zhou, J. Li, J. Ding, H. Ni, Q. Zhang, Q. Tang, J.X. Meng, L. Lin, Disorder-Induced Broadband Near-Infrared Persistent and Photostimulated Luminescence in Mg_2SnO_4: Cr^{3+}, Inorg. Chem. 60 (2021) 2219–2227. https://doi.org/10.1021/acs.inorgchem.0c02941.
[63] S. Ding, H. Guo, P. Feng, Q. Ye, Y. Wang, A New Near-Infrared Long Persistent Luminescence Material with Its Outstanding Persistent Luminescence Performance and Promising Multifunctional Application Prospects, Adv. Opt. Mater. 2000097 (2020) 1–12. https://doi.org/10.1002/adom.202000097.
[64] M.G. Brik, A.M. Srivastava, Critical Review—A Review of the Electronic Structure and Optical Properties of Ions with d3 Electron Configuration (V^{2+}, Cr^{3+}, Mn^{4+}, Fe^{5+}) and Main Related Misconceptions, ECS J. Solid State Sci. Technol. 7 (2018) R3079–R3085. https://doi.org/10.1149/2.0041801jss.
[65] L. Marciniak, K. Kniec, K. Elżbieciak-Piecka, K. Trejgis, J. Stefanska, M. Dramićanin, Luminescence thermometry with transition metal ions. A review, Coord. Chem. Rev. 469 (2022) 214671. https://doi.org/10.1016/j.ccr.2022.214671.
[66] S.K. Singh, Red and near infrared persistent luminescence nano-probes for bioimaging and targeting applications, RSC Adv. 4 (2014) 58674–58698. https://doi.org/10.1039/C4RA08847F.
[67] M.G. Brik, A.M. Srivastava, On the optical properties of the Mn^{4+} ion in solids, J. Lumin. 133 (2013) 69–72. https://doi.org/10.1016/j.jlumin.2011.08.047.
[68] L. Dong, L. Zhang, Y. Jia, B. Shao, W. Lü, S. Zhao, H. You, Site Occupation and Luminescence of Novel Orange-Red $Ca_3M_2Ge_3O_{12}$: Mn^{2+}, Mn^{4+} (M = Al, Ga) Phosphors, ACS Sustain. Chem. Eng. 8 (2020) 3357–3366. https://doi.org/10.1021/acssuschemeng.9b07281.
[69] M. Ayvacıkli, Z. Kotan, E. Ekdal, Y. Karabulut, A. Canimoglu, J. Garcia Guinea, A. Khatab, M.

Henini, N. Can, Solid state synthesis of $SrAl_2O_4$: Mn^{2+} co-doped with Nd^{3+} phosphor and its optical properties, J. Lumin. 144 (2013) 128–132. https://doi.org/10.1016/j.jlumin.2013.06.040.
[70] S. Sugano, Y. Tanabe, H. Kamimura, Multiplets of transition-metal ions in crystals, Pure Appl. Phys. v. 33. 33 (1970) xi, 331.
[71] I. Morad, X. Liu, J. Qiu, Surface crystallized Mn-doped glass-ceramics for tunable luminescence, J. Am. Ceram. Soc. 102 (2019) 5843–5852. https://doi.org/10.1111/jace.16473.
[72] F. Chi, X. Wei, B. Jiang, Y. Chen, C. Duan, M. Yin, Luminescence properties and the thermal quenching mechanism of Mn^{2+} doped Zn_2GeO_4 long persistent phosphors, Dalt. Trans. 47 (2018) 1303–1311. https://doi.org/10.1039/c7dt03906a.
[73] L. Qin, C. Chen, J. Wang, S. Bi, Y. Huang, H.J. Seo, Luminescence properties of red-emitting Mn^{2+}-Activated $Na_2Mg_5Si_{12}O_{30}$ phosphors, Mater. Res. Bull. 118 (2019) 110494. https://doi.org/10.1016/j.materresbull.2019.110494.
[74] K. Van den Eeckhout, P.F. Smet, D. Poelman, Persistent Luminescence in Eu^{2+}-Doped Compounds: A Review, Materials (Basel). 3 (2010) 2536–2566. https://doi.org/10.3390/ma3042536.
[75] K. Van den Eeckhout, D. Poelman, P. Smet, Persistent Luminescence in Non-Eu^{2+}-Doped Compounds: A Review, Materials (Basel). 6 (2013) 2789–2818. https://doi.org/10.3390/ma6072789.
[76] L. Wu, Y. Tang, F. Lu, Z. Yuan, Recent Progress of Near-Infrared Persistent Phosphors in Bio-related and Emerging Applications, Chem. - An Asian J. 16 (2021) 1041–1048. https://doi.org/10.1002/asia.202100108.
[77] X. Wang, Z. Zhang, Z. Tang, Y. Lin, Characterization and properties of a red and orange Y_2O_2S-based long afterglow phosphor, Mater. Chem. Phys. 80 (2003) 1–5. https://doi.org/10.1016/S0254-0584(02)00097-4.
[78] H. Yamamoto, T. Matsuzawa, Mechanism of long phosphorescence of $SrAl_2O_4$: Eu^{2+}, Dy^{3+} and $CaAl_2O_4$:Eu^{2+}, Nd^{3+}, J. Lumin. 72–74 (1997) 287–289. https://doi.org/10.1016/S0022-2313(97)00012-4.
[79] Z. Pan, Y.Y. Lu, F. Liu, Sunlight-activated long-persistent luminescence in the near-infrared from Cr^{3+}-doped zinc gallogermanates, Nat. Mater. 11 (2012) 58–63. https://doi.org/10.1038/nmat3173.
[80] R.E. Rojas-Hernandez, F. Rubio-Marcos, M.Á. Rodriguez, J.F. Fernandez, Long lasting phosphors: $SrAl_2O_4$: Eu, Dy as the most studied material, Renew. Sustain. Energy Rev. 81 (2018) 2759–2770. https://doi.org/10.1016/j.rser.2017.06.081.
[81] D. Poelman, D. Van der Heggen, J. Du, E. Cosaert, P.F. Smet, Persistent phosphors for the future: Fit for the right application, J. Appl. Phys. 128 (2020) 240903. https://doi.org/10.1063/5.0032972.
[82] S. Wu, Y. Li, W. Ding, L. Xu, Y. Ma, L. Zhang, Recent Advances of Persistent Luminescence Nanoparticles in Bioapplications, Nano-Micro Lett. 12 (2020). https://doi.org/10.1007/s40820-020-0404-8.
[83] Q. Lin, Z. Li, Q. Yuan, Recent advances in autofluorescence-free biosensing and bioimaging based on persistent luminescence nanoparticles, Chinese Chem. Lett. 30 (2019) 1547–1556. https://doi.org/10.1016/j.cclet.2019.06.016.
[84] S. Duco, Outdoor Lighting: Physics, Vision and Perception, 2008.
[85] V. Castaing, E. Arroyo, A.I. Becerro, M. Ocaña, G. Lozano, H. Míguez, Persistent luminescent nanoparticles: Challenges and opportunities for a shimmering future, J. Appl. Phys. 130 (2021). https://doi.org/10.1063/5.0053283.
[86] D. Gao, F. Gao, Q. Kuang, X. Zhang, Z. Zhang, Y. Pan, R. Chai, H. Jiao, Zinc Germanate Nanophosphors with Persistent Luminescence for Multi-Mode Imaging of Latent Fingerprints, ACS Appl. Nano Mater. (2022). https://doi.org/10.1021/acsanm.2c02163.
[87] S. Zheng, J. Shi, X. Wang, X. Fu, H. Fan, H. Zhang, Flexible thermosensitive films based on shallow-trap persistent luminescence for high-resolution texture imaging of fingerprints even through latex gloves, J. Mater. Chem. C. 9 (2021) 9619–9626. https://doi.org/10.1039/d1tc01888d.
[88] X. Yu, H. Zhang, J. Yu, Luminescence anti-counterfeiting: From elementary to advanced, Aggregate. 2 (2021) 20–34. https://doi.org/10.1002/agt2.15.
[89] S. Peng, L. Liu, L. Wang, R. Rong, L. Song, W. You, J. Shi, Y. Zhang, A novel self-activated

ultraviolet persistent luminescence material and its anti-counterfeiting application based on intensity and time resolution from persistent luminescence, J. Rare Earths. (2022). https://doi.org/10.1016/j.jre.2022.01.005.
[90] N. Thejo Kalyani, A. Jain, S.J. Dhoble, Persistent phosphors for luminous paints: A review, Luminescence. 37 (2022) 524–542. https://doi.org/10.1002/bio.4203.
[91] J. Arras, S. Bräse, The World Needs New Colors: Cutting Edge Mobility Focusing on Long Persistent Luminescence Materials, ChemPhotoChem. 2 (2018) 55–66. https://doi.org/10.1002/cptc.201700215.
[92] M. Raeiszadeh, B. Adeli, A Critical Review on Ultraviolet Disinfection Systems against COVID-19 Outbreak: Applicability, Validation, and Safety Considerations, ACS Photonics. 7 (2020) 2941–2951. https://doi.org/10.1021/acsphotonics.0c01245.
[93] R. Yin, T. Dai, P. Avci, A.E.S. Jorge, W.C.M.A. De Melo, D. Vecchio, Y.Y. Huang, A. Gupta, M.R. Hamblin, Light based anti-infectives: Ultraviolet C irradiation, photodynamic therapy, blue light, and beyond, Curr. Opin. Pharmacol. 13 (2013) 731–762. https://doi.org/10.1016/j.coph.2013.08.009.
[94] X. Zhou, J. Qiao, Y. Zhao, K. Han, Z. Xia, Multi-responsive deep-ultraviolet emission in praseodymium-doped phosphors for microbial sterilization, Sci. China Mater. (2021) 1–9. https://doi.org/10.1007/s40843-021-1790-1.
[95] S. Yan, Y. Liang, Y. Chen, J. Liu, D. Chen, Z. Pan, Ultraviolet-C persistent luminescence from the Lu_2SiO_5: Pr^{3+} persistent phosphor for solar-blind optical tagging, Dalt. Trans. 50 (2021) 8457–8466. https://doi.org/10.1039/D1DT00791B.
[96] W. Yuan, T. Tan, H. Wu, R. Pang, S. Zhang, L. Jiang, D. Li, Z. Wu, C. Li, H. Zhang, Intense UV long persistent luminescence benefiting from the coexistence of Pr^{3+}/Pr^{4+} in a praseodymium-doped $BaLu_2Al_2Ga_2SiO_{12}$ phosphor, J. Mater. Chem. C. 9 (2021) 5206–5216. https://doi.org/10.1039/D1TC00584G.
[97] P. Xiong, M. Peng, Recent advances in ultraviolet persistent phosphors, Opt. Mater. X. 2 (2019) 100022. https://doi.org/10.1016/j.omx.2019.100022.
[98] J. Du, D. Poelman, Identifying Near-Infrared Persistent Luminescence in Cr^{3+}-Doped Magnesium Gallogermanates Featuring Afterglow Emission at Extremely Low Temperature, Adv. Opt. Mater. 8 (2020) 1901848. https://doi.org/10.1002/adom.201901848.
[99] J. Du, D. Poelman, H. Lin, Modulating trap distribution of persistent phosphors upon simple microwave-assisted solid-state reactions, Chem. Eng. J. 431 (2022) 133706. https://doi.org/10.1016/j.cej.2021.133706.
[100] S. Liu, H. Cai, S. Zhang, Z. Song, Q. Liu, An emerging NIR super-long persistent phosphor and its applications, Mater. Today Chem. 24 (2022) 100806. https://doi.org/10.1016/j.mtchem.2022.100806.
[101] S. Korte, E. Lindfeld, J. Thomas, Flicker Reduction of AC LEDs by Mn^{2+} Doped Apatite Phosphor, 7 (2018) 21–26. https://doi.org/10.1149/2.0141803jss.
[102] H. Lin, J. Xu, Q. Huang, B. Wang, H. Chen, Z. Lin, Y. Wang, Bandgap Tailoring via Si Doping in Inverse-Garnet $Mg_3Y_2Ge_3O_{12}$: Ce^{3+} Persistent Phosphor Potentially Applicable in AC-LED, ACS Appl. Mater. Interfaces. 7 (2015) 21835–21843. https://doi.org/10.1021/acsami.5b06071.
[103] S. Kitsinelis, L. Arexis-boisson, Y. Zhang, G. Zissis, LED Flicker: A Drawback or an Opportunity, 2013 (2013) 63–66.
[104] Q. Su, C. Li, J. Wang, Some interesting phenomena in the study of rare earth long lasting phosphors, Opt. Mater. (Amst). 36 (2014) 1894–1900. https://doi.org/10.1016/j.optmat.2014.06.032.
[105] D. Van Der Heggen, J.J. Joos, P.F. Smet, Importance of Evaluating the Intensity Dependency of the Quantum E ffi ciency: Impact on LEDs and Persistent Phosphors, (2018). https://doi.org/10.1021/acsphotonics.8b00979.
[106] W. Yuan, R. Pang, S. Wang, T. Tan, C. Li, C. Wang, H. Zhang, Enhanced blue-light excited cyan-emitting persistent luminescence of $BaLu_2Al_2Ga_2SiO_{12}$: Ce^{3+}, Bi^{3+} phosphors for AC-LEDs via defect modulation, Light Sci. Appl. 11 (2022) 184. https://doi.org/10.1038/s41377-022-00868-8.
[107] R. Naik, S.C. Prashantha, H. Nagabhushana, Effect of Li^+ codoping on structural and luminescent properties of Mg_2SiO_4: RE^{3+} (RE = Eu, Tb) nanophosphors for displays and eccrine latent fingerprint detection, Opt. Mater. (Amst). 72 (2017) 295–304. https://doi.org/10.1016/j.optmat.2017.06.021.

[108] X. Zhao, F. Liu, Z. Yu, X. Li, C. Wang, F. Chen, X. Wang, Sunlight stimulated solar-blind ultraviolet phosphor, Phys. Rev. Res. 4 (2022) L012028. https://doi.org/10.1103/PhysRevResearch.4.L012028.
[109] D. Chávez, C.R. Garcia, J. Oliva, L.A. Diaz-Torres, A review of phosphorescent and fluorescent phosphors for fingerprint detection, Ceram. Int. 47 (2021) 10–41. https://doi.org/10.1016/j.ceramint.2020.08.259.
[110] V. Sharma, A. Das, V. Kumar, V. Kumar, K. Verma, H.C. Swart, Combustion synthesis and characterization of blue long lasting phosphor $CaAl_2O_4$: Eu^{2+}, Dy^{3+} and its novel application in latent fingerprint and lip mark detection, Phys. B Condens. Matter. 535 (2018) 149–156. https://doi.org/10.1016/j.physb.2017.07.019.
[111] M. Zhang, F. Li, S. Jiang, Y.C. Lin, F. Chen, X. Zhao, Y. Shen, $CaAl_2O_4$: Eu^{2+}, Nd^{3+} anti-corrosive coating and its afterglow - Catalytic process, Opt. Mater. (Amst). 116 (2021) 111049. https://doi.org/10.1016/j.optmat.2021.111049.
[112] F. Kang, G. Sun, P. Boutinaud, H. Wu, F.X. Ma, J. Lu, J. Gan, H. Bian, F. Gao, S. Xiao, Recent advances and prospects of persistent luminescent materials as inner secondary self-luminous light source for photocatalytic applications, Chem. Eng. J. 403 (2021) 126099. https://doi.org/10.1016/j.cej.2020.126099.
[113] D. Gao, J. Gao, F. Gao, Q. Kuang, Y. Pan, Y. Chen, Z. Pan, Quintuple-mode dynamic anti-counterfeiting using multi-mode persistent phosphors, J. Mater. Chem. C. 9 (2021) 16634–16644. https://doi.org/10.1039/d1tc04568g.
[114] B. Wang, Z. Wang, P. Mao, Y. Wang, A multi-color persistent luminescent phosphor b-$NaYF_4$: RE^{3+} (RE = Sm, Tb, Dy, Pr) for dynamic anti-counterfeiting, (2022). https://doi.org/10.1039/d2ra01425d.
[115] N. Katumo, K. Li, B.S. Richards, I.A. Howard, Dual-color dynamic anti-counterfeiting labels with persistent emission after visible excitation allowing smartphone authentication, Sci. Rep. 12 (2022) 2100. https://doi.org/10.1038/s41598-022-05885-6.
[116] P. Liu, Y. Zhang, B. Li, L. Han, Y. Xu, Trap depth engineering in $MgGa_2O_4$: Bi^{3+} for muticolor dynamic anti-counterfeiting, encryption and optical temperature sensing applications, Chem. Eng. J. 437 (2022) 135389. https://doi.org/10.1016/j.cej.2022.135389.
[117] E. Hemmer, A. Benayas, F. Légaré, F. Vetrone, Exploiting the biological windows: Current perspectives on fluorescent bioprobes emitting above 1000 nm, Nanoscale Horizons. 1 (2016) 168–184. https://doi.org/10.1039/c5nh00073d.
[118] X. Sun, L. Song, N. Liu, J. Shi, Y. Zhang, Chromium-Doped Zinc Gallate Near-Infrared Persistent Luminescence Nanoparticles in Autofluorescence-Free Biosensing and Bioimaging: A Review, ACS Appl. Nano Mater. 4 (2021) 6497–6514. https://doi.org/10.1021/acsanm.1c01115.
[119] L. Liang, N. Chen, Y. Jia, Q. Ma, J. Wang, Q. Yuan, W. Tan, Recent progress in engineering near-infrared persistent luminescence nanoprobes for time-resolved biosensing/bioimaging, Nano Res. 12 (2019) 1279–1292. https://doi.org/10.1007/s12274-019-2343-6.
[120] D.L. Fritzen, L. Giordano, L.C.V. Rodrigues, J.H.S.K. Monteiro, Opportunities for persistent luminescent nanoparticles in luminescence imaging of biological systems and photodynamic therapy, Nanomaterials. 10 (2020) 1–38. https://doi.org/10.3390/nano10102015.
[121] J. Trojan-Piegza, E. Zych, Afterglow luminescence of Lu_2O_3: Eu ceramics synthesized at different atmospheres, J. Phys. Chem. C. 114 (2010) 4215–4220. https://doi.org/10.1021/jp910126r.
[122] P. Liu, Y. Liu, C. Cui, L. Wang, J. Qiao, P. Huang, Q. Shi, Y. Tian, H. Jiang, J. Jiang, Enhanced luminescence and afterglow by heat-treatment in reducing atmosphere to synthesize the $Gd_3Al_2Ga_3O_{12}$: Ce^{3+} persistent phosphor for AC-LEDs, J. Alloys Compd. 731 (2018) 389–396. https://doi.org/10.1016/j.jallcom.2017.10.037.
[123] M. Iwasaki, D.N. Kim, K. Tanaka, T. Murata, K. Morinaga, Red phosphorescence properties of Mn ions in $MgO–GeO_2$ compounds, Sci. Technol. Adv. Mater. 4 (2003) 137–142. https://doi.org/10.1016/S1468-6996(03)00025-1.
[124] F. Xue, Y. Hu, L. Chen, H. Wu, G. Ju, T. Wang, L. Yang, A novel rare-earth free red long-persistent phosphor: Mg_2GeO_4: Mn^{4+}, Ceram. Int. 43 (2017) 15141–15145. https://doi.org/10.1016/j.ceramint.2017.08.044.
[125] D. Zhou, Z. Song, H. Zhou, Q. Liu, Enhanced persistent luminescence via Si4+ co-doping in $Y_3Al_2Ga_3O_{12}$: Ce^{3+}, Yb^{3+}, B^{3+}, J. Lumin. 222 (2020) 117190. https://doi.org/10.1016/j.jlumin.2020.117190.

[126] L.L. Noto, S.S. Pitale, M.A. Gusowki, J.J. Terblans, O.M. Ntwaeaborwa, H.C. Swart, Afterglow enhancement with In^{3+} codoping in $CaTiO_3$: Pr^{3+} red phosphor, Powder Technol. 237 (2013) 141–146. https://doi.org/10.1016/j.powtec.2013.01.029.

[127] D. Jia, W.M. Yen, Enhanced VK^{3+} center afterglow in $MgAl_2O_4$ by doping with Ce^{3+}, J. Lumin. 101 (2003) 115–121. https://doi.org/10.1016/S0022-2313(02)00394-0.

[128] M. Fasoli, A. Vedda, M. Nikl, C. Jiang, B.P. Uberuaga, D.A. Andersson, K.J. McClellan, C.R. Stanek, Band-gap engineering for removing shallow traps in rare-earth $Lu_3Al_5O_{12}$ garnet scintillators using Ga^{3+} doping, Phys. Rev. B - Condens. Matter Mater. Phys. 84 (2011) 1–4. https://doi.org/10.1103/PhysRevB.84.081102.

[129] I.I. Vrubel, R.G. Polozkov, I.A. Shelykh, V.M. Khanin, P.A. Rodnyi, C.R. Ronda, Bandgap Engineering in Yttrium-Aluminum Garnet with Ga Doping, Cryst. Growth Des. 17 (2017) 1863–1869. https://doi.org/10.1021/acs.cgd.6b01822.

[130] J. Xu, S. Tanabe, A.D. Sontakke, J. Ueda, Near-infrared multi-wavelengths long persistent luminescence of Nd3+ion through persistent energy transfer in Ce^{3+}, Cr^{3+} co-doped $Y_3Al_2Ga_3O_{12}$for the first and second bio-imaging windows, Appl. Phys. Lett. 107 (2015). https://doi.org/10.1063/1.4929495.

[131] L. Yuan, Y. Jin, D. Zhu, Z. Mou, G. Xie, Y. Hu, Ni^{2+} -Doped Yttrium Aluminum Gallium Garnet Phosphors: Bandgap Engineering for Broad-Band Wavelength-Tunable Shortwave-Infrared Long-Persistent Luminescence and Photochromism, ACS Sustain. Chem. Eng. 8 (2020) 6543–6550. https://doi.org/10.1021/acssuschemeng.0c01377.

[132] J. Xu, J. Ueda, S. Tanabe, Design of deep-red persistent phosphors of $Gd_3Al_{5-x}Ga_xO_{12}$: Cr^{3+} transparent ceramics sensitized by Eu^{3+} as an electron trap using conduction band engineering, Opt. Mater. Express. 5 (2015) 963. https://doi.org/10.1364/ome.5.000963.

[133] V. Castaing, A.D. Sontakke, J. Xu, A.J. Ferná Ndez-Carrió, C. Cile Genevois, S. Tanabe, M. Allix, B. Viana, Persistent energy transfer in ZGO: Cr^{3+}, Yb^{3+}: a new strategy to design nano glass-ceramics featuring deep red and near infrared persistent luminescence, Phys. Chem. Chem. Phys. 21 (1945). https://doi.org/10.1039/c9cp02927c.

[134] J. Liu, Y. Liang, S. Yan, D. Chen, S. Miao, W. Wang, Narrowband ultraviolet-B persistent luminescence from $(Y,Gd)_3Ga_5O_{12}$: Bi^{3+} phosphors for optical tagging application, Dalt. Trans. 50 (2021) 15413–15421. https://doi.org/10.1039/d1dt02568f.

[135] J. Xu, D. Chen, Y. Yu, W. Zhu, J. Zhou, Y. Wang, Cr^{3+} :$SrGa_{12}O_{19}$: A broadband near-infrared long-persistent phosphor, Chem. - An Asian J. 9 (2014) 1020–1025. https://doi.org/10.1002/asia.201400009.

[136] R.K. Gartia, N. Chandrasekhar, Physical basis of persistent luminescence: The case of europium doped $Ca_{1-x}Sr_xS$, J. Alloys Compd. 683 (2016) 157–163. https://doi.org/10.1016/j.jallcom.2016.05.087.

[137] Y. Zhuang, J. Ueda, S. Tanabe, Multi-color persistent luminescence in transparent glass ceramics containing spinel nano-crystals with Mn^{2+} ions, Appl. Phys. Lett. 105 (2014) 3–7. https://doi.org/10.1063/1.4901749.

[138] J. Kong, W. Zheng, Y. Liu, R. Li, E. Ma, H. Zhu, X. Chen, Persistent luminescence from Eu^{3+} in SnO_2 nanoparticles, Nanoscale. 7 (2015) 11048–11054. https://doi.org/10.1039/c5nr01961c.

[139] L. Pihlgren, T. Laihinen, L.C.V. Rodrigues, S. Carlson, K.O. Eskola, A. Kotlov, M. Lastusaari, T. Soukka, H.F. Brito, J. Hölsä, On the mechanism of persistent up-conversion luminescence in the ZrO_2: Yb^{3+}, Er^{3+} nanomaterials, Opt. Mater. (Amst). 36 (2014) 1698–1704. https://doi.org/10.1016/j.optmat.2014.01.027.

[140] X. Ding, Z. Li, Y. Shi, H.T. Cao, Luminescence properties of $Ca_2Sn_2Al_2O_9$: Mn as a long afterglow and field-emission displays material with high yellow color purity, J. Alloys Compd. 824 (2020) 153931. https://doi.org/10.1016/j.jallcom.2020.153931.

[141] X.J. Wang, D. Jia, W.M. Yen, Mn^{2+} activated green, yellow, and red long persistent phosphors, J. Lumin. 102–103 (2003) 34–37. https://doi.org/10.1016/S0022-2313(02)00541-0.

[142] Y. Gong, X. Xu, W. Zeng, C. Wu, Y. Wang, Ce^{3+}, Mn^{2+} Co-doped Red–light Long–Lasting Phosphor: $BaMg_2Si_2O_7$ Through Energy Transfer, Phys. Procedia. 29 (2012) 86–90. https://doi.org/10.1016/j.phpro.2012.03.696.

[143] J. Kuang, Y. Liu, B. Lei, Effect of RE^{3+} as a co-dopant in long-lasting phosphorescence $CdSiO_3$: Mn^{2+} (RE=Y, La, Gd, Lu), J. Lumin. 118 (2006) 33–38. https://doi.org/10.1016/j.jlumin.2005.06.005.

[144] Y. Jin, Y. Hu, Y. Fu, G. Ju, Z. Mu, R. Chen, J. Lin, Z. Wang, Preparation, Design, and

Characterization of the Novel Long Persistent Phosphors: Na_2ZnGeO_4 and Na_2ZnGeO_4: Mn^{2+}, J. Am. Ceram. Soc. 98 (2015) 1555–1561. https://doi.org/10.1111/jace.13503.

[145] Y. Katayama, T. Kayumi, J. Ueda, S. Tanabe, Enhanced persistent red luminescence in Mn^{2+}-doped (Mg,Zn)GeO_3 by electron trap and conduction band engineering, Opt. Mater. (Amst). 79 (2018) 147–151. https://doi.org/10.1016/j.optmat.2018.03.033.

[146] L. Jiang, Luminescent properties of Zn_2GeO_4: Mn^{2+} phosphors synthesized by using different manganese sources, J. Photochem. Photobiol. A Chem. 377 (2019) 282–285. https://doi.org/10.1016/j.jphotochem.2019.04.005.

[147] G. Doke, A. Antuzevics, G. Krieke, A. Kalnina, M. Springis, A. Sarakovskis, UV and X-ray excited red persistent luminescence in Mn^{2+} doped $MgGeO_3$ material synthesized in air and reducing atmosphere, J. Lumin. 234 (2021) 117995. https://doi.org/10.1016/j.jlumin.2021.117995.

[148] G. Che, C. Liu, X. Li, Z. Xu, Y. Liu, H. Wang, Luminescence properties of a new Mn^{2+}-activated red long-afterglow phosphor, J. Phys. Chem. Solids. 69 (2008) 2091–2095. https://doi.org/10.1016/j.jpcs.2008.03.006.

[149] A. Luchechko, Y. Zhydachevskyy, S. Ubizskii, O. Kravets, A.I. Popov, U. Rogulis, E. Elsts, E. Bulur, A. Suchocki, Afterglow, TL and OSL properties of Mn^{2+}-doped $ZnGa_2O_4$ phosphor, Sci. Rep. 9 (2019) 9544. https://doi.org/10.1038/s41598-019-45869-7.

[150] W. Zheng, H. Wu, G. Ju, Z. Mo, H. Dong, Y. Hu, Y. Jin, Crystal field modulation-control, bandgap engineering and shallow/deep traps tailoring-guided design of a color-tunable long-persistent phosphor (Ca,Sr)Ga_4O_7: Mn^{2+}, Bi^{3+}, Dalt. Trans. 48 (2019) 253–265. https://doi.org/10.1039/c8dt03566k.

[151] J. Wang, Q. Su, S. Wang, A novel red long lasting phosphorescent (LLP) material β-$Zn_3(PO_4)_2$: Mn^{2+}, Sm^{3+}, Mater. Res. Bull. 40 (2005) 590–598. https://doi.org/10.1016/j.materresbull.2005.01.011.

[152] Y.H. Song, H.F. Zou, S.C. Gan, Y.F. Deng, G.Y. Hong, J. Meng, Phase conversion and spectral properties of long lasting phosphor $Zn_3(PO_4)_2$: Mn^{2+}, Ga^{3+}, J. Mater. Sci. 42 (2007) 4899–4904. https://doi.org/10.1007/s10853-006-0598-2.

[153] A. Bessière, A. Lecointre, R.A. Benhamou, E. Suard, G. Wallez, B. Viana, How to induce red persistent luminescence in biocompatible $Ca_3(PO_4)_2$, J. Mater. Chem. C. 1 (2013) 1252–1259. https://doi.org/10.1039/C2TC00138A.

[154] Z. Wang, L. Feng, J. Zhang, Z. Ci, Z. Zhang, Y. Wang, Nonequivalent Substitution and Charge-Induced Emitter-Migration Design of Tuning Spectral and Duration Properties of $NaCa_2GeO_4F$: Mn^{2+} Persistent Luminescent Phosphor, Inorg. Chem. 55 (2016) 7988–7996. https://doi.org/10.1021/acs.inorgchem.6b01048.

[155] J. Xu, N.J. Cherepy, J. Ueda, S. Tanabe, Red persistent luminescence in rare earth-free AlN: Mn^{2+} phosphor, Mater. Lett. 206 (2017) 175–177. https://doi.org/10.1016/j.matlet.2017.07.015.

[156] Y. Zhuang, Y. Katayama, J. Ueda, S. Tanabe, A brief review on red to near-infrared persistent luminescence in transition-metal-activated phosphors, Opt. Mater. (Amst). 36 (2014) 1907–1912. https://doi.org/10.1016/j.optmat.2014.05.035.

[157] Y. Zhang, R. Huang, H. Li, D. Hou, Z.Z. Lin, J. Song, Y. Guo, H. Lin, C. Song, Z.Z. Lin, J. Robertson, Germanium substitution endowing Cr^{3+}-doped zinc aluminate phosphors with bright and super-long near-infrared persistent luminescence, Acta Mater. 155 (2018) 214–221. https://doi.org/10.1016/j.actamat.2018.06.020.

[158] F. Sun, R. Xie, L. Guan, C. Zhang, The near-infrared long-persistent phosphorescence of Cr^{3+}-activated non-gallate phosphor, Mater. Lett. 164 (2016) 39–43. https://doi.org/10.1016/j.matlet.2015.10.111.

[159] Y. Katayama, H. Kobayashi, S. Tanabe, Deep-red persistent luminescence in Cr^{3+}-doped $LaAlO_3$ perovskite phosphor for in vivo imaging, Appl. Phys. Express. 8 (2015) 1–4. https://doi.org/10.7567/APEX.8.012102.

[160] S. Wang, J. Cai, R. Pang, H. Wu, Y. Luo, T. Tan, W. Yuan, L. Jiang, C. Li, H. Zhang, Synthesis and luminescence properties of a broadband near-infrared emitting non-gallate persistent luminescence $Mg_{1.4}Zn_{0.6}SnO_4$: Cr^{3+} phosphor, Dalt. Trans. 50 (2021) 5666–5675. https://doi.org/10.1039/d1dt00452b.

[161] Y. Li, S. Zhou, Y. Li, K. Sharafudeen, Z. Ma, G. Dong, M. Peng, J. Qiu, Long persistent and photo-stimulated luminescence in Cr^{3+}-doped Zn-Ga-Sn-O phosphors for deep and reproducible tissue imaging, J. Mater. Chem. C. 2 (2014) 2657–2663. https://doi.org/10.1039/c4tc00014e.

[162] Y. Li, Y. Li, R. Chen, K. Sharafudeen, S. Zhou, M. Gecevicius, H. Wang, G. Dong, Y. Wu, X. Qin, J. Qiu, Tailoring of the trap distribution and crystal field in Cr^{3+}-doped non-gallate phosphors with near-infrared long-persistence phosphorescence, NPG Asia Mater. 7 (2015) e180-11. https://doi.org/10.1038/am.2015.38.

[163] F. Liu, W. Yan, Y.-J. Chuang, Z. Zhen, J. Xie, Z. Pan, Photostimulated near-infrared persistent luminescence as a new optical read-out from Cr^{3+}-doped $LiGa_5O_8$, Sci. Rep. 3 (2013) 1554. https://doi.org/10.1038/srep01554.

[164] Y. Zhuang, J. Ueda, S. Tanabe, Enhancement of Red Persistent Luminescence in Cr^{3+}-Doped $ZnGa_2O_4$ Phosphors by Bi_2O_3 Codoping, Appl. Phys. Express. 6 (2013) 052602. https://doi.org/10.7567/APEX.6.052602.

[165] A. Mondal, J. Manam, Structural and Luminescent Properties of Si^{4+} Co-Doped $MgGa_2O_4$: Cr^{3+} Near Infra-Red Long Lasting Phosphor, ECS J. Solid State Sci. Technol. 6 (2017) R88–R95. https://doi.org/10.1149/2.0021708jss.

[166] Y. Zhan, Y. Jin, H. Wu, L. Yuan, G. Ju, Y. Lv, Y. Hu, Cr^{3+}-doped $Mg_4Ga_4Ge_3O_{16}$ near-infrared phosphor membrane for optical information storage and recording, J. Alloys Compd. 777 (2019) 991–1000. https://doi.org/10.1016/j.jallcom.2018.11.065.

[167] D. Dai, Z. Wang, C. Liu, X. Li, L. Zhang, Z. Xing, Z. Yang, P. Li, Lithium Substitution Endowing Cr^{3+}-Doped Gallium Germanate Phosphors with Super-Broad-Band and Long Persistent Near-Infrared Luminescence, ACS Appl. Electron. Mater. 1 (2019) 2551–2559. https://doi.org/10.1021/acsaelm.9b00563.

[168] X. Zhou, G. Ju, T. Dai, Y. Li, H. Wu, Y. Jin, Y. Hu, $Li_5Zn_8Ga_5Ge_9O_{36}$: Cr^{3+}, Ti^{4+}: A Long Persistent Phosphor Excited in a Wide Spectral Region from UV to Red Light for Reproducible Imaging through Biological Tissue, Chem. – An Asian J. 14 (2019) 1506–1514. https://doi.org/10.1002/asia.201900158.

[169] Y. Jin, Y. Hu, L. Yuan, L. Chen, H. Wu, G. Ju, H. Duan, Z. Mu, Multifunctional near-infrared emitting Cr^{3+}-doped $Mg_4Ga_8Ge_2O_{20}$ particles with long persistent and photostimulated persistent luminescence, and photochromic properties, J. Mater. Chem. C. 4 (2016) 6614–6625. https://doi.org/10.1039/C6TC01640E.

[170] H. Lin, G. Bai, T. Yu, M.K. Tsang, Q. Zhang, J. Hao, Site Occupancy and Near-Infrared Luminescence in $Ca_3Ga_2Ge_3O_{12}$: Cr^{3+} Persistent Phosphor, Adv. Opt. Mater. 5 (2017) 1–9. https://doi.org/10.1002/adom.201700227.

[171] X. Meng, P. Li, K. Qiu, H. Suo, X. Zhao, J. Cui, D. Wang, J. Zhao, Z. Yang, Z. Wang, Photoluminescence and afterglow tuning in ultra-broadband near-infrared $Mg_3Y_2Ge_3O_{12}$: Cr^{3+} phosphor via cation substitution, Optik (Stuttg). 230 (2021) 166305. https://doi.org/10.1016/j.ijleo.2021.166305.

[172] X. Meng, Z. Wang, S. Wu, K. Qiu, Z. Wang, X. Li, D. Wang, J. Zhao, Z. Yang, P. Li, Improving the luminescence and afterglow properties of $Mg_3Y_2Ge_3O_{12}$: Cr^{3+} by co-doping Bi^{3+}, Ceram. Int. 46 (2020) 18903–18910. https://doi.org/10.1016/j.ceramint.2020.04.213.

[173] R. Kang, J. Nie, X. Dou, S. Zhang, G. Ju, L. Chen, Y. Hu, Y. Li, Tunable NIR long persistent luminescence and discovery of trap-distribution-dependent excitation enhancement in transition metal doped weak-crystal-field $CaZnGe_2O_6$, J. Alloys Compd. 735 (2018) 692–699. https://doi.org/10.1016/j.jallcom.2017.11.182.

[174] F. Xue, Y. Hu, L. Fan, G. Ju, Y. Lv, Y. Li, Cr^{3+}-activated $Li_5Zn_8Al_5Ge_9O_{36}$: A near-infrared long-afterglow phosphor, J. Am. Ceram. Soc. 100 (2017) 3070–3079. https://doi.org/10.1111/jace.14874.

[175] G. Doke, A. Antuzevics, G. Krieke, A. Kalnina, A. Sarakovskis, Novel broadband near-infrared emitting long afterglow phosphor $MgGeO_3$: Cr^{3+}, J. Alloys Compd. 918 (2022) 165768. https://doi.org/10.1016/j.jallcom.2022.165768.

[176] D.-D. Xu, Z.-C. Qiu, Q. Zhang, L.-J. Huang, Y.-Y. Ye, L.-W. Cao, J.-X. Meng, Sr_2MgWO_6: Cr^{3+} phosphors with effective near-infrared fluorescence and long-lasting phosphorescence, J. Alloys Compd. 781 (2019) 473–478. https://doi.org/10.1016/j.jallcom.2018.12.094.

[177] D. Xu, X. Wu, Q. Zhang, W. Li, T. Wang, L. Cao, J. Meng, Fluorescence property of novel near-infrared phosphor Ca_2MgWO_6: Cr^{3+}, J. Alloys Compd. 731 (2018) 156–161. https://doi.org/10.1016/j.jallcom.2017.10.036.

[178] T. Yamanaka, M. Hirano, Y. Takeuchi, A high temperature transition in $MgGeO_3$ from clinopyroxene C2c type to orthopyroxene Pbca type, Am. Mineral. 70 (1985) 365–374.

[179] Y. Katayama, T. Kayumi, J. Ueda, P. Dorenbos, B. Viana, S. Tanabe, The role of Ln^{3+} (Ln = Eu,

Yb) in persistent red luminescence in $MgGeO_3$: Mn^{2+}, J. Mater. Chem. C. 5 (2017) 8893–8900. https://doi.org/10.1039/C7TC03151C.

[180] Y. Katayama, J. Ueda, S. Tanabe, Effect of Bi_2O_3 doping on persistent luminescence of $MgGeO_3$: Mn^{2+} phosphor, Opt. Mater. Express. 4 (2014) 613. https://doi.org/10.1364/OME.4.000613.

[181] X. Peng, Z. Tang, Y. Luo, L. Yang, M. He, X. Ye, Z. Zheng, X. Cui, C. Xia, F. Wang, Visual color modulation and luminescence mechanism studies on Mn/Eu co-doped Zn–Mg-Ge-O long afterglow system, Ceram. Int. 46 (2020) 14005–14018. https://doi.org/10.1016/j.ceramint.2020.02.200.

[182] C. Xia, M. Zhou, M. He, L. Yang, M. Liu, P. Zhou, H. Chen, F. Wang, Experimental and theoretical studies on luminescent mechanisms and different visual color of the mixed system composed of $MgGeO_3$: Mn, Eu and Zn_2GeO_4: Mn, Int. J. Mod. Phys. B. 34 (2020) 1–16. https://doi.org/10.1142/S0217979220502161.

[183] D. Ding, S. Li, H. Xu, L. Zhu, S. Meng, J. Liu, Q. Lin, S.W. Leung, W. Sun, Y. Li, H. Chen, X-ray-Activated Simultaneous Near-Infrared and Short-Wave Infrared Persistent Luminescence Imaging for Long-Term Tracking of Drug Delivery, ACS Appl. Mater. Interfaces. 13 (2021) 16166–16172. https://doi.org/10.1021/acsami.1c02372.

[184] S. Zheng, J. Shi, X. Fu, C. Wang, X. Sun, C. Chen, Y. Zhuang, X. Zou, Y. Li, H. Zhang, X-ray recharged long afterglow luminescent nanoparticles $MgGeO_3$: Mn^{2+}, Yb^{3+} ,Li^+ in the first and second biological windows for long-term bioimaging, Nanoscale. 12 (2020) 14037–14046. https://doi.org/10.1039/C9NR10622G.

[185] Y.-J. Liang, F. Liu, Y.-F. Chen, X.-J. Wang, K.-N. Sun, Z. Pan, New function of the Yb^{3+} ion as an efficient emitter of persistent luminescence in the short-wave infrared, Light Sci. Appl. 5 (2016) e16124–e16124. https://doi.org/10.1038/lsa.2016.124.

[186] Y. Liang, F. Liu, Y. Chen, X. Wang, K. Sun, Z. Pan, Red/near-infrared/short-wave infrared multi-band persistent luminescence in Pr^{3+}-doped persistent phosphors, Dalt. Trans. 46 (2017) 11149–11153. https://doi.org/10.1039/C7DT02271A.

[187] X. Huang, X. Zhao, Z. Yu, Y. Liu, A. Wang, X. Wang, F. Liu, Effect of electron-transfer quenching on the photoluminescence of Pr^{3+} in $MgXO_3$ (X = Ge, Si), Opt. Mater. Express. 10 (2020) 1163. https://doi.org/10.1364/ome.389599.

[188] H. Song, M. Zhang, R. Cui, W. Huang, C. Deng, Structure, morphology and optical characterization of Sm^{3+}-doped $MgGeO_3$ nanocrystals for warm white light emitting devices, Mod. Phys. Lett. B. 36 (2022) 2000. https://doi.org/10.1142/S0217984921506223.

[189] A. Awad, A.F. Koster Van Groos, S. Guggenheim, Forsteritic olivine: Effect of crystallographic direction on dissolution kinetics, Geochim. Cosmochim. Acta. 64 (2000) 1765–1772. https://doi.org/10.1016/S0016-7037(99)00442-1.

[190] H.M. Yang, J.X. Shi, H. Bin Liang, M.L. Gong, A novel red phosphor Mg_2GeO_4 doped with Eu^{3+} for PDP applications, Mater. Sci. Eng. B Solid-State Mater. Adv. Technol. 127 (2006) 276–279. https://doi.org/10.1016/j.mseb.2005.10.014.

[191] H.M. Yang, Z. Wang, M.L. Gong, H. Liang, Luminescence properties of a novel red emitting phosphor, Mg_2GeO_4: Sm^{3+}, J. Alloys Compd. 488 (2009) 331–333. https://doi.org/10.1016/j.jallcom.2009.08.123.

[192] H.M. Yang, J. Shi, M.L. Gong, H. Liang, The UV and VUV luminescence properties of the phosphor Mg_2GeO_4: Tb^{3+}, Mater. Lett. 64 (2010) 1034–1036. https://doi.org/10.1016/j.matlet.2010.02.001.

[193] H. Cai, S. Liu, Z. Song, Q. Liu, Tuning luminescence from NIR-I to NIR-II in Cr^{3+}-doped olivine phosphors for nondestructive analysis, J. Mater. Chem. C. 9 (2021) 5469–5477. https://doi.org/10.1039/d1tc00521a.

[194] H. Cai, H. Chen, H. Zhou, J. Zhao, Z. Song, Q.L. Liu, Controlling Cr^{3+}/Cr^{4+} concentration in single-phase host toward tailored super-broad near-infrared luminescence for multifunctional applications, Mater. Today Chem. 22 (2021) 100555. https://doi.org/10.1016/j.mtchem.2021.100555.

[195] R. Naik, S.C. Prashantha, H. Nagabhushana, S.C. Sharma, B.M. Nagabhushana, H.P. Nagaswarupa, H.B. Premkumar, Low temperature synthesis and photoluminescence properties of red emitting Mg_2SiO_4: Eu^{3+} nanophosphor for near UV light emitting diodes, Sensors Actuators, B Chem. 195 (2014) 140–149. https://doi.org/10.1016/j.snb.2014.01.018.

[196] M. Ghahari, A.R. Naeimi, Electrophoretic deposition and an investigation of co-dopants effect

on luminescence property of Mg_2SiO_4: Eu^{3+} phosphors, J. Rare Earths. 35 (2017) 1171–1179. https://doi.org/10.1016/j.jre.2017.05.013.
[197] H. Yang, J. Shi, M. Gong, K.W. Cheah, Synthesis and photoluminescence of Eu^{3+}- or Tb^{3+}-doped Mg_2SiO_4 nanoparticles prepared by a combined novel approach, J. Lumin. 118 (2006) 257–264. https://doi.org/10.1016/j.jlumin.2005.09.005.
[198] K. Mondal, P. Kumari, J. Manam, Influence of doping and annealing temperature on the structural and optical properties of Mg_2SiO_4: Eu^{3+} synthesized by combustion method, Curr. Appl. Phys. 16 (2016) 707–719. https://doi.org/10.1016/j.cap.2016.04.001.
[199] R. Naik, S.C. Prashantha, H. Nagabhushana, H.P. Nagaswarupa, K.S. Anantharaju, S.C. Sharma, B.M. Nagabhushana, H.B. Premkumar, K.M. Girish, Mg_2SiO_4: Tb^{3+} nanophosphor: Auto ignition route and near UV excited photoluminescence properties for WLEDs, J. Alloys Compd. 617 (2014) 69–75. https://doi.org/10.1016/j.jallcom.2014.07.100.
[200] Y. Zhao, S. Qiao, Y. Wang, X. Wu, D. Poelman, P.D. Townsend, Luminescence sites and spectra of metal doped microwave synthesized Mg_2SiO_4: Tb, J. Lumin. 228 (2020) 5–11. https://doi.org/10.1016/j.jlumin.2020.117635.
[201] M. Ghahari, K. Mostafavi, Synthesis of Mg_2SiO_4: Dy^{3+} nanoparticles by hydrothermal method and investigation of their thermo and photo luminescence properties, Mater. Res. Bull. 77 (2016) 48–53. https://doi.org/10.1016/j.materresbull.2016.01.026.
[202] R. Naik, S.C. Prashantha, H. Nagabhushana, S.C. Sharma, H.P. Nagaswarupa, K.S. Anantharaju, D.M. Jnaneshwara, K.M. Girish, Tunable white light emissive Mg_2SiO_4: Dy^{3+} nanophosphor: Its photoluminescence, Judd-Ofelt and photocatalytic studies, Dye. Pigment. 127 (2016) 25–36. https://doi.org/10.1016/j.dyepig.2015.12.014.
[203] R. Naik, S.C. Prashantha, H. Nagabhushana, S.C. Sharma, H.P. Nagaswarupa, K.S. Anantharaju, B.M. Nagabhushana, H.B. Premkumar, K.M. Girish, A single phase, red emissive Mg_2SiO_4: Sm^{3+} nanophosphor prepared via rapid propellant combustion route, Spectrochim. Acta - Part A Mol. Biomol. Spectrosc. 140 (2015) 516–523. https://doi.org/10.1016/j.saa.2015.01.011.
[204] T.J. Glynn, G.F. Imbusch, G. Walker, Luminescence from Cr^{3+} centres in forsterite (Mg_2SiO_4), J. Lumin. 48–49 (1991) 541–544. https://doi.org/10.1016/0022-2313(91)90188-2.
[205] R. Naik, S.C. Prashantha, H. Nagabhushana, S.C. Sharma, H.P. Nagaswarupa, K.M. Girish, Effect of fuel on auto ignition route, photoluminescence and photometric studies of tunable red emitting Mg_2SiO_4: Cr^{3+} nanophosphors for solid state lighting applications, J. Alloys Compd. 682 (2016) 815–824. https://doi.org/10.1016/j.jallcom.2016.05.037.
[206] G. Walker, B. Kamaluddin, T.J. Glynn, R. Sherlock, Luminescence of Ni^{2+} centers in forsterite (Mg_2SiO_4), J. Lumin. 60–61 (1994) 123–126. https://doi.org/10.1016/0022-2313(94)90110-4.
[207] T.C. Brunold, H.U. Güdel, A.A. Kaminskii, Optical spectroscopy of V^{4+} doped crystals of Mg_2SiO_4 and Ca_2GeO_4, Chem. Phys. Lett. 271 (1997) 327–334. https://doi.org/10.1016/S0009-2614(97)00466-1.
[208] P.N. Chiara, S.S. Pedro, A. López, I.C.S. Carvalho, L.P. Sosman, Photoluminescence of the manganese ions on $Mg_2Si_2O_6$-Mg_2SiO_4 compounds, J. Lumin. 182 (2017) 39–44. https://doi.org/10.1016/j.jlumin.2016.09.062.
[209] L. Lin, M. Yin, C. Shi, W. Zhang, B. You, Synthesis and luminescence properties of red phosphors: Mn^{2+} doped $MgSiO_3$ and Mg_2SiO_4 prepared by sol-gel method, J. Rare Earths. 24 (2006) 104–107. https://doi.org/10.1016/S1002-0721(07)60334-2.
[210] L. Lin, M. Yin, C. Shi, W. Zhang, Luminescence properties of a new red long-lasting phosphor: Mg_2SiO_4: Dy^{3+}, Mn^{2+}, J. Alloys Compd. 455 (2008) 327–330. https://doi.org/10.1016/j.jallcom.2007.01.059.
[211] G. Doke, G. Krieke, A. Antuzevics, A. Sarakovskis, B. Berzina, Optical properties of red-emitting long afterglow phosphor $Mg_2Si_{1-x}Ge_xO_4$: Mn^{2+}/Mn^{4+}, Opt. Mater. (Amst). 137 (2023) 113500. https://doi.org/10.1016/j.optmat.2023.113500.
[212] A. Bishnoi, S. Kumar, N. Joshi, Wide-Angle X-ray Diffraction (WXRD), in: Microsc. Methods Nanomater. Charact., Elsevier, 2017: pp. 313–337. https://doi.org/10.1016/B978-0-323-46141-2.00009-2.
[213] N. Doebelin, R. Kleeberg, Profex: A graphical user interface for the Rietveld refinement program BGMN, J. Appl. Crystallogr. 48 (2015) 1573–1580. https://doi.org/10.1107/S1600576715014685.
[214] T. Ahmad Para, S. Kanti Sarkar, Challenges in Rietveld Refinement and Structure Visualization in Ceramics, in: Adv. Ceram. Mater., IntechOpen, 2021: p. 13.

https://doi.org/10.5772/intechopen.96065.
[215] K. Momma, F. Izumi, VESTA 3 for three-dimensional visualization of crystal, volumetric and morphology data, J. Appl. Crystallogr. 44 (2011) 1272–1276. https://doi.org/10.1107/S0021889811038970.
[216] A.J.J. Bos, Theory of thermoluminescence, Radiat. Meas. 41 (2006) S45–S56. https://doi.org/10.1016/j.radmeas.2007.01.003.
[217] V. Pagonis, G. Kitis, Prevalence of first-order kinetics in thermoluminescence materials: An explanation based on multiple competition processes, Phys. Status Solidi Basic Res. 249 (2012) 1590–1601. https://doi.org/10.1002/pssb.201248082.
[218] S.W.S. McKeever, On the analysis of complex thermoluminescence. Glow-curves: Resolution into individual peaks, Phys. Status Solidi. 62 (1980) 331–340. https://doi.org/10.1002/pssa.2210620139.
[219] Y.S. Horowitz, D. Satinger, D. Yossian, M.E. Brandan, A.E. Buenfil, I. Gamboa-deBuen, M. Rodriguez-Villafuerte, C.G. Ruiz, Ionisation density effects in the thermoluminescence of TLD-100: Computerised T(m)-T(stop) glow curve analysis, Radiat. Prot. Dosimetry. 84 (1999) 239–242. https://doi.org/10.1093/oxfordjournals.rpd.a032727.
[220] A. Akin, E. Ekdal, Y. Tuncer Arslanlar, M. Ayvaci, T. Karali, N. Can, Thermally stimulated luminescence glow curve structure of β-irradiated CaB_4O_7: Dy, Luminescence. 30 (2015) 830–834. https://doi.org/10.1002/bio.2826.
[221] N. Chandrasekhar, K.B. Singh, R.K. Gartia, On the Urbach's formula for evaluation of electron trapping parameter: The case of persistent luminescent materials, J. Rare Earths. 35 (2017) 733–738. https://doi.org/10.1016/S1002-0721(17)60970-0.
[222] R. Chen, V. Pagonis, J.L. Lawless, Evaluated thermoluminescence trapping parameters - What do they really mean?, Radiat. Meas. 91 (2016) 21–27. https://doi.org/10.1016/j.radmeas.2016.04.006.
[223] M.S. Rasheedy, Method of Hoogenstraaten as a tool for obtaining the trap parameters of general-order thermoluminescence glow peaks, Radiat. Eff. Defects Solids. 160 (2005) 383–390. https://doi.org/10.1080/10420150500459999.
[224] Y. Zhang, R. Huang, Z. Lin, H. Li, D. Hou, J. Song, S. Lin, C. Song, H. Lin, Z. Lin, Positive effect of codoping Yb^{3+} on the super-long persistent luminescence of Cr^{3+}-doped zinc aluminum germanate, Ceram. Int. 44 (2018) 17377–17382. https://doi.org/10.1016/j.ceramint.2018.06.202.
[225] V. Pagonis, G. Kitis, C. Furetta, Numerical and practical exercises in thermoluminescence, 2006. https://doi.org/10.1007/0-387-30090-2.
[226] B.J. Hales, Electron Paramagnetic Resonance (EPR) Spectroscopy, in: Encycl. Inorg. Bioinorg. Chem., John Wiley & Sons, Ltd, Chichester, UK, 2011: pp. 1–16. https://doi.org/10.1002/9781119951438.eibc0310.
[227] C.F. De, O. Graeff, J. Niklas, R. Pandey, T. Biskup, Structure-Function Relationship of Organic Semiconductors: Detailed Insights From Time-Resolved EPR Spectroscopy, Front. Chem. 7 (2019). https://doi.org/10.3389/fchem.2019.00010.
[228] M. Mostafanejad, Basics of the spin Hamiltonian formalism, Int. J. Quantum Chem. 114 (2014) 1495–1512. https://doi.org/10.1002/qua.24721.
[229] A. Abragam, B. Bleaney, Electron Paramagnetic Resonance of Transition Ions, in: Electron Paramagn. Reson. Transit. Ions, Clarendon Press, 1970. https://doi.org/10.1017/CBO9781107415324.004.
[230] J. Telser, EPR interactions-zero-field splittings, EMagRes. 6 (2017) 207–234. https://doi.org/10.1002/9780470034590.emrstm1501.
[231] M. Bennati, EPR interactions-hyperfne couplings, EMagRes. (2017). https://doi.org/10.1002/9780470034590.emrstm1503.
[232] S. Stoll, A. Schweiger, EasySpin, a comprehensive software package for spectral simulation and analysis in EPR, J. Magn. Reson. 178 (2006) 42–55.
[233] Y. Cong, B. Li, S. Yue, L. Zhang, W. Li, X. Wang, Enhanced Red Phosphorescence in $MgGeO_3$: Mn^{2+} by Addition of Yb^{3+} Ions, J. Electrochem. Soc. 156 (2009) H272. https://doi.org/10.1149/1.3077570.
[234] F. Liu, Y. Liang, Y. Chen, Z. Pan, Divalent Nickel-Activated Gallate-Based Persistent Phosphors in the Short-Wave Infrared, Adv. Opt. Mater. 4 (2016) 562–566. https://doi.org/10.1002/adom.201500656.

[235] A. Lecointre, A. Bessière, K.R. Priolkar, D. Gourier, G. Wallez, B. Viana, Role of manganese in red long-lasting phosphorescence of manganese-doped diopside for in vivo imaging, Mater. Res. Bull. 48 (2013) 1898–1905. https://doi.org/10.1016/j.materresbull.2013.01.017.

[236] F. Xue, Y. Hu, L. Fan, X. Wang, G. Ju, M. He, Y. Lv, Photoluminescence and afterglow of Mn^{2+} doped lithium zinc silicate, J. Lumin. 183 (2017) 68–72. https://doi.org/10.1016/j.jlumin.2016.11.026.

[237] J. Wang, S. Wang, Q. Su, Synthesis, photoluminescence and thermostimulated-luminescence properties of novel red long-lasting phosphorescent materials β-$Zn_3(PO_4)_2$: Mn^{2+}, M^{3+} (M = Al and Ga), J. Mater. Chem. 14 (2004) 2569–2574. https://doi.org/10.1039/b401685h.

[238] M. Kemere, A. Antuzevics, P. Rodionovs, U. Rogulis, A. Sarakovskis, Photoluminescence and electron paramagnetic resonance studies of Mn^{2+} doped $CaAl_4O_7$, Opt. Mater. (Amst). 127 (2022) 112352. https://doi.org/10.1016/j.optmat.2022.112352.

[239] T. Xie, H. Guo, J. Zhang, Y. He, H. Lin, G. Chen, Z. Zheng, Effects of oxygen vacancies on luminescent properties of green long-lasting phosphorescent (LLP) material α-$Zn_3(PO_4)_2$: Mn^{2+}, K^+, J. Lumin. 170 (2016) 150–154. https://doi.org/10.1016/j.jlumin.2015.10.044.

[240] L. Lin, C. Shi, Z. Wang, W. Zhang, M. Yin, A kinetics model of red long-lasting phosphorescence in $MgSiO_3$: Eu^{2+}, Dy^{3+}, Mn^{2+}, J. Alloys Compd. 466 (2008) 546–550. https://doi.org/10.1016/j.jallcom.2007.11.093.

[241] X. Li, X. Tang, Z. Wang, Z. Zou, J. Zhang, Z. Ci, Y. Wang, Structural, persistent luminescence properties and trap characteristics of an orthosilicate phosphor: $LiGaSiO_4$: Mn^{2+}, J. Alloys Compd. 721 (2017) 512–519. https://doi.org/10.1016/j.jallcom.2017.06.054.

[242] J. Yang, Y. Liu, D. Yan, H. Zhu, C. Liu, C. Xu, L. Ma, X. Wang, A vacuum-annealing strategy for improving near-infrared super long persistent luminescence in Cr^{3+} doped zinc gallogermanate nanoparticles for bio-imaging, Dalt. Trans. 45 (2016) 1364–1372. https://doi.org/10.1039/c5dt03875h.

[243] X. Xu, Y. Wang, Y. Gong, W. Zeng, Y. Li, Effect of oxygen vacancies on the red phosphorescence of Sr_2SnO_4: Sm^{3+} phosphor, Opt. Express. 18 (2010) 16989. https://doi.org/10.1364/oe.18.016989.

[244] K. Brylew, W. Drozdowski, A.J. Wojtowicz, K. Kamada, A. Yoshikawa, Studies of low temperature thermoluminescence of GAGG: Ce and LuAG: Pr scintillator crystals using the T_{max}-T_{stop} method, J. Lumin. 154 (2014) 452–457. https://doi.org/10.1016/j.jlumin.2014.05.035.

[245] M. Isik, N.M. Gasanly, L.G. Gasanova, A.Z. Mahammadov, Thermoluminescence study in $Cu_3Ga_5S_9$ single crystals: Application of heating rate and T_m–T_{stop} methods, J. Lumin. 199 (2018) 334–338. https://doi.org/10.1016/j.jlumin.2018.03.076.

[246] W. Drozdowski, K. Brylew, S.M. Kaczmarek, D. Piwowarska, Y. Nakai, T. Tsuboi, W. Huang, Studies on shallow traps in $Li_2B_4O_7$: Eu, Mn, Radiat. Meas. 63 (2014) 26–31. https://doi.org/10.1016/j.radmeas.2014.02.017.

[247] G. Doke, A. Antuzevics, G. Krieke, A. Kalnina, M. Springis, A. Sarakovskis, UV and X-ray excited red persistent luminescence in Mn^{2+} doped $MgGeO_3$ material synthesized in air and reducing atmosphere, J. Lumin. 234 (2021) 117995. https://doi.org/10.1016/j.jlumin.2021.117995.

[248] C.M. Sunta, W.E.F. Ayta, J.F.D. Chubaci, S. Watanabe, A critical look at the kinetic models of thermoluminescence - I. First order kinetics, J. Phys. D. Appl. Phys. 34 (2001). https://doi.org/10.1088/0022-3727/38/1/016.

[249] A.S. Marfunin, Spectroscopy, luminescence and radiation centers in minerals, Springer Science & Business Media, 2012.

[250] V. Laguta, M. Buryi, P. Arhipov, O. Sidletskiy, O. Laguta, M.G. Brik, M. Nikl, Oxygen-vacancy donor-electron center in $Y_3Al_5O_{12}$ garnet crystals: Electron paramagnetic resonance and dielectric spectroscopy study, Phys. Rev. B. 101 (2020) 24106. https://doi.org/10.1103/PhysRevB.101.024106.

[251] T. Si, Q. Zhu, J. Xiahou, X. Sun, J.G. Li, Regulating Mn^{2+}/Mn^{4+} Activators in $ZnGa_2O_4$ via Mg^{2+}/Ge^{4+} Doping to Generate Multimode Luminescence for Advanced Anti-Counterfeiting, ACS Appl. Electron. Mater. 3 (2021) 2005–2016. https://doi.org/10.1021/acsaelm.0c01121.

[252] E. Hill, B.J. Wood, J.D. Blundy, The effect of Ca-Tschermaks component on trace element partitioning between clinopyroxene and silicate melt, Lithos. 53 (2000) 203–215. https://doi.org/10.1016/S0024-4937(00)00025-6.

[253] K.P. O'Donnell, B. Henderson, D. O'Connell, M.O. Henry, Axial Cr^{3+} centres in MgO: EPR and

fluorescence studies, J. Phys. C Solid State Phys. 10 (1977) 3877–3884. https://doi.org/10.1088/0022-3719/10/19/021.
[254] S.K. Misra, Multifrequency Electron Paramagnetic Resonance: Theory and Applications, Wiley, 2011. https://doi.org/10.1002/9783527633531.
[255] N. Li, P. Zhang, Z. Wang, Z. Wei, Z. Jiang, Y. Shang, M. Zhang, Q. Qiang, L. Zhao, W. Chen, Novel UV and X-ray irradiated white-emitting persistent luminescence and traps distribution of $Ca_5Ga_6O_{14}$: Pr^{3+} phosphors, J. Alloys Compd. 858 (2021) 1–9. https://doi.org/10.1016/j.jallcom.2020.157719.
[256] X. Ding, Q. Zhang, Multi spectral responsive near infrared-II broad emission material and its LED device and imaging research, Ceram. Int. 47 (2021) 34851–34859. https://doi.org/10.1016/j.ceramint.2021.09.026.
[257] K. Qiu, H. Zhang, T. Yuan, J. Shi, S. Wu, X. Meng, J. Liu, P. Li, Z. Yang, Z. Wang, Design and improve of the near-infrared phosphor by adjusting the energy levels or constructing new defects, Spectrochim. Acta - Part A Mol. Biomol. Spectrosc. 219 (2019) 401–410. https://doi.org/10.1016/j.saa.2019.04.069.
[258] N. Mao, S. Liu, Z. Song, Y. Yu, Q. Liu, A broadband near-infrared phosphor $Ca_3Y_2Ge_3O_{12}$: Cr^{3+} with garnet structure, J. Alloys Compd. 863 (2021) 2–8. https://doi.org/10.1016/j.jallcom.2021.158699.
[259] A.P. Vink, M.A. de Bruin, S. Roke, P.S. Peijzel, A. Meijerink, Luminescence of Exchange Coupled Pairs of Transition Metal Ions, J. Electrochem. Soc. 148 (2001) E313. https://doi.org/10.1149/1.1375169.
[260] T.R. Rajalekshmi, T. Dixit, M.S.R. Rao, K. Sethupathi, Pair-Emission-Induced Near-Infrared Lasing from Ceramic Ga :$LaCrO_3$ Microcrystals at Room Temperature, Phys. Status Solidi - Rapid Res. Lett. 15 (2021) 1–5. https://doi.org/10.1002/pssr.202000519.
[261] Y. Su, L. Yuan, H. Liu, G. Xiong, H. Wu, Y. Hu, X. Cheng, Y. Jin, Multi-site occupation of Cr^{3+} toward developing broadband near-infrared phosphors, Ceram. Int. 47 (2021) 23558–23563. https://doi.org/10.1016/j.ceramint.2021.05.073.
[262] D. Dai, Z. Wang, Z. Xing, X. Li, C. Liu, L. Zhang, Z. Yang, P. Li, Broad band emission near-infrared material $Mg_3Ga_2GeO_8$: Cr^{3+}: Substitution of Ga-In, structural modification, luminescence property and application for high efficiency LED, J. Alloys Compd. 806 (2019) 926–938. https://doi.org/10.1016/j.jallcom.2019.07.166.
[263] L. Zhang, S. Zhang, Z. Hao, X. Zhang, G.H. Pan, Y. Luo, H. Wu, J. Zhang, A high efficiency broad-band near-infrared $Ca_2LuZr_2Al_3O_{12}$: Cr^{3+} garnet phosphor for blue LED chips, J. Mater. Chem. C. 6 (2018) 4967–4976. https://doi.org/10.1039/c8tc01216d.
[264] P. Bolek, D. Kulesza, A.J.J. Bos, E. Zych, The role of Ti in charge carriers trapping in the red-emitting Lu_2O_3: Pr, Ti phosphor, J. Lumin. 194 (2018) 641–648. https://doi.org/10.1016/j.jlumin.2017.09.028.
[265] A.E. Hughes, B. Henderson, Color Centers in Simple Oxides, in: Point Defects in Solids, 1972: pp. 381–490. https://doi.org/10.1007/978-1-4684-2970-1_7.
[266] C. Gionco, S. Livraghi, S. Maurelli, E. Giamello, S. Tosoni, C. Di Valentin, G. Pacchioni, Al- and Ga-Doped TiO_2, ZrO_2, and HfO_2: The Nature of O2p Trapped Holes from a Combined Electron Paramagnetic Resonance (EPR) and Density Functional Theory (DFT) Study, Chem. Mater. 27 (2015) 3936–3945. https://doi.org/10.1021/acs.chemmater.5b00800.
[267] M. Nikl, V. V. Laguta, A. Vedda, Complex oxide scintillators: Material defects and scintillation performance, Phys. Status Solidi Basic Res. 245 (2008) 1701–1722. https://doi.org/10.1002/pssb.200844039.
[268] V. V. Laguta, M. Nikl, A. Vedda, E. Mihokova, J. Rosa, K. Blazek, Hole and electron traps in the $YAlO_3$ single crystal scintillator, Phys. Rev. B - Condens. Matter Mater. Phys. 80 (2009) 1–10. https://doi.org/10.1103/PhysRevB.80.045114.
[269] V. V. Laguta, M. Nikl, Electron spin resonance of paramagnetic defects and related charge carrier traps in complex oxide scintillators, Phys. Status Solidi Basic Res. 250 (2013) 254–260. https://doi.org/10.1002/pssb.201200502.
[270] A. Antuzevics, G. Krieke, G. Doke, B. Berzina, The origin of bright cyan persistent luminescence in Ca_2SnO_4: La^{3+}, Materialia. 21 (2022) 101374. https://doi.org/10.1016/j.mtla.2022.101374.
[271] X. Wu, Y. Yang, S. Gai, L. Liu, Z. Zhou, M. Li, Y. Zhong, M. Xia, N. Zhou, Z. Zhou, Enhancing photoluminescence properties of Mn^{4+}-activated $Sr_{4-x}Ba_xAl_{14}O_{25}$ red phosphors for plant cultivation LEDs, J. Am. Ceram. Soc. 102 (2019) 7386–7396.

https://doi.org/10.1111/jace.16633.
[272] M. Sójka, J. Zeler, E. Zych, Effect of Ge:Si ratio and charging energy on carriers trapping in $Y_2(Ge,Si)O_5$: Pr powders observed with thermoluminescence methods, J. Alloys Compd. 858 (2021) 157676. https://doi.org/10.1016/j.jallcom.2020.157676.
[273] T. Lyu, P. Dorenbos, Vacuum-Referred Binding Energies of Bismuth and Lanthanide Levels in $ARE(Si,Ge)O_4$ (A = Li, Na; RE = Y, Lu): Toward Designing Charge-Carrier-Trapping Processes for Energy Storage, Chem. Mater. 32 (2020) 1192–1209. https://doi.org/10.1021/acs.chemmater.9b04341.
[274] Y. Zhang, Y. Liu, L. Yang, S. Hu, Z. Wang, Z. Jing, H. Nian, B. Liu, G. Zhou, S. Wang, Preparation and luminescence properties of thermally stable Mn^{4+} doped spinel red-emitting ceramic phosphors, J. Lumin. 220 (2020) 117016. https://doi.org/10.1016/j.jlumin.2019.117016.
[275] T.-G. Kim, T. Kim, Y.-S. Kim, S.-J. Im, Effect of Alkali-Earth Metal Fluorides on Phase and Luminescence of Magnesium Germanate Phosphors, J. Electrochem. Soc. 157 (2010) J397. https://doi.org/10.1149/1.3482025.
[276] H. Przybylińska, Y. Zhydachevskyy, A. Grochot, A. Wołoś, V. Stasiv, M. Glowacki, A. Kaminska, S. Ubizskii, M. Berkowski, A. Suchocki, Electron Paramagnetic Resonance and Optical Studies of Thermoluminescence Processes in Mn-Doped $YAlO_3$ Single Crystals, J. Phys. Chem. C. 126 (2022) 743–753. https://doi.org/10.1021/acs.jpcc.1c08997.
[277] H. Wu, Q. Zhu, X. Sun, J.-G. Li, Regulating anti-site defects in $MgGa_2O_4$: Mn^{4+} through Mg^{2+}/Ge^{4+} doping to greatly enhance broadband red emission for plant cultivation, J. Mater. Res. Technol. 13 (2021) 1–12. https://doi.org/10.1016/j.jmrt.2021.04.045.
[278] Y. Kitagawa, J. Ueda, S. Tanabe, Blue Persistent Phosphor of $YSiO_2N$: Ce^{3+} Developed by Codoping Sm^{3+} or Tm^{3+} Ions and Thermoluminescence Analysis of Their Trap Distributions, Phys. Status Solidi Appl. Mater. Sci. 219 (2022). https://doi.org/10.1002/pssa.202100670.
[279] A. Dobrowolska, A.J.J. Bos, P. Dorenbos, Electron tunnelling phenomena in YPO_4: Ce, Ln (Ln = Er, Ho, Nd, Dy), J. Phys. D. Appl. Phys. 47 (2014) 335301. https://doi.org/10.1088/0022-3727/47/33/335301.
[280] B. Henderson, J.E. Wertz, Defects in the alkaline earth oxides, Adv. Phys. 17 (1968) 749–855. https://doi.org/10.1080/00018736800101386.